UNIVERSITY OF THE
WITWATERSRAND,
JOHANNESBURG

Expression, purification, structural and functional analysis of *Klebsiella pneumoniae* nicotinate nucleotide adenylyltransferase

by Tasvi Daya

1131535

School of Molecular and Cell Biology

A research report submitted to the Faculty of Science, University of Witwatersrand, Johannesburg, in fulfilment of the requirements of the degree of Masters in Science in the school of Molecular and Cell biology.

Supervisor: Dr Ikechukwu A Achilonu

2020

DECLARATION

I declare that this dissertation is my own, unaided work. It is being submitted for the Degree of Master of Science (MSc) by dissertation at the University of Witwatersrand, Johannesburg. It has not been submitted for any other degree or examination at any other university.

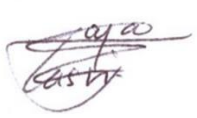

_____

Tasvi Daya

Date: 25/2/2021

ABSTRACT

Ongoing and new nosocomial infections threaten sub-Saharan African regions with their spiking statistics. Almost 50% of patients in health-care settings develop nosocomial infections. *Klebsiella pneumoniae* is a widespread bacterium recognized for conferring bacterial resistance against most current nosocomial antibiotics. These resistance genes can be contracted by other pathogens promoting an outbreak of hospital infections led by superbugs within Africa. This study focuses on a novel expression, purification and structural analysis of *K. pneumoniae* Nicotinate nucleotide adenylyltransferase (*Kp*NNAT), an enzyme responsible for cellular metabolism and redox balance. *Kp*NNAT was over-expressed in a pGEX-4T-1 vector with a Glutathione S-transferase (GST) tag and a hexahistidine tag. The enzyme was successfully purified and cleaved using both Glutathione (GSH)-agarose column and a Nickel immobilised metal affinity column (Ni^{2+}-IMAC) in the presence of thrombin. Expression and purification yielded pure *Kp*NNAT with a wet biomass concentration of 5.5 mg/g of *E. coli* cells. A dual enzyme activity assay consisting of substrates Nicotinate Mononucleotide (NMN) and Adenosine Triphosphate (ATP) in the presence of alcohol dehydrogenase (ADH) proved that the expressed enzyme was active. Structural characterisation of *Kp*NNAT was achieved by assessing the secondary structure through far-UV circular dichroism (CD), the tertiary structure through tryptophan fluorescence, 8-Anilinonaphthalene-1-sulfonic acid (ANS) binding and methylanthraniloyl-ATP (mant-ATP) binding. The secondary structural analysis revealed a predominant α-helical secondary structure of *Kp*NNAT. Tertiary structural analysis indicated the presence of predominantly buried tryptophan residues that are exposed upon the unfolding of *Kp*NNAT. Upon the binding of substrate ATP and product NAD^+ to *Kp*NNAT, displacement of ANS and mant-ATP occurred. These displacement studies further indicated that *Kp*NNAT may experience product inhibition and ligand-induced conformations. Thermodynamic analysis, through isothermal titration calorimetry (ITC), showed that the binding of ATP to *Kp*NNAT is an exothermic, single-site binding event. Data from this study concluded that the *Kp*NNAT active site and structural-water molecules which are present during enzyme catalysation can be exploited for drug design and should be further analysed as a possible target in preventing the spread of ESKAPE pathogen infections within Africa.

DEDICATION

To the people who inspire me the most,

My mom, my dad and my sister,

Everything that I am and everything that I have achieved in life, is because of you.

"I believe in you"

ACKNOWLEDGEMENTS

To my supervisor and mentor, Dr Ikechukwu A Achilonu, thank you for your patience, understanding and support towards my work, ideas and career progression. You continue to inspire me and assist in the expansion of my knowledge and passion for biochemistry. The techniques, experiences and principles I have learnt from you are invaluable. I know that I am a better scientist today because of you. Thank you for allowing me the honour to be your student and always nudging me in the right direction.

To my family and friends, specifically my Mom, Dad, Nikita, Akhil and Rohil, thank you for always listening to my biochemistry dilemmas and supporting me through the tough times. I appreciate your faith and belief in my goals and dreams. Thank you for your continuous love and support. I am grateful for each one of you.

To Prof Y. Sayed, thank you for your advice and suggestions regarding my ITC data and interpretation. I am grateful for your time and guidance throughout my Masters.

To Dr Monare Thulo, "It's okay, it happens", thank you for your assistance and advice in ITC experiments and training on ITC equipment in Protein-Structure Function and Research Unit (PSFRU). I am grateful for all of your guidance and advice.

To Dr Roland Worth, thank you for your insightful thoughts, guidance and support throughout this journey. I will always appreciate your kindness.

To Jessica Olfsen, thank you for always lending your ear to all of the problems I've faced and your never-ending help towards this journey. Your advice and presence will always be appreciated.

To the members and staff of the Protein-Structure Function and Research Unit (PSFRU) at the University of Witwatersrand (WITS), thank you for the guidance, support and amazing memories that I will always cherish.

To the National Research Foundation (NRF) and University of Witwatersrand (WITS), thank you for the financial assistance.

TABLE OF CONTENTS

LIST OF FIGURES

LIST OF TABLES

LIST OF ABBREVIATIONS

A. baumannii	*Acinetobacter baumannii*
ADH	Alcohol Dehydrogenase
Ala	Alanine
AMR	Anti-microbial resistance
ANS	8-Anilinonaphthalene-1-sulfonic acid
Asp	Aspartic acid
ATP	Adenosine triphosphate
Δ*G*°	Change in free energy at standard conditions
Δ*H*°	Change in enthalpy at standard conditions
Δ*S*°	Change in entropy at standard conditions
DNA	Deoxyribonucleic Acid
E. aerogenes	*Enterobacter aerogenes*
E. cloacae	*Enterobacter cloacae*
E. faecium	*Enterococcus faecium*
E.coli	*Escherichia coli*
EC	Enzyme commission number
*Ec*NNAT	*Escherichia coli* Nicotinic acid Mononucleotide Adenylyltransferase
ESBL	Extended spectrum β-lactamase
GSH	Glutathione
GST	Glutathione *S*-transferase
GTP	Guanosine Triphosphate
H. sapien	*Homo sapien*
HAI	Health-care associated infections
HGT	Horizontal gene transfer
His	Histidine
*Hs*NNAT	*Homo sapien* Nicotinic acid Mononucleotide Adenylyltransferase
IMAC	Immobilised Metal Affinity Chromatography
IPTG	Isopropyl β- d-1-thiogalactopyranoside
ITC	Isothermal Titration Calorimetry
kDa	Kilodaltons
*Kp*NNAT	*Klebsiella pneumoniae* mononucleotide adenylyltransferase
LPS	Lipopolysaccharide antigen
Mant	Methylanthraniloyl

MCS	Multiple cloning site
MDR	Multi-drug resistance
MRSA	Methicillin-Resistant *S. aureus*
NaAD	Nicotinic aid Adenine Dinucleotide
NAD	Nicotinamide adenine dinucleotide
NaMN	Nicotinic acid mononucleotide
NNAT	Nicotinic acid mononucleotide adenylyl transferase
NLS	Nuclear localisation sequence
NMN	Nicotinamide Mononucleotide
NNAT	Nicotinamide mononucleotide adenylyltransferase
NRMSD	Normalized Root Mean Square Deviation
OXA	Oxicillases
P. aeruginosa	*Pseudomonas aeruginosa*
PBP	Penicillin-binding protein
PBS	Phosphate Buffer Saline
PDB	Protein Data Bank
pI	Isoelectric point
QS	Quorum-sensing
rpm	revolutions per min
RSB	Reducing Sample Buffer
S. aureus	*Staphylococcus aureus*
SDS-PAGE	Sodium Dodecyl Sulphate Polyacrylamide Gel Electrophoresis
SHV	Sulfhydryl variable enzymes
Ser	Serine
TCEP	Tris (2-carboxyethyl) phosphine
TEMED	N,N,N’,N’-tetramethyethylenediamine
Thr	Threonine
Trp	Tryptophan
TTS	Type III Secretion
Tyr	Tyrosine
UTI	Urinary tract infections
UV CD	Ultraviolet Circular Dichroism
YT	Yeast, Tryptone

All amino acids are labelled in accordance with the IUPAC system

CHAPTER 1:

INTRODUCTION

1.1 Problem statement

Due to their spiking statistics, nosocomial infections have emerged as a leading problem across sub-Saharan African regions. Almost 50% of patients in hospitals or health-care settings develop nosocomial infections (Khan *et al*., 2017). These infections are spread during residency at hospitals or health-care environments and are linked to the duration of the patients' visits (Nair *et al*., 2018). The ESKAPE pathogens (*Enterococcus faecium, Staphylococcus aureus, Klebsiella pneumoniae, Acinetobacter baumannii, Pseudomonas aeruginosa, Enterobacter*) are the main distributors of these infections. These Gram-positive and Gram-negative bacteria can be contracted through direct or indirect contact as well as through airborne transmission (Nair *et al*., 2018). Common infections caused by these pathogens include urinary tract infections (UTI's), surgical site and bloodstream infections, pneumonia and many others (Scherbaum *et al*., 2014). In severe cases, these infections contribute to a physical and financial burden, and may even cause death. There are available treatments for these illnesses such as cephalosporins, fluoroquines, carbapenems and others (Bergogne-Bérézin, 1999). The threat of these pathogens emerged since most of these bacteria have developed multi-drug resistance (MDR) such as vancomycin-resistance *Enterococcus* (VRE) and methicillin-resistant *S. aureus* (MRSA). *K. pneumoniae* is known as a "collector" of these resistance genes through conjugation of plasmids and is currently resistant to most developed antibiotics (Hirsch and Tam, 2010). Considering the above, the contraction of resistance genes from this bacterium to others is a major concern and the continuous development of new antibiotics is required to avoid the current issue surrounding ESKAPE pathogens.

1.2 Rationale

The looming threat of ESKAPE pathogens is associated with its antibiotic resistance to date. These pathogens have developed resistance to current β-lactam therapeutics such as carbapenems, methicillin, vancomycin and others (Obritsch *et al*., 2005). Due to virulence, horizontal gene transfer (HGT), specific efflux systems and drug inactivation, these pathogens are not fully susceptible to antibiotics (Santajit and Indrawattana *et al*., 2016). The rising pathogenicity of the ESKAPE pathogens in Africa is of high concern and new approaches to drug therapies should be explored (Ramsamy *et al*., 2018). Currently, β-lactam antibiotics pose as first-line treatments in ESKAPE infections. The mechanism of action prevents peptidoglycan synthesis in bacteria, an essential step in bacterial cell wall synthesis and cell viability (Bush and Bradford, 2016). Due to the eminent issue of resistance surrounding these antibiotics, the World Health Organisation (WHO) has listed ESKAPE pathogens as that which requires urgent new antibiotics (Tacconelli *et al*., 2018). Potential alternative therapies include silver nanoparticles, antimicrobial peptides (AMPs), bacteriophage therapy and combinational drug therapy (Mulani *et al*., 2019). However, associated research shows several limitations to these techniques and contrasting data during *in vivo* and *in vitro* trials (Mulani *et al*., 2019). Furthermore, several reviews focus on the addition or utilisation of various agents such as bacteriophages or nanoparticles against MDR bacteria, instead of specifically targeting ESKAPE pathogens (Mulani *et al*., 2019). Hence, new approaches targeting the ESKAPE pathogens need to be ventured for rational drug design.

Enzymes are considered potential targets for drug therapy due to the cascade of reactions that they catalyse (Magni *et al*., 2009). They are responsible for the formation of various products/by-products that are essential for survival. The essential enzyme, nicotinic acid/nicotinamide mononucleotide adenylyltransferase, also referred to as nicotinate nucleotide adenylyltransferase (NNAT) is responsible for the production of nicotinamide adenine dinucleotide (NAD^+) (Magni *et al*., 2009). This co-factor is vital in redox reactions, DNA repair and metabolic states of the cell (Jayaram *et al*., 2011). Depletion or insufficiency of NAD^+ may result in organismal death or weakened immune systems (Jayaram *et al*., 2011). NNAT is a promising drug target since it is essential in bacterial cell survival and differs catalytically and structurally from the human NNAT (Franchetti *et al*., 2003). The sequence similarity between bacterial and human NNAT is ~20% (Magni *et al*., 2009). Thus, bacterial NNATs poses as a possible target for drug therapy.

Analysis of bacterial NNAT must be performed to evaluate the enzyme as a drug target. This can be done using biochemical and biophysical processes to gain insight into the functionality and structure of NNAT. Through functionality associated studies, the binding events or mechanisms can provide insight to ligand binding and the polarity of binding pockets which can be manipulated in drug design (Amaro, 2017). The investigation into enzyme structure can be performed and further applied to crystallography (Maveyraud and Mourey, 2020). NNAT plays a crucial role in regulating cellular metabolism and redox reactions which are essential for cell survival (Magni *et al*., 2009). Thus, further analysis into enzyme structure and function is obligatory to understand the underlying mechanism of action and/or structural relevance to its function. These structural and functional concepts provide a platform to exploiting NNAT as a probable drug target for nosocomial infections. Hence, in this study, analysis of *Kp*NNAT, will be performed for the first time to investigate the structure and functionality of this enzyme.

1.3 Aims and objectives:

This study aimed to conduct novel expression, purification, structural characterisation and functional analysis of recombinant *Kp*NNAT.

In order to achieve the aim, the following objectives were carried out:

- Recombinant overexpression of GST-tagged hexahistidine *Kp*NNAT using a pGEX-4T-1 vector.
- Purification and cleavage of tagged *Kp*NNAT using double affinity chromatography and thrombin.
- Quantification of purified *Kp*NNAT using spectrophotometry.
- Analysis of *Kp*NNAT activity using a dual enzyme assay.
- Determination of *Kp*NNAT secondary structural analysis (Far-UV CD) in the native and denatured states.
- Determination of *Kp*NNAT tertiary structure using intrinsic and extrinsic fluorescence in the absence and presence of ligands.
- Analysis of *Kp*NNAT binding events using mant-ATP fluorescence in the absence and presence of ligands.
- Derivation and analysis of thermodynamic parameters associated with the interaction between *Kp*NNAT and substrate ATP using isothermal titration calorimetry (ITC).

1.4 Novelty

K. pneumoniae, member of the ESKAPE pathogen group, is infamous for causing nosocomial infections in Africa. These infections are widespread in health-care facilities and heavily impact patients and health workers. The steady increase in nosocomial infection rates in Africa is an undeniable threat. Due to the antibiotic resistance conferred by *K. pneumoniae*, the need for new alternative drug therapies is imperative. This study focuses on novel research surrounding *Kp*NNAT structure, function and ligandin properties. Targeting this enzyme results in metabolic deficits in bacterial cells which may ultimately lead to cell death. Its high conservation between bacterial species makes this enzyme a suitable target for drug therapy. Insights into *Kp*NNAT structure and function are explored in this study for the first time using a combination of biophysical strategies to produce high yields of purified, active protein for analysis.

1.5 Outline of this dissertation

This dissertation commences from Chapter 2 (Literature review), which entails information regarding ESKAPE pathogens, specifically *Kp*NNAT. Chapter 3 (Materials and methods) discusses the relevant processes performed during the experimental procedures. In Chapter 4 (Results), the outcomes of the corresponding experiments are shown and described. Lastly, Chapter 5 (Discussion) explains the results shown in Chapter 4 and mentions limitations and future work for this study.

CHAPTER 2:
LITERATURE REVIEW

2.1 ESKAPE: Emerging pathogens of concern

Health-care associated infections (HAI), or nosocomial infections are a global concern across all health-care sectors. These infections are contracted during the process of patients being hospitalised for several days or being present in any health-care setting. The burden of these infections is substantial on patients, usually causing further discomfort and may result in death in severe cases (Pearse, 1997). Sub-Saharan African regions are prone to these type of infections as developing countries experience up to 50% nosocomial infections in health-care settings such as intensive units (Elizabeth *et al*., 2016). The severity of nosocomial infections in Africa is shown in Figure 2.1 which demonstrates the expected mortality rate due to bacterial resistance in nosocomial infections. The main agents leading to these infections are the ESKAPE pathogens (Elizabeth *et al*., 2016). This group of pathogens are present on the WHO global priority pathogen list (Ramsamy *et al*., 2018).

Unlike most developed countries, data surrounding ESKAPE pathogen infections and analysis have not been prominent in African countries (Ramsamy *et al*., 2018). Analysis and surveillance associated with ESKAPE pathogens are vital to gain insight into drug therapy at a local or national level and serves as a powerful strategy in disease/infection management across Africa (Ismail *et al*., 2019). However, there are a few studies that analyse the growth of infections due to ESKAPE pathogens in Africa. In particular, studies conducted in South Africa exposes the worrisome growth of ESKAPE infections and antibiotic resistance across the country (Ismail *et al*., 2019) (Ramsamy *et al*., 2018). Data from these studies suggest the growing rate of ESKAPE infections over the years which indicate that more than 50% of *K. pneumoniae* blood cultures (isolates) are non-susceptible to several commonly used antibiotics such as cephalosporins and carbapenems (Perovic *et al*., 2018). Although all ESKAPE pathogens demonstrate antibiotic resistance, *K. pneumoniae* exhibits a high percentage of MDR and accounts for almost one-third of ESKAPE organisms in blood cultures in South Africa (Ramsamy *et al*., 2018). Additionally, more than 90% of patients acquired multi-resistant (carbapenem-resistant) Enterobacteria species (*Klebsiella* species, *Enterobacter* species and other bacterial species) in hospitals across South Africa (Perovic *et al*., 2020). To date, more than 75% of carbapenem-resistant bacteria were *K. pneumoniae* which emphasises

the detrimental role *K. pneumoniae* is playing in South Africa, among the rest of the ESKAPE pathogens (Perovic *et al*., 2020). To further expose the threat of ESKAPE pathogens, a recent outbreak of *K. pneumoniae* in a neonatal unit at a regional hospital in South Africa was investigated (Essel *et al*., 2020). The study expresses the urgency of the matter surrounding ESKAPE pathogens and the desperate need for safe and hygienic practices in health-care settings, in addition to the requirement of new drug therapies against this group of bacteria in South Africa.

The group of bacteria characterised as ESKAPE consists of both Gram-negative and Gram-positive bacteria (Santajit and Indrawattana, 2016). A variety of infections caused by these pathogens include UTI's, nosocomial respiratory tract infections, meningitis, surgical site and bloodstream infections, gastroenteritis and many other infections due to low immune responses (Elizabeth *et al*., 2016). The transmission of ESKAPE pathogens may occur through compromised skin and mucosal surfaces and can be transmitted through direct and indirect contact or is transmitted by being airborne (Elizabeth *et al*., 2016). These pathogens are also susceptible to HGT whereby they can acquire resistance genes to antibiotics, resulting in MDR bacteria or "superbugs". HGT is described as a process involving the movement of genetic information between organisms (usually of different species) (Burmeister, 2015). The mechanisms of HGT include conjugation, transformation and transduction of which conjugation is usually responsible for anti-microbial resistance (AMR) gene transferal in bacteria (Wintersdorff *et al*., 2016). Figure 2.2 illustrates the various mechanisms of HGT. Conjugation involves the transfer of genes through physical contact, transduction involves the transfer of DNA through bacteriophages from one bacterium to another and transformation involves the transfer of free DNA from the environment (Pang *et al*., 2018).

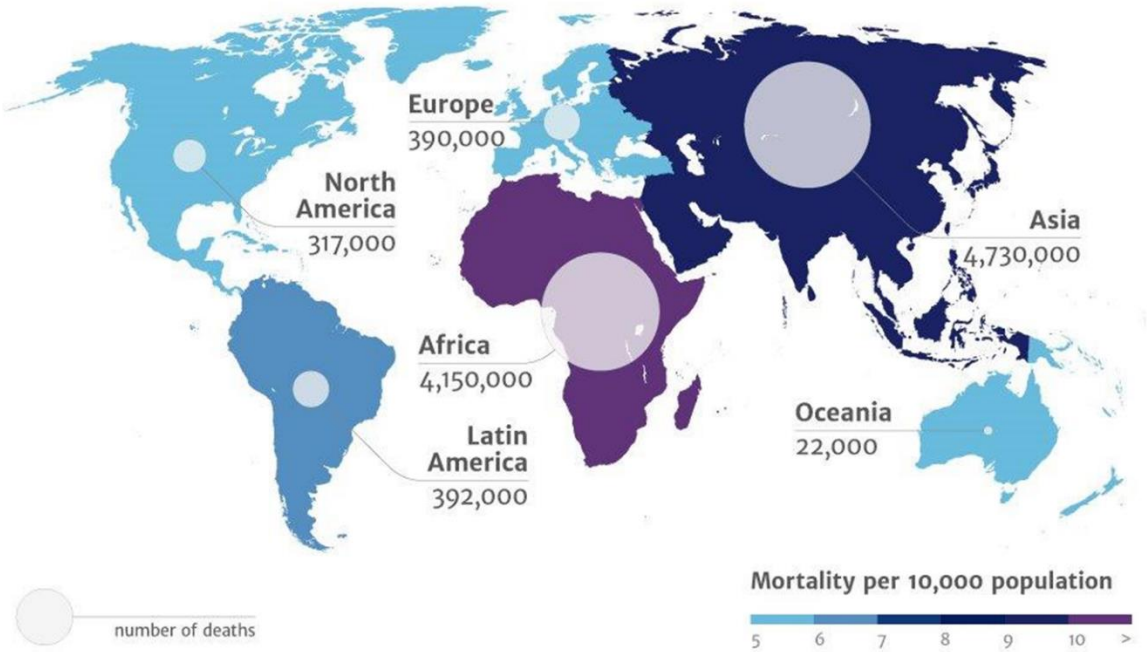

Figure 2.1: Map illustrating the distribution of nosocomial infections on a global scale.
Each area is encoded by a colour representing varied mortality per 10000 population of nosocomial infections. The African region depicts the highest mortality rate (purple colour) and second highest mortalities due to antibiotic-resistant bacteria by the year 2050. The urgency of nosocomial infections is highlighted by this figure (Crew, 2014).

A

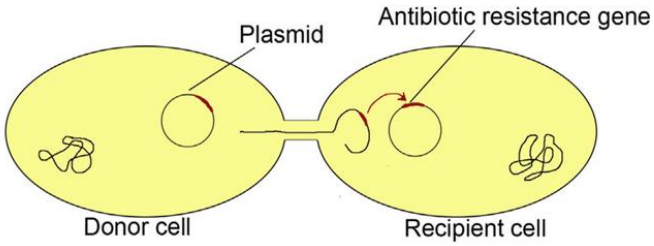

B

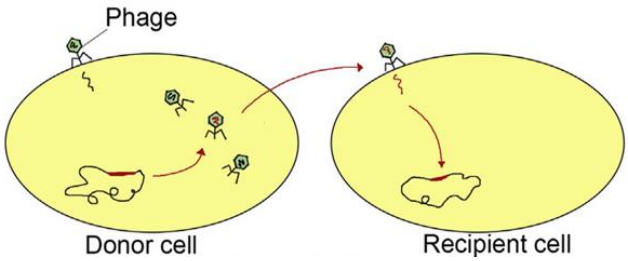

C

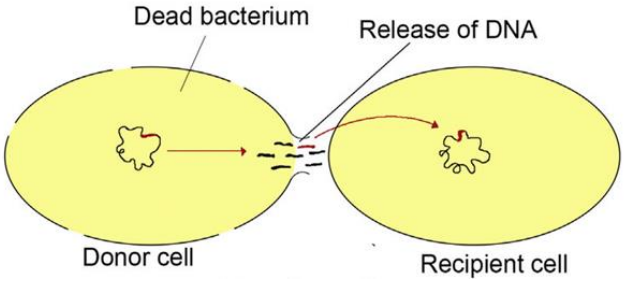

Figure 2.2: Mechanisms of horizontal gene transfer in bacteria

Process A represents conjugation of DNA in bacteria through physical contact. Process B represents the transduction of DNA via bacteriophages and process C represents the transformation principle of DNA uptake in bacteria. These are the various mechanisms that allow for bacterial gene transfer (Pang *et al*., 2018).

Despite efforts made by the WHO, ESKAPE pathogens are rapidly dominating HAI due to issues pertaining to unsanitary health-care settings/machinery and MDR bacteria. Mechanisms of drug resistance include drug inactivation or alteration, biofilm formation, changes in cell permeability resulting in reduced drug absorption and drug site modification (Santajit and Indrawattana, 2016).

2.2 Nosocomial infections: Antibiotics

ESKAPE pathogens are associated with multi-resistance to various β-lactam antibiotics (Obritsch *et al*., 2005). This β-lactam class of antibiotics includes penicillin, cephalosporins, carbapenems, β-lactamase inhibitors and monobactams (Pandey and Cascella, 2020). A common feature of these drugs is the β-lactam ring which is highly reactive and is shown in Figure 2.3A (Pandey and Cascella, 2020). β-lactam drugs are strongly associated as a bactericidal agents due to their ability to disrupt the process of peptidoglycan synthesis in bacteria (Bush and Bradford, 2016). During bacterial cell wall synthesis, peptidoglycan is essential for cell stability and structure (Pandey and Cascella, 2020). During the last step of peptidoglycan synthesis, β-lactams covalently bind to essential penicillin-binding proteins (PBP), preventing peptidoglycan cross-linking in both Gram-negative and Gram-positive bacteria (Bush and Bradford, 2016). The binding of β-lactams to the PBP's results in loss of bacterial cell viability (Pandey and Cascella, 2020). Although β-lactam drugs deem successful mechanisms of action, the resistance to these drugs in bacterial cells is a growing concern. Resistance may be conferred through β-lactamases (inactivates β-lactam rings)(Figure 2.3B), PBP mutations, increased efflux of β-lactams and horizontal gene transfer of resistance genes (Bush and Bradford, 2020).

A

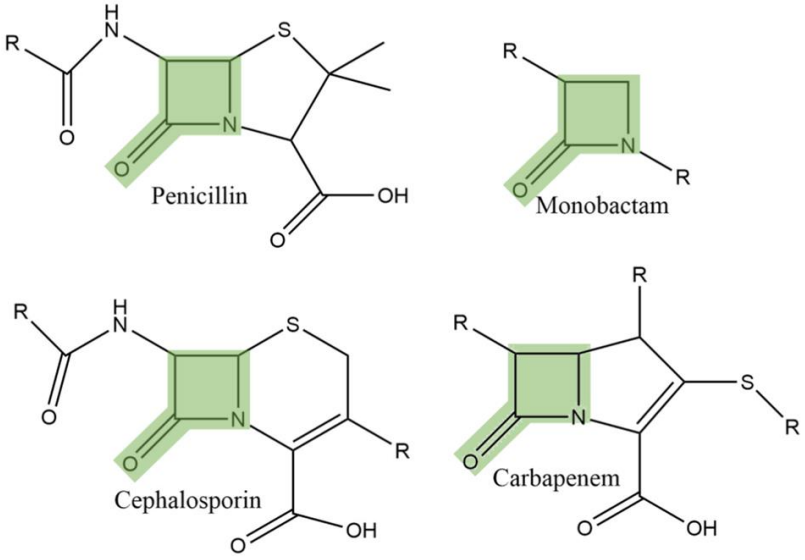

B

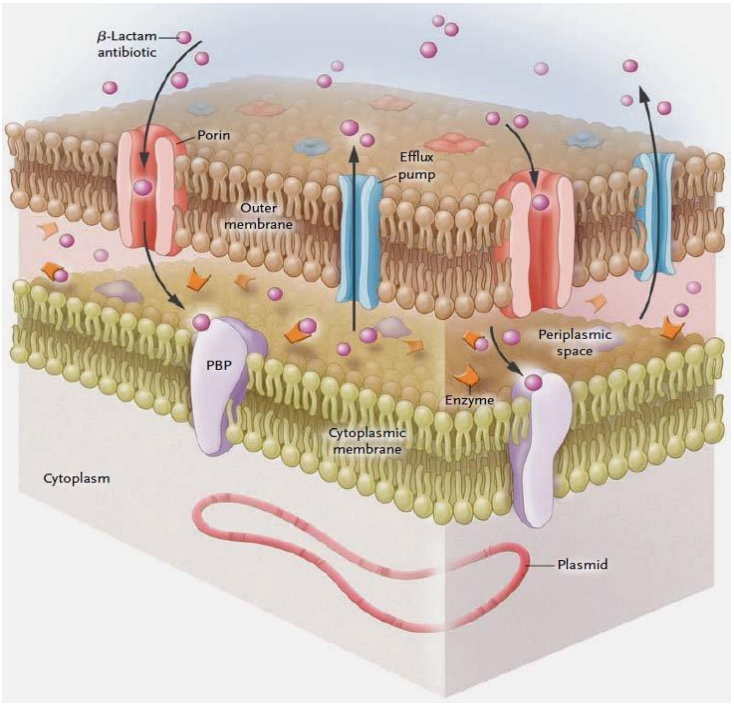

Figure 2.3: Nosocomial antibiotics against ESKAPE pathogens

Figure A demonstrates the common β-lactam drugs (penicillin, monobactam, cephalosporin and carbapenem) with their respective β-lactam rings (shaded in green). The β-lactam ring consists of three carbons and one nitrogen and is consistent throughout the β-lactam antibiotics. The chemistry of these drugs differs within their side chains. Figure B provides the mechanism of action of a β-lactam drug. The entry of penicillin prevents the synthesis of peptidoglycan in bacterial cells. The diagram also depicts a mechanism of drug resistance induced by β-lactamase (orange enzyme) which inactivates β-lactam drugs. This prevents the attachment of β-lactam drugs to the penicillin-binding protein (DiLallo, 2018) (Karah, 2011).

2.2.1 Overview of the molecular mechanisms of antibiotic resistance

Bacterial drug resistance can be intrinsic or acquired via HGT. The overall mechanisms of drug resistance can be categorised broadly as alteration of drug binding sites, drug inactivation, the formation of biofilms and changes in intracellular drug concentrations (Santajit and Indrawattana, 2016). These mechanisms aid in conferring resistance to most current β-lactam antibiotics which is illustrated in Figure 2.4.

2.2.1.1. Alteration of drug binding site/s

Several bacteria possess the ability to modify their target sites to prevent drug binding. A common example is the mutated PBP (essential for bacterial cell wall synthesis) such as PBP2a, a unique mutation of PBP which experiences low affinity for β-lactam drugs such as vancomycin (Santajit and Indrawattana, 2016). Thus, the presence of high amounts of β-lactam antibiotics has a reduced or no effect on bacteria that possess a mutated PBP (Santajit and Indrawattana, 2016).

2.2.1.2. Drug inactivation

One of the most common bacterial mechanisms that lead to drug resistance is the modification or inactivation of antibiotics. The production of enzymes such as β-lactamases, chloramphenicol, acetyltransferases and aminoglycoside-modifying enzymes and others, often lead to resistance of the respective antibiotics (Santajit and Indrawattana, 2016). The popular enzymes responsible for many resistance cases are the β-lactamases which hydrolyse the β-lactam ring in all β-lactam antibiotics (Santajit and Indrawattana, 2016). There is great diversity in β-lactamases and their activity is varied in different bacterial cells. This broad enzyme class includes penicillinases, extended spectrum β-lactamases (ESBL), carbapenemases, sulfhydryl variable enzymes (SHV), oxacillin hydrolysing enzymes (OXA) and several others. The most clinically important β-lactam enzymes are produced by Gram-negative bacteria (Giedraitienė *et al*., 2011). ESBLs such as SHV experience high mutation rates and thus increases the enzyme diversity and resistance against antibiotics (Santajit and Indrawattana, 2016). In addition to β-lactamases, drug inactivation also occurs via group transfer. Enzymes that modify aminoglycosides and chloramphenicol have the ability to bind adenylyl, phosphoryl or acetyl groups to the periphery of the antibiotics. Such enzymes are able to reduce the affinity of those modified molecules and further provides extended spectrum resistance to other antibiotics (Maurice *et al*., 2008).

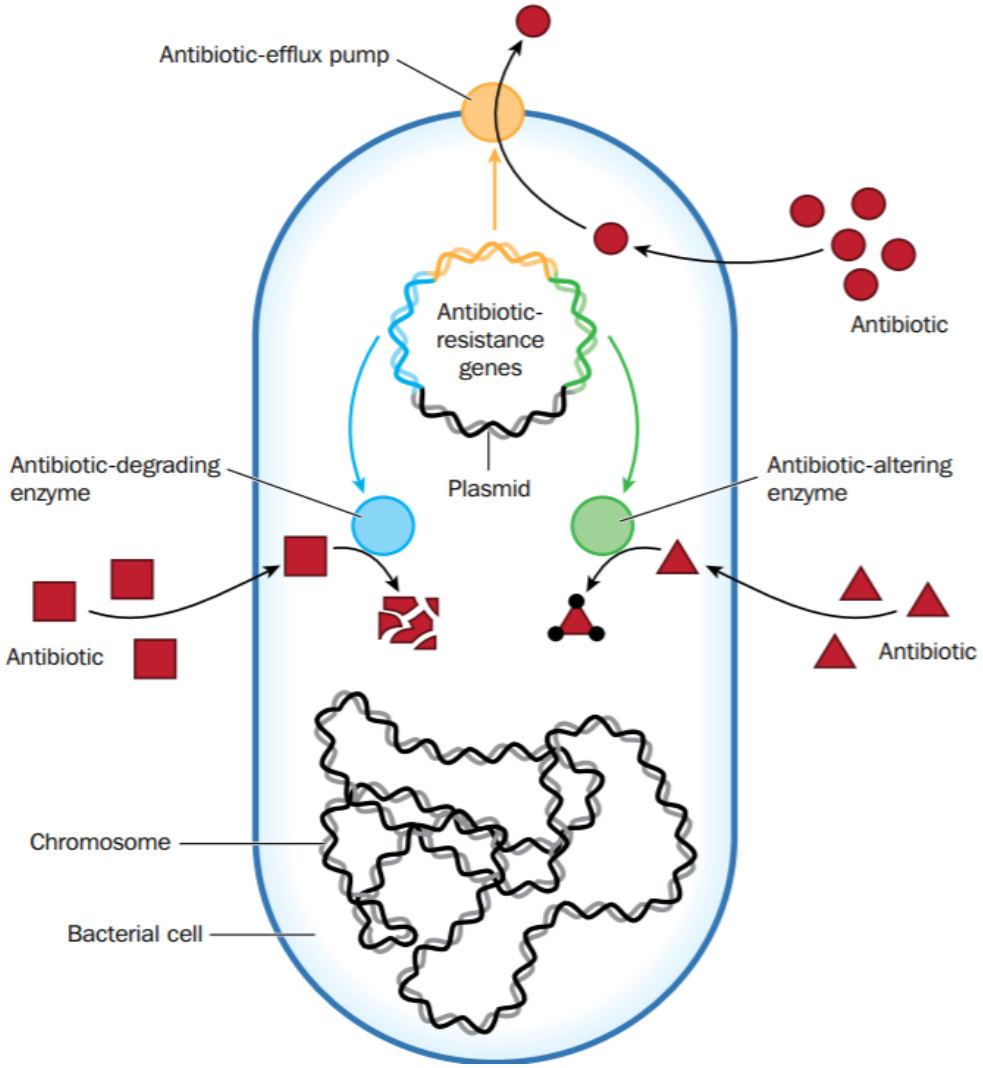

Figure 2.4: Mechanisms of bacterial antibiotic resistance

The diagram illustrates the various mechanisms of antibiotic resistance in bacterial cells. Such mechanisms include efflux pumps, target modification, degradation of antibiotics, modification of antibiotics and the uptake of resistance genes via horizontal gene transfer as indicated by the antibiotic resistance gene plasmid. These mechanisms aid in bacterial survival against current therapeutics (Cope and Cope, 2013).

2.2.1.3. Formation of biofilms

Biofilm formation can be described as a process in which microorganisms attach to and grow on biotic and abiotic surfaces while producing extracellular polymers that aid in biofilm attachment and survival (Donlan, 2001). The significance of biofilms on public health is vital since biofilms may exhibit decreased susceptibility to antimicrobial drugs (Donlan, 2001). In addition, the resistance conferred by biofilms could be intrinsic or acquired through other organisms in the biofilm (Donlan, 2001). The matrix of these biofilms produces a favourable environment for the microbes by providing conditions such as low oxygen levels, low pH levels, high carbon dioxide levels and decreased water availability (Santajit and Indrawattana, 2016). Thus, the antibiotic effects are reduced due to these unconventional conditions produced by biofilms since most of the antibiotics cannot be fully functional in these conditions.

2.2.1.4. Intracellular drug concentrations

A major contributing factor towards antibiotic susceptibility is the balance between antibiotic uptake and antibiotic elimination in bacteria. Due to the decreased bacterial cell permeability and the presence of specific efflux pumps, bacterial mechanisms as such, are used as strategies for antibiotic resistance (Santajit and Indrawattana, 2016). The outer membranes of Gram-negative bacteria possess porins that allow many substances, including antibiotics, inside the cells. Thus, reduction in porin proteins such as OprD decreases the influx of antibiotics, thus contributing to resistance (Fukuoka *et al*., 1993). The complete loss of other outer membrane proteins (OMP) results in complete resistance against various antibiotics (Fukuoka *et al*., 1993). Gram-negative bacteria such a *K. pneumoniae* and *A. baumannii* exhibit OMP reduction or loss and this aids in their antibiotic resistance to therapeutics such as carbapenems and cephalosporins (Santajit and Indrawattana, 2016). In addition to OMPs, another bacterial strategy used to combat antibiotics are efflux pumps. Efflux pumps are membrane proteins used to transport substances across the cytoplasmic membrane and cell envelope (Giedraitienė *et al*., 2011). These pumps are found in many bacteria and expel antibiotics from the cell at a high rate, thus contributing to drug insufficiency inside the cell. Most pumps are multi-drug transporters which greatly produces MDR across these bacterial organisms (Džidić *et al*., 2008). The most common efflux pumps form part of the resistance-nodulation division (RND) family in Gram-negative bacteria (Sun *et al*., 2014). Particularly, the AcrAB-TolC and MexAB-OprM pumps are chromosomally encoded and essential for bacterial survival (Santajit and Indrawattana, 2016). These pumps frequently expel a variety of antibiotics and biocides

that are used in healthcare settings, which greatly contributes to the antibiotic resistance across bacterial organisms (Nikaido and Pagès, 2012).

2.3 Overview of ESKAPE pathogens

2.3.1 Enterococcus faecium

E. faecium is a facultative anaerobic, Gram-positive bacterium located in the intestinal tracts of humans and animals (Markwart *et al*., 2019). Although this bacterium participates in commensal roles, it is regarded as an emerging pathogen responsible for nosocomial infections (Markwart *et al*., 2019). Symptoms of these infections include UTI's, bloodstream infections, dermal and endocardium infections (Markwart *et al*., 2019). The features or abilities of this bacterium such as HGT, virulence traits and the possession of biofilm, influence the bacterium's susceptibility to various lines of treatment (Iweriebor *et al*., 2015). To date, *E. faecium* exhibits resistance to vancomycin, a treatment that had once been successful against *E. faecium* infections (Iweriebor *et al*., 2015). VRE are responsible for almost 75% of deaths associated with *E. faecium* infections which heightens the urgency of therapeutic success against this bacterial pathogen (Iweriebor *et al*., 2015).

2.3.2 Staphylococcus aureus

S. aureus is a non-motile, non-spore forming, facultative anaerobic and Gram-positive bacterium located on/in the skin and mucous membranes of humans and animals (Taylor and Unakal, 2020). Once this bacterium enters the bloodstream or internal organs of the body, severe infections arise as a result. These infections include meningitis, scalded skin syndrome (blisters/peeling), wound infections, endocarditis and many more (Bien *et al*., 2011). Africa, among other continents, has displayed a rise in *S. aureus* cases in recent years due to the resistance that the bacterium confers (Schaumburg *et al*., 2014). Due to their features such as biofilm formation, genetic elements (virulence factors) such as SpA (structural element anchored to the bacterial cell wall) and transferal of chromosomal material, *S. aureus* has high survival rates against antibiotics (Bien *et al*., 2011). The focal issue regarding *S. aureus* infections is due to the resistance against methicillin, the first-line of treatment against these infections (Taylor and Unakal, 2020). The prominent use of antibiotics within health-care settings have facilitated the spread of resistance genes through bacteria, which have led to the rise of antibiotic-resistant species such as MRSA (Gheorghe *et al*., 2018). The ability of these bacteria to transfer plasmids and transposons play a crucial role in resistance conferred to β-lactam antibiotics (Gheorghe *et al*., 2018). A chromosomally localised gene, *mEcA*, confers

resistance and is only upregulated upon the exposure to β-lactam antibiotics (penicillin and derivatives of penicillin) (Gheorghe *et al*., 2018). Thus, HGT of material from one bacterium to another poses a threat against therapeutic development.

2.3.3 Acinetobacter baumannii

A. baumannii is an aerobic, non-motile and Gram-negative bacterium predominantly located in soil and surface water (Howard *et al*., 2012). This bacterium targets moist surfaces such as mucous membranes of humans through wounds or injuries. Untreated *A. baumannii* infections result in septicaemia (bloodstream infections due to bacterial toxins) and organ failure (Howard *et al*., 2012). As a result of the high prevalence of *A. baumannii* infections globally, WHO has declared *A. baumannii* as an emerging pathogen of concern (Harding *et al*., 2018). Increased resilience of *A. baumannii* is achieved through their virulence factors, HGT, the formation of biofilms and structural features. An important factor, the *OmpA* gene is predominantly responsible for the bacterial pathogenicity by inducing host cell apoptosis (Howard *et al*., 2012). In addition to its pathogenicity, the *OmpA* gene, *AmpC* gene and OXA-51-like enzymes also aid in bacterial resistance. These enzymes have the ability, although weak, to hydrolyse penicillin and carbapenems, while the overexpression of the *AmpC* gene is linked to cephalosporin resistance (Howard *et al*., 2012). Thus, *A. baumannii* exhibits MDR to many first-line treatments.

2.3.4 Pseudomonas aeruginosa

Infections due to *P. aeruginosa* threatens immunocompromised individuals within health-care settings. This Gram-negative, rod-shaped bacterium is commonly found within the environment (soil and water) and can be spread to humans or animals through contaminated soil or water (Bassetti *et al*., 2018). Serious infections such as pneumonia, endocarditis, malignant external otitis and meningitis can be due to *P. aeruginosa* contamination (Bodey *et al*., 1983). The virulence and pathogenicity of this bacterium enable its survival and resistance to many current therapeutics. The presence of various virulence factors such as quorum-sensing (QS), type III secretion (TTS) and lipopolysaccharide antigen (LPS) enhance the pathogenicity of *P. aeruginosa* (Hauser, 2011). These factors are responsible for cell density signalling, injection of bacterial toxins and protection against complement-mediated lysis respectively (Hauser, 2011). In addition to its virulence factors, *P. aeruginosa* exhibits resistance to multiple drugs such as β-lactam antibiotics, aminoglycosides and quinolones (Bassetti *et al*., 2018). *P. aeruginosa* possesses genes like oxicillases (*OXA*) and *AmpC* which

are responsible for conferring resistance to carboxypenicillins and cephalosporins (Bassetti *et al*., 2018). In addition, its structural advantages, such as low membrane permeability and active efflux pumps aid in its resistance features. Efflux systems such as *MexXY-OprM* are natural resistance systems which are triggered by the exposure of a single antibiotic. Some antibiotics, such as quinolones, act as substrates for these efflux systems, thus generating cross-resistance towards many other antibiotics (β-lactams and aminoglycosides (Bassetti *et al*., 2018). Due to these natural and imported (from other bacteria) resistance genes, systems or mechanisms, *P. aeruginosa* infections contribute to the urgency of MDR "superbugs".

2.3.5 Enterobacter

Enterobacter species are Gram-negative, facultative anaerobic and motile bacteria which thrive in the intestines of animals (Davin-Regli and Pagès, 2015). *E. aerogenes* and *E. cloacae* are well-known species of the *Enterobacter* family that are involved in the spread of nosocomial infections within health-care settings (Davin-Regli and Pagès, 2015). *Enterobacter* infections lead to lower respiratory problems, skin infections, endocarditis, UTI's, septic arthritis and much more (Davin-Regli and Pagès, 2015). Apart from its virulent strategies of biofilm formation and toxin secretion (enterotoxins, pore-forming toxins and haemolysins), the *Enterobacter* species exhibits antibiotic-resistance to multiple therapeutics (Davin-Regli and Pagès, 2015). The species displays resistance against ampicillin and cephalosporins due to the possession of the *AmpC* β-lactamases which hydrolyse β-lactam antibiotics (Azevedo *et al*., 2018). In addition to this, the *Enterobacter* species also possesses aminoglycoside-modifying enzymes namely acetyltransferases, phosphotransferases and adenylyltransferases, thus conferring resistance to antibiotics such as aminoglycosides (Davin-Regli and Pagès, 2015). Almost 40% of MDR *Enterobacter* strains possess active efflux systems (Davin-Regli and Pagès, 2015). The presence of these pumps such as the *AcrAB–TolC* pump, is efficient in expelling antibiotics such as tetracycline, fluoroquines and chloramphenicol which aid in the species' resistant nature (Davin-Regli and Pagès, 2015). Thus, the prevailing resistance and virulent factors of the *Enterobacter* species diminishes the chances of viable therapeutics.

2.3.6 K. pneumoniae: A leading cause of nosocomial infections

K. pneumoniae, which is part of the Enterobacteriaceae family, can be characterised as a non-motile, Gram-negative, rod-shaped bacterium that resides in both mammals (mucosal surfaces) and within the surrounding environment (surface water, plants, sewage and soil) (Podschun and Ullman, 1998). As a member of the ESKAPE pathogens, *K. pneumoniae* is one

of the leading causes of nosocomial infections in humans. Naturally, it occurs as a saprophyte (dead organic matter as a food source) within the gastrointestinal tract mucous membranes where it does not cause any illness (Podschun and Ullman, 1998). However, once the bacterium enters the respiratory tract or bloodstream, many infections arise as a result and can be attributed to unsanitary environments within health-care settings such as inadequate sanitation within bathrooms and unsanitary machines such as catheters (Tzouvelekis *et al*., 2012). Common infections caused by *K. pneumoniae* include liver abscess, pneumonia, meningitis, UTI's and wound infections (Kang *et al*., 2004). The challenge surrounding antibiotics against *K. pneumoniae* contribute greatly to the rapid increase in nosocomial infections within sub-Saharan African regions.

There are several bacterial factors which can be attributed to the pathogenicity of *K. pneumoniae* in addition to its ability to acquire various resistance genes. These include structural features such as capsules, fimbriae, lipopolysaccharide layer and adhesins. Capsules surrounding *K. pneumoniae* aid in its survival against host immune responses by protecting the bacterium from host phagocytosis and bactericidal serum factors (Podschun and Ullman, 1998). In addition, different capsular strains expressing different antigens display varying levels of virulence which is attributed to the mannose content within the capsule. Capsular types which contain repetitive sequences of mannose-α-2, 3-mannose, l-rhamnose-α-2 or 3-l-rhamnose are recognised by macrophages and undergo lectinophagocytosis, based on the recognition of surface lectins and carbohydrates (Podschun and Ullman, 1998). Thus, endocytosis (ingestion) of *K. pneumoniae* containing these repeats will occur. However, capsular types that do not contain these sequences are shielded from lectinophagocytosis and are associated with high virulence (Podschun and Ullman, 1998).

Unlike most bacteria, *K. pneumoniae* confers resistance to penicillin due to an *SHV-1* penicillinase in their chromosomes (Wyres and Holt, 2018). High susceptibility to chromosomal mutations results in resistance to other available antibiotics such as colistin or carbapenems designated to *K. pneumoniae* infections (Doorduijn *et al*., 2016). In addition to these mutations, additional acquisition of anti-microbial resistance (AMR) genes through HGT occurs.

Elements such as plasmids and transposons are usually associated with AMR gene transferal through conjugation due to the protection it offers from surroundings and increased efficiencies

when entering a host cell (Norman *et al*., 2009). HGT and AMR genes localised in *K. pneumoniae* is not a recent discovery. Previous studies indicate the acquisition of ESBL, plasmid-mediated enzymes which hydrolyse cephalosporins that are used for enterobacterial treatment (Gupta *et al*., 2003). In addition, other resistance genes against other antibiotics such as chloramphenicol, aminoglycosides, tetracycline and sulphonamides are carried on these plasmids (Gupta *et al*., 2003). Broad-spectrum cephalosporins show low success rates in bloodstream infections and are not recommended for ESBL-producing pathogens. Possible treatments include β-lactamase inhibitors such as tazobactam, clavulanic acid and carbapenems as a last resort treatment for MDR *K. pneumoniae* infections (Gupta *et al*., 2003).

Carbapenems such as meropenem and imipenem are currently the most effective drugs against *K. pneumoniae* infections and multi-resistant strains such as ESBL-producing pathogens. However, certain bacteria contain plasmids that encode for bla_{IMP-1} and bla_{KPC-1} as well as other genes that produce imipenemases and carbapenemases respectively due to HGT (Low *et al*., 2017). These plasmids are transferable and many strains of *K. pneumoniae* exist with several resistance genes to date. Carbapenemases hydrolyse the β-lactam rings of the compounds therefore preventing their absorption and inactivating β-lactams via zinc ions. This results in a decreased outer membrane permeability which enhances its virulence to most antibiotics (Papp-Wallace *et al*., 2011). The MDR feature of *K. pneumoniae* threatens global health since this bacterium contains transferable plasmids and continues to acquire new resistance genes over time. Thus, new approaches for ESKAPE pathogens treatment should be explored to combat resistance acquisition.

Most antibiotics do not exhibit high success rates in serious *K. pneumoniae* infections (Hirsch and Tam, 2010). Thus, novel developments are required in this spectrum of multi-resistant pathogens. Current developments include improved β-lactamase inhibitors such as NXL104 which have been shown to restore β-lactam activity by binding and inactivating β-lactamases in several *K. pneumoniae* pathogens producing carbapenemases (Hirsch and Tam, 2010). Other options include combinational therapy of carbapenems and fluoroquines. Apart from the temporary mitigation of bacterial resistance by antibiotics, other opportunities may reside in targeting specific proteins, enzymes or metabolic products in *K. pneumoniae*.

2.4 Bacterial metabolism of NAD^+

The coenzyme, NAD^+ is essential in maintaining the survival of eukaryotes, bacteria and archaea (Xiao *et al*., 2018). This coenzyme can be reduced to NADH via dehydrogenases, to participate in cellular energy metabolism, or it may be reduced to NADP via kinases to participate in the biosynthesis of fatty acids, nucleic acids and the maintenance of redox activity (Xiao *et al*., 2018). The synthesis efficiency of NADH/NADP is limited by the generation of NAD^+ and thus emphasises the importance of this nucleotide. An imbalance of these redox couples may lead to severe illnesses or death of an organism.

The generation of NADP/NADPH is imperative for reactive oxygen species (ROS) and antioxidant networks for organismal defence due to the need for electron transferal in various reactions (Xiao *et al*., 2018). Thus, it is crucial that the metabolism of NAD^+ occurs optimally. NAD^+ production occurs via two main pathways: i) *De novo* pathway and ii) salvage pathway. The *de novo* pathway produces NAD^+ from quinolinic acid which can be generated from either L-aspartate or L-tryptophan in bacteria (Spaans *et al*., 2015). The salvage pathway is associated with the generation of NAD^+ from degradation products which consist of pyrimidine rings, usually nicotinic acid. Figure 2.5 illustrates the pathways leading to the generation of NAD^+.

2.5 Targeting NAD^+ metabolism in *K. pneumoniae*

Generating NAD^+ through both the *de novo* and salvage pathway yields high amounts of these coenzymes. Several enzymes are r equired to converge products from both pathways and convert them into NAD^+. A key enzyme common in both *de novo* and salvage pathways required for conversion of products into NAD^+, is NNAT (Lin *et al*., 2010). The reactions catalysed by this enzyme is shown in Figure 2.5. Since this enzyme is crucial for NAD^+ generation, it acts as a possible target for pathogens such as *K. pneumoniae*. NAD^+ is essential for bacterial survival, thus, reducing the concentrations of this enzyme in the cell may lead to bacterial death or weakened antioxidant systems thus increasing bacterial susceptibility to drug therapy. This may be achieved by targeting NNAT.

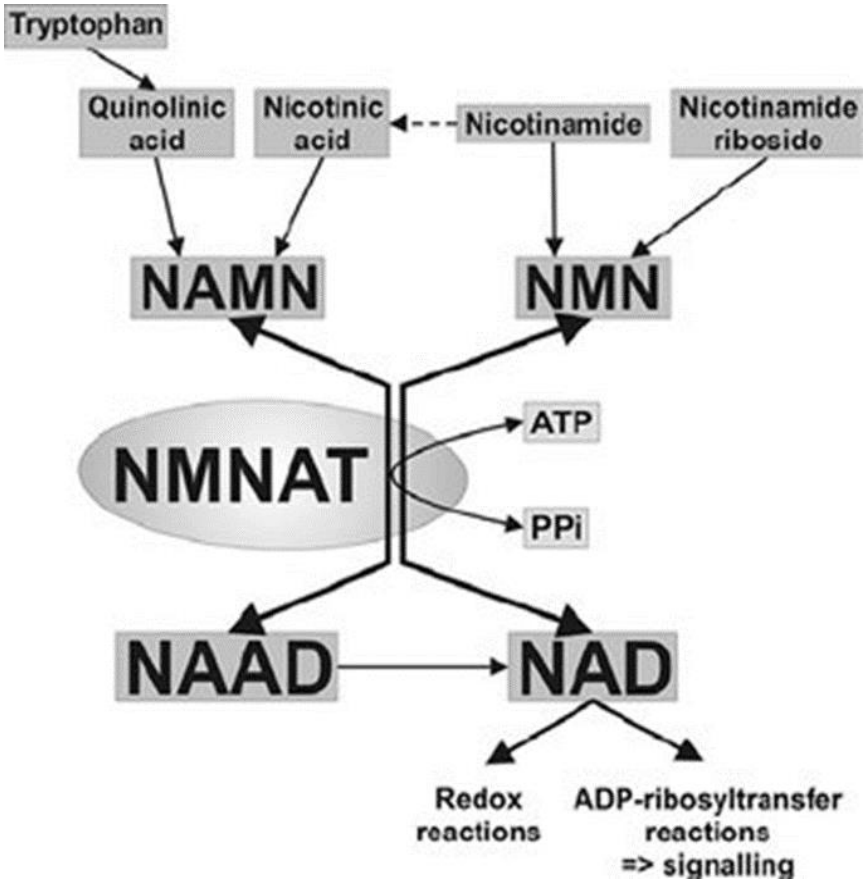

Figure 2.5: Central pathways associated with NAD^+ generation in bacteria

The Figure illustrates NAD^+ production in bacterial cells from aspartate or tryptophan. Through the *de novo* pathway, tryptophan is converted into quinolinic acid which is further converted into NaMN. Using NaMN and ATP as substrates, NNAT, also referred to NMNAT, produces nicotinic acid adenine dinucleotide (NaAD). This can be converted into NAD^+. Through the salvage pathway, NMN is produced via nicotinamide (converted to nicotinic acid) and nicotinamide ribose. NMN and ATP produce NAD^+ in the presence of NNAT. The products of the NNAT reaction are NAD^+/NaAD and inorganic pyrophosphate. NAD^+ is used for redox reactions and signalling in the cell (Lau *et al*., 2009).

2.6 NNAT: Key enzyme in NAD^+ metabolism

NNAT (*EC* 2.7.7.18) is a transferase enzyme with substrates ATP, NMN, nicotinic acid mononucleotide (NaMN) and other nucleotides, aiding in the transferal of the adenylyl moiety of ATP. It forms part of the nucleotidyltransferase α/β phosphodiesterase family (Magni *et al*., 2009). It is comprised of 216 amino acids with a molecular weight of 24.9 kDa and a theoretical isoelectric point (pI) of 5.77. The gene family, *nadD*, is highly conserved within the bacterial group. The family of *nadD* genes work together in various reactions to generate NAD^+. The enzyme catalyses the following reaction.

$$\text{NaMN/NMN} + \text{ATP} \underset{\text{Mg}^{2+}}{\overset{\text{NNAT}}{\rightleftharpoons}} \text{NaAD/NAD}^+ + \text{H}^+ + \text{PP}_i \quad (1)$$

Once NaAD is formed due to the catalysation by NNAT using NaMN as the substrate, it is then amidated by NAD synthase, encoded by *nadE* (Wang *et al*., 2017). Although NNAT can convert NMN directly into NAD^+, the enzyme displays a higher substrate specificity for NaMN over NMN, and produces NaAD at a higher rate (~20 times) than NAD^+ (Wang *et al*., 2017). To date, there is no solved crystal structure of *Kp*NNAT however, sequence alignment analysis revealed a 75% sequence similarity between *Kp*NNAT (Uniprot ID: B5XZR5) to *Escherichia coli* NNAT (*Ec*NNAT) (PDB ID: 1k4k). Thus, revelations made around the *Kp*NNAT structure can be done by analysing *Ec*NNAT until the *Kp*NNAT structure has been solved experimentally.

Secondary structural analysis of *Ec*NNAT, reveals seven β-strands flanked by several α-helices and an α/β/α/β sandwich towards the C-terminal (Zhang *et al*., 2002). The structure has a homologous domain, Rossman-fold, which is characterised by the α/β/α/β sandwich (Zhang *et al*., 2002). The Rossman-fold is a feature of nucleotidyltransferases, adenylyltransferases and cytidylyltransferases and acts as a nucleotide cofactor binding domain (Barbas *et al*., 2013). The secondary structure of *Ec*NNAT is shown in Figure 2.6 alongside the Rossman-fold feature.

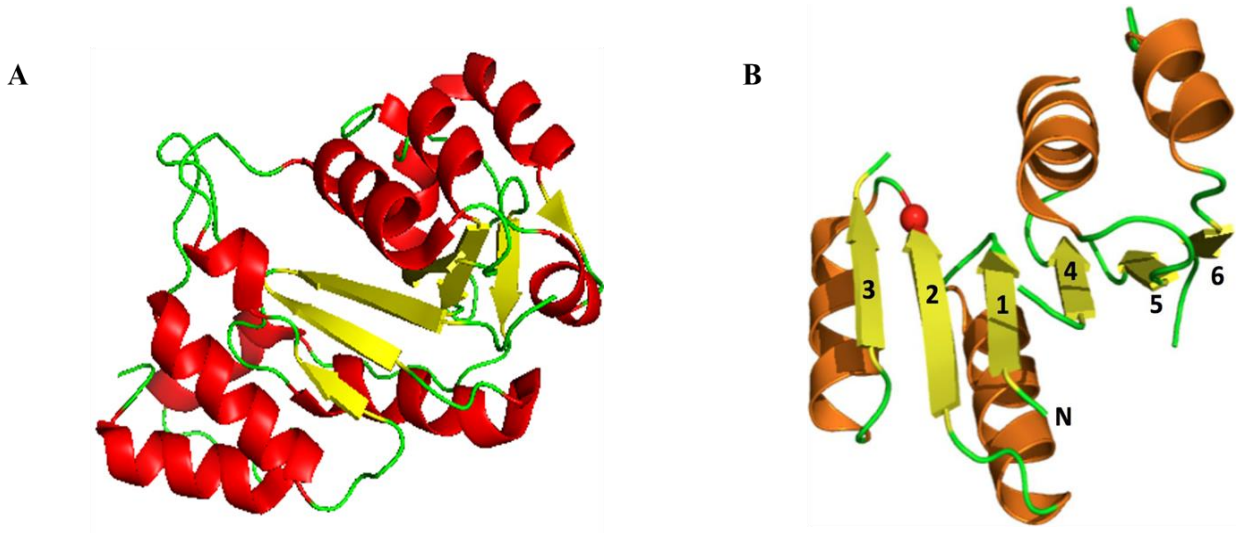

Figure 2.6: Secondary structural depiction of *Ec*NNAT

Figure A shows the secondary structure of *Ec*NNAT (PDB: 1k4k) with β-strands in yellow and α-helices in red. The secondary structure of *Ec*NNAT depicts seven β-strands surrounded by several α-helices. Figure B shows the features of a Rossman-fold which is comprised of six β-strands flanked by several helices (Laurino *et al*., 2016). From Figure A, it is evident that the Rossman-fold is a feature of the *Ec*NNAT secondary structure.

The oligomeric states of NNATs differ between species and show differences between the crystal lattices. The crystal lattice of *Ec*NNAT in its apo-form revealed a tetrameric state consisting of four independent NNAT molecules (Figure 2.7A) (Zhang *et al*., 2002). However, the packing of this lattice indicates that *Ec*NNAT is monomeric in solution since the molecules are independently packed in the lattice. This is supported by gel filtration studies showing that the molecule in apo-form had a molecular weight of 25 kDa indicative of the monomeric form (Zhang *et al*., 2002). The manner in which the molecules are positioned in the asymmetric unit indicated flexibility in certain regions of *Ec*NNAT. Flexibility in these regions aid in substrate binding and product release (Zhang *et al*., 2002). Figure 2.7B depicts *Ec*NNAT and indicates the flexible regions of the enzyme. When complexed to its product NaAD, *Ec*NNAT revealed a different crystal lattice to its apo-form. The crystal lattice (I222) showed three complexed molecules with a 3-fold symmetry. The enzyme still exists as a monomer in solution even though it demonstrates a trimeric crystal lattice packing (Zhang *et al*., 2002). Thus, the trimeric structure does not play a physiological role, it is only as a result of crystal packing (Lau and Niere, 2009). Changes in the specific regions shown in Figure 2.7B are due to the complexed *Ec*NNAT and its association with NaAD. Region 1 (residues 41-48) become less ordered to associate with the NaMN portion of NaAD, Region 2 becomes more ordered (residues 112-120) and Region 3 (looped region) changes its conformation in such a way that citrate can interact with the adenine ring (Zhang *et al*., 2002). Citrate mimics the interactions that *Ec*NNAT would exhibit with ATP (Zhang *et al*., 2002). These changes demonstrate the flexibility of *Ec*NNAT when bound to ligands or products. The active site of *Ec*NNAT and its interactions are shown in Figure 2.8 which highlight the residues that participate in substrate binding during catalysis.

2.7 Overview of *Kp*NNAT structure using a homology model

Using *Ec*NNAT, a predicted homology model for *Kp*NNAT was generated as a result using SWISS-Model and PyMol (Figure 2.9) since *Ec*NNAT and *Kp*NNAT share a 75% sequence similarity (Waterhouse *et al*., 2018) (PyMol.org). The secondary structure of this model is conserved and indicates the presence of a Rossman-fold. Unspecified α-helices or β-strands are slightly shorter or longer compared to its model *Ec*NNAT however, the overall structure seems to be conserved. Thus, the hydrophobic collapse of residues to form these secondary structures is also conserved. These residues (Ala9, Trp95 and others) (Figure 2.11) are not only associated with secondary structures but also play crucial roles in ligand binding (Zhang *et al*., 2002).

A

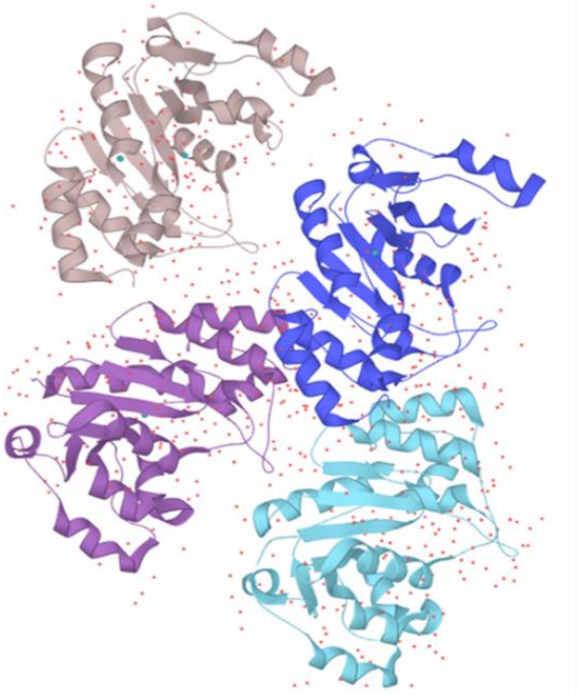

B

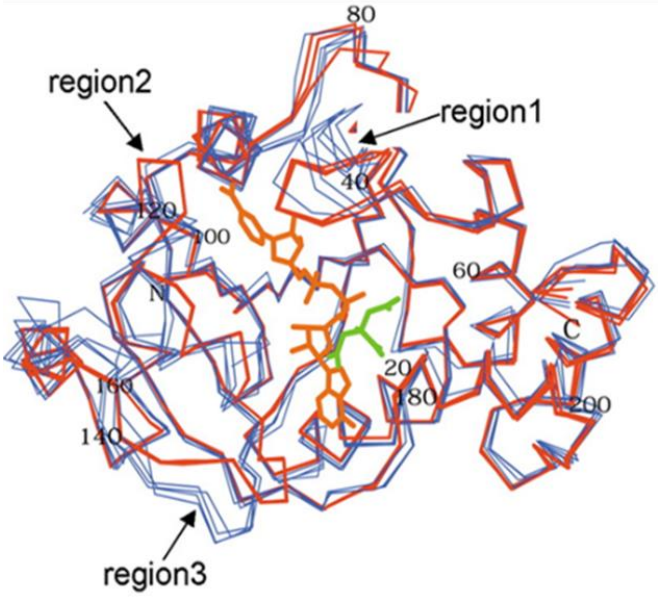

Figure 2.7: Structure of crystal form *Ec*NNAT

Figure A shows the tetrameric crystal lattice of *Ec*NNAT in its apo-form with four independent *Ec*NNAT molecules. Figure B shows the monomeric structure of *Ec*NNAT (with ligands) with the flexible regions numbered. The blue lines represent apo-*Ec*NNAT and the red lines represent complexed *Ec*NNAT with NaAD (red) and citrate (green) (PDB ID: 1k4k) (Zhang *et al*., 2002).

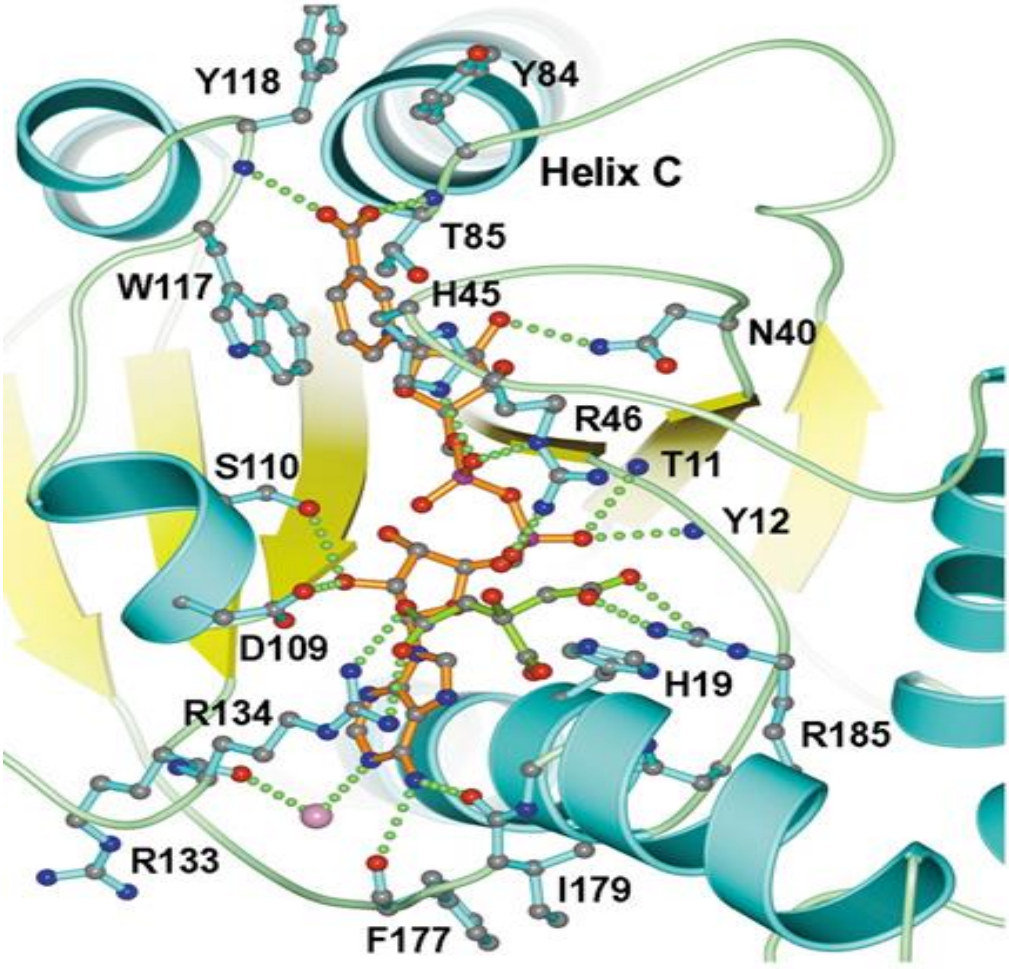

Figure 2.8: Active site of complexed *Ec*NNAT

The figure shows the complexed *Ec*NNAT with NaAD (red balls and yellow sticks) and citrate (red balls and green sticks) and their interactions with the corresponding amino acids which is aided by changes in structure flexibility. The binding of citrate partially mimics the interactions of ATP binding to *Ec*NNAT. Y-tyrosine; T-threonine; W-tryptophan; H-histidine; N-asparagine; R-arginine; S-serine; D-aspartic acid; I-isoleucine; F-phenylalanine (Zhang *et al*., 2002).

Bacterial NNATs have conserved ATP binding motifs for ATP recognition. The conserved sequence (T/HXGH) has been previously shown to aid in the stabilisation of ATP binding and catalysis (Stancek *et al*., 2005). In specific, *Ec*NNAT contains a glycine residue which is associated with binding near the active site (Lau and Niere, 2009). During the catalysed reaction, the α-phosphate of ATP is localised close to magnesium ions found at the active site. The ions aid in the nucleophilic attack and is essential in the promotion of catalysis (Lau and Niere, 2009). The presence of a positively charged residue such as histidine in the active site of *Ec*NNAT is responsible for nucleotidylation of the second substrate (Lau and Niere, 2009). The conserved ATP motif sequence can be seen in Figure 2.11.

Residues such as Trp120, Asp112 and Ser113 are conserved between bacterial species *E. coli* and *K. pneumoniae* (Figure 2.11) and participate in conformational changes once the product (NaAD/NAD^+) is bound (Zhang *et al*., 2002). In addition, Arg137 and Trp179 aid in closing the active site once the product is bound. Conservation of other residues such as His48 and Thr88 are shown to participate in pyridine mononucleotide binding (Zhang *et al*., 2002). They aid in stacking interactions with the pyridine ring whilst creating an anionic pocket for interactions with NaMN/NMN (Wang *et al*., 2017). Apart from the conserved residues, there are several alterations in the amino acid sequence of *Kp*NNAT that may alter the catalytic activity or substrate binding. Tyr118 is replaced with histidine in the predicted model, however since both residues are polar, the binding of exocyclic carboxylates would still occur in a similar manner (Wang *et al*., 2017). Tyr84, an important catalytic residue, is replaced with tryptophan in the predicted *Kp*NNAT model. However, crystallisation studies on *Ec*NNAT show that the role of Tyr84 in certain bacterial NNAT species has similar roles to Trp117 with regard to conformational change due to product binding. (Zhang *et al*., 2002). Irrespective of the variations, this model demonstrates the conservative structure between these bacterial NNATs.

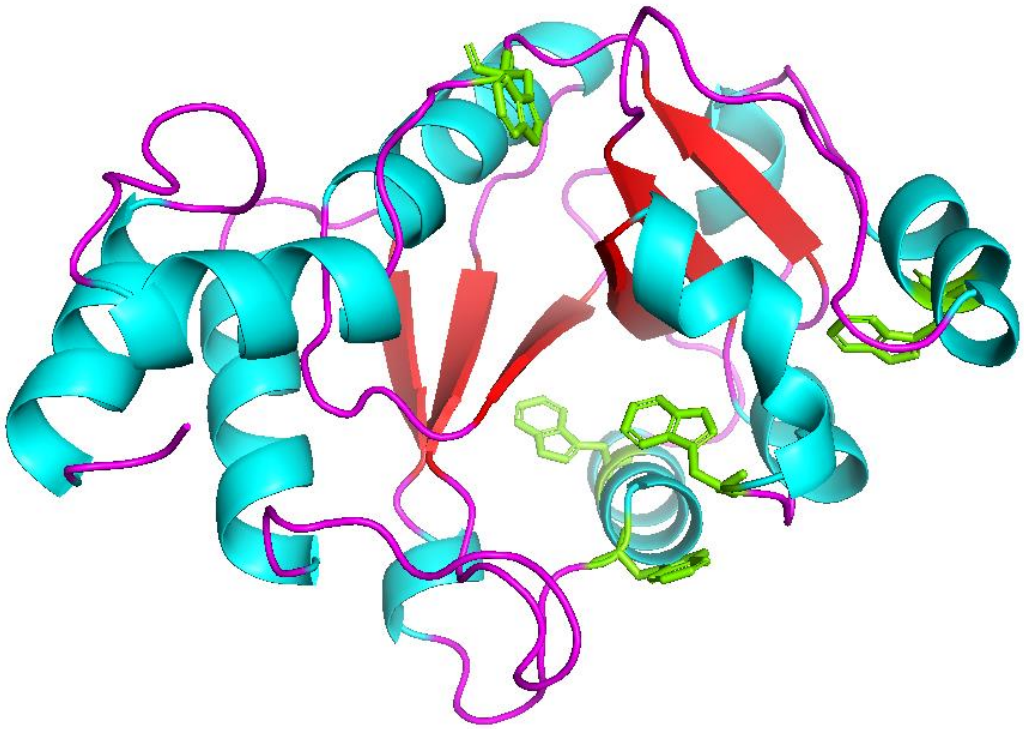

Figure 2.9: Model prediction of *Kp*NNAT using *Ec*NNAT in homology modelling
Using SWISS-Model and the template 1k4k, the above model was built to predict the structure of *Kp*NNAT. Alpha helices are shown in blue; β-strands are shown in red and tryptophan residues are shown as green sticks. The presence of the Rossman-fold can be seen in the predicted model.

2.8 Comparisons of bacterial and human NNATs

NNATs exist across different kingdoms. They are found in bacteria, archaea and eukarya but exhibit vast differences in sequence identity across these kingdoms. Due to the lack of solved *Kp*NNAT crystal structures, structural and functional comparisons cannot be made with respect to *Homo sapien* NNAT (*Hs*NNAT). Thus, *Ec*NNAT which shares a 75% sequence similarity with *Kp*NNAT can be used to compare the NNAT counterparts. Specifically, there is only ~20% sequence similarity between NNATs derived from *H. sapiens* and *E. coli* (Figure 2.12). The major difference in this enzyme between both organisms is the enzyme affinity for its substrate, which can be attributed to significant changes in oligomeric state and active sites (Zhou *et al*., 2002). *Hs*NNAT exhibits a unique equal affinity (no preference) for both substrates NMN and NaMN, whereas *Ec*NNAT exhibits a higher affinity for NaMN (Stancek *et al*., 2005). The differences between the active sites of *Ec*NNAT and *Hs*NNAT are crucial in the specificities of substrates. The *Hs*NNAT active site consists of additional residues such as Lys170, Asp173, Asn273, Leu95, Thr95 and additional water molecules that facilitate substrate binding (Lau *et al*., 2009). These residues and molecules are not conserved in bacterial NNATs and are shown to contribute to the dual affinity experienced by *Hs*NNATs. In particular, the negative charge on Asp173 and the presence of specific water molecules enable the binding of substrates with different electrostatic properties (Lau *et al*., 2009). Furthermore, certain active site residues such as Asn273 are located on an α-helix that is unique to *Hs*NNAT which accommodates dual-specificity (Lau *et al*., 2009). Unlike, *Hs*NNATs, *Ec*NNATs possess an anionic binding pocket which contributes to the higher affinity towards NaMN than NMN. *Ec*NNAT creates an anionic binding pocket via Thr85, Tyr118, Ala86 and His45 to form interactions with NaMN (Zhang *et al*., 2002). The interactions are specific and allow for higher affinity towards NaMN than NMN (Zhang *et al.*, 2002). Thus, the binding sites of NaMN or NMN exhibit major differences between human and bacterial NNATs which is an enticing consideration for drug design.

The *Hs*NNAT monomer consists of six stranded β-sheets compared to *Ec*NNAT which contains seven-stranded β-sheets (Zhou *et al*., 2002). The monomer also possesses additional C-terminus residues which are proposed to play a role in substrate recognition (Zhou *et al*., 2002). The *Hs*NNAT monomer also possesses a special residue sequence called the nuclear localisation sequence (NLS) (Figure 2.11). This sequence is unique to *Hs*NNAT and is responsible for interactions with the nuclear translocation machinery or protein kinase C (Zhou

et al., 2002). Apart from their substrate affinities and sequences, the oligomeric states and crystal lattice packing indicate major differences in *Hs*NNAT compared to *Ec*NNAT (Figure 2.10). *Hs*NNAT exhibits a hexameric state in the crystal structure, a trimer of dimers (Zhou *et al*., 2002). However, crystal structures and further studies prove that *Hs*NNAT exists as multiple oligomeric states in solution, thus it has a tetramer-dimer-hexamer equilibrium in solution (Zhou *et al*., 2002). Unlike *Hs*NNAT, the *Ec*NNAT crystal structure demonstrates four independent molecules (Figure 2.10) indicating monomeric states of *Ec*NNAT in solution (Zhang *et al*., 2002). Thus, the differences in oligomeric states of NNATs in both *H. sapiens* and *E. coli* may lead to differences in the enzyme functionality.

*2.9 Kp*NNAT: Possible target for drug therapy

Although the monomeric units of bacterial and human NNATs are structurally similar, their sequence similarity is very low (~20%). Studies indicate that the substrate specificities, enzymatic activity and active sites of bacterial and human NNATs vary and thus, bacterial NNATs can be used for drug design (Brunetti *et al*., 2010). The preference for NaMN over NMN that is experienced by bacterial NNATs is due to the peculiar anionic binding pocket for the negatively charged NaMN (Garavaglia *et al*., 2002). The human NMN active site does not possess the anionic binding pocket that is present in bacterial NNATs (Zhou *et al*., 2002). Furthermore, the *Hs*NNAT active site consists of a unique Asp173 (shown in Figure 2.10) residue which interacts with conserved water molecules within proximity of the active site. These water molecules contribute to the electrostatic forces within the site which allow *Hs*NNAT to accommodate both NaMN and NMN with dual-specificity (Zhou *et al*., 2002). Thus, the major differences in charge, water molecules and overall binding shape within the active sites of bacterial and human NNATs permit for bacterial NNAT drug design (Sorci *et al*., 2009). In addition, previous drug design studies targeting bacterial NNATs showed no effect on human NNATs, reinforcing the idea of bacterial NNATs as a suitable target for inhibition (Sorci *et al*., 2009).

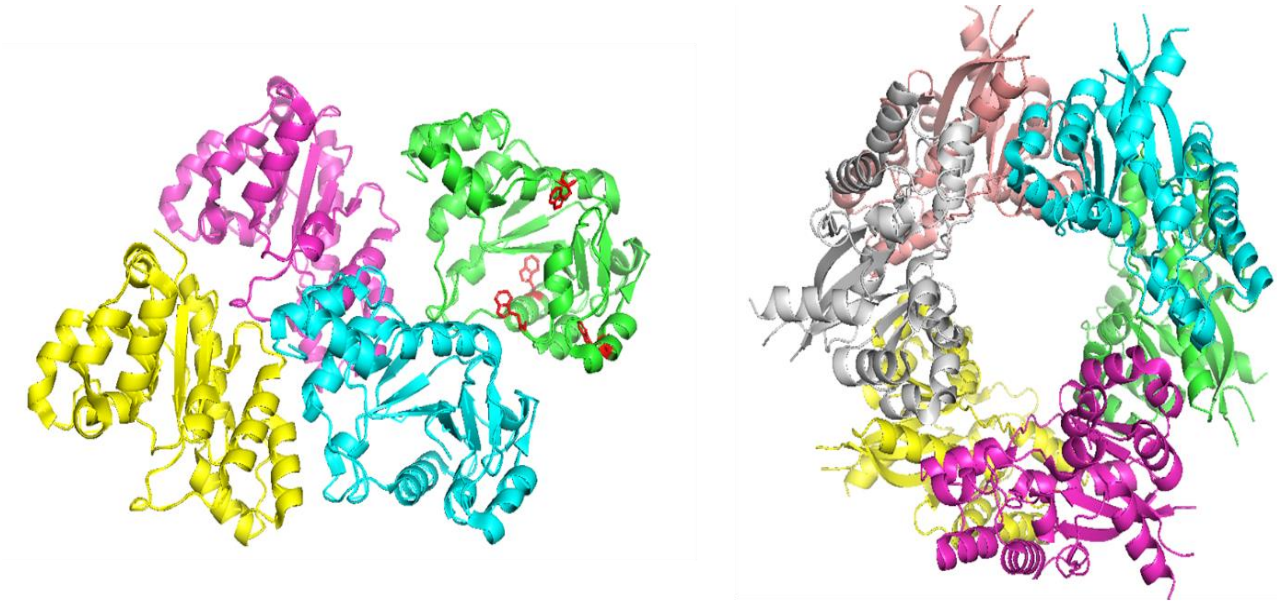

E. coli NaMNAT

H. sapien NaMNAT

Figure 2.10: Crystal structures of *Ec*NNAT and *HsNNAT*

The following enzyme structures were created using Pymol and Protein Data Bank codes (1k4k and 1kqo respectively). The *E. coli* crystal structure shows four independent chains. Tryptophan residues are indicated as sticks and shown on one chain (monomeric). The *H. sapien* crystal structure shows six chains (hexameric) forming a central channel accessing the active sites.

A

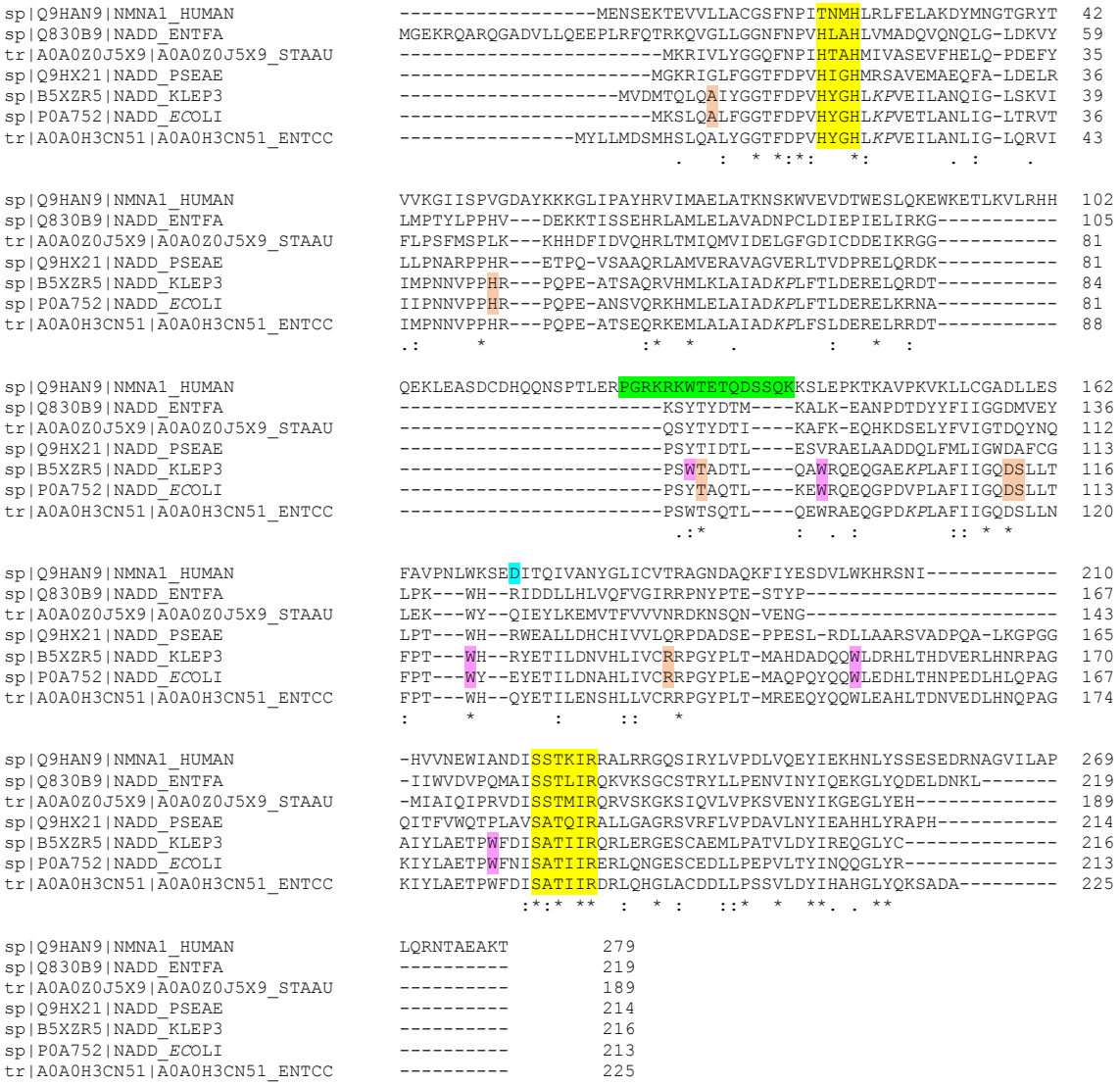

Figure 2.11: Clustal Omega alignments of NNATs derived from various organisms Figure A demonstrates the alignments of NNATs from different organisms using their Uniprot codes and Clustal Omega. NNATs were aligned from NMNA1_HUMAN (*H. sapiens*, Uniprot: Q9HAN9), NADD_ENTFA (*E. faecalis*, Uniprot: Q830B9), STAAU (*S. aureus*, Uniprot: A0A0Z0J5X9), NADD_PSEAE (*P. aeruginosa*, Uniprot: Q9HX21), NADD_KLEP3 (*K. pneumoniae*, Uniprot: B5XZR5), NADD_*EC*OLI (*E. coli*, Uniprot: P0A752) and ENTCC (*E. cloacae*, Uniprot: A0A0H3CN51). The highlighted (yellow) sequences depict the conserved sequences (H/TXXH, SXXXXR) on the N-terminals and C-terminals of all organisms. The highlighted (green) residues represent the unique NLS sequence of *Hs*NNAT. The highlighted (blue) residue (Asp173) represents a unique residue of *Hs*NNAT involved in substrate recognition. NNAT derived from *H. sapiens* possesses a longer sequence with major dissimilarity against NNATs derived from the bacterial organisms. An asterisk (*) represents common residue, a colon (:) represents different amino acid with similar properties and a single dot (.) represents different amino acids with different properties The highlighted (pink) tryptophan (W) residues emphasise the high sequence similarity of *Kp*NNAT and *Ec*NNAT as Trp residues play crucial roles in enzyme function. The highlighted (orange) residues indicate conserved residues between *Kp*NNAT and *Ec*NNAT that participate in enzymatic activity.

	1	2	3	4	5	6	7
1: sp|Q9HAN9|NMNA1_HUMAN	100.00	23.38	22.22	21.29	24.14	23.50	21.90
2: sp|Q830B9|NADD_ENTFA	23.38	100.00	38.62	37.70	37.70	38.30	35.50
3: tr|A0A0Z0J5X9|A0A0Z0J5X9_STAAU	22.22	38.62	100.00	29.79	26.20	26.74	26.60
4: sp|Q9HX21|NADD_PSEAE	21.29	37.70	29.79	100.00	37.91	37.91	36.45
5: sp|B5XZR5|NADD_KLEP3	24.14	37.70	26.20	37.91	100.00	75.12	76.39
6: sp|P0A752|NADD_*EC*OLI	23.50	38.30	26.74	37.91	75.12	100.00	78.40
7: tr|A0A0H3CN51|A0A0H3CN51_ENTCC	21.90	35.50	26.60	36.45	76.39	78.40	100.00

Figure 2.12: Percentage sequence similarity of NNAT between various organisms
The percentages are represented in the order 1:1, 1:2, 1:3, 1:4, 1:5, 1:6 and 1:7 where 1 represent *H. sapiens*. *Hs*NNAT shares a very low sequence similarity with NNATs derived from bacterial species (<25%). NNATs were aligned from NMNA1_HUMAN (*H. sapiens*, Uniprot: Q9HAN9), NADD_ENTFA (*E. faecalis*, Uniprot: Q830B9), STAAU (*S. aureus*, Uniprot: A0A0Z0J5X9), NADD_PSEAE (*P. aeruginosa*, Uniprot: Q9HX21), NADD_KLEP3 (*K. pneumoniae*, Uniprot: B5XZR5), NADD_*EC*OLI (*E. coli*, Uniprot: P0A752) and ENTCC (*E. cloacae*, Uniprot: A0A0H3CN51). The shaded percentage (24.14%) represents the low sequence similarity between *H. sapien* and *K. pneumoniae*.

CHAPTER 3:

MATERIALS AND METHODS

3.1 Materials

The following materials were supplied by Sigma-Aldrich: yeast, tryptone, ampicillin, isopropyl β- d-1-thiogalactopyranoside (IPTG), GSH, thrombin, imidazole, Trisma, glycerol, Sodium Dodecyl Sulphate (SDS), N,N,N',N'-tetramethyethylenediamine (TEMED), glycine, β-mercaptoethanol, Coomassie Brilliant Blue R-250, urea, ANS, NMN, ATP, ADH, Magnesium chloride ($MgCl_2$,) sodium phosphate monobasic, NAD^+, mant-ATP, Tris (2-carboxyethyl) phosphine (TCEP), Snakeskin^{TM} dialysis membrane. The following materials were supplied by Bio-Rad: molecular weight marker (MWM) (BLUeye Prestained Protein Ladder), electrophoresis casting apparatus. The following materials were supplied from the New England Biolab, USA: T7 *E. coli* cells. The following materials were supplied from GenScript, USA: pGEX-4T-1 plasmid.

3.2 Methods

3.2.1 Plasmid design and synthesis

The synthetic gene (Gene ID 11846511, GenBank) was cloned into a pGEX-4T-1 vector for overexpression. All sequencing was done by Inqaba Biotech (Pretoria, South Africa) and produced by GenScript to incorporate a hexahistidine tag upstream the *Kp*NNAT ORF sequence. Messenger ribonucleic acid (mRNA) was re-coded to be harmonised with codon usage frequency in *E. coli*. The synthesized gene was then incorporated into a pGEX-4T-1 vector for overexpression in *E. coli* T7 cells. This vector contains features such as a GST fusion tag, a multiple cloning site (MCS) and a thrombin cleavage site which are shown in Figure 3.1. Its expression system consists of a Ptac promoter, *lacI* repressor and ampicillin resistance gene. Since a GST fusion tag vector is used, *Kp*NNAT possessed a GST tag (N-terminus) which was removed prior to protein characterisation and assays. This tag removal was achieved using thrombin which acts at the thrombin cleavage site (Shimon *et al*., 2015). A major advantage of using the pGEX vector lies in its possession of the GST-encoding region which simplifies the protein purification procedure and solubility of the expressed protein. GST fusion tags act as chaperones aiding in protein folding and solubility (Harper and Speicher, 2011).

A

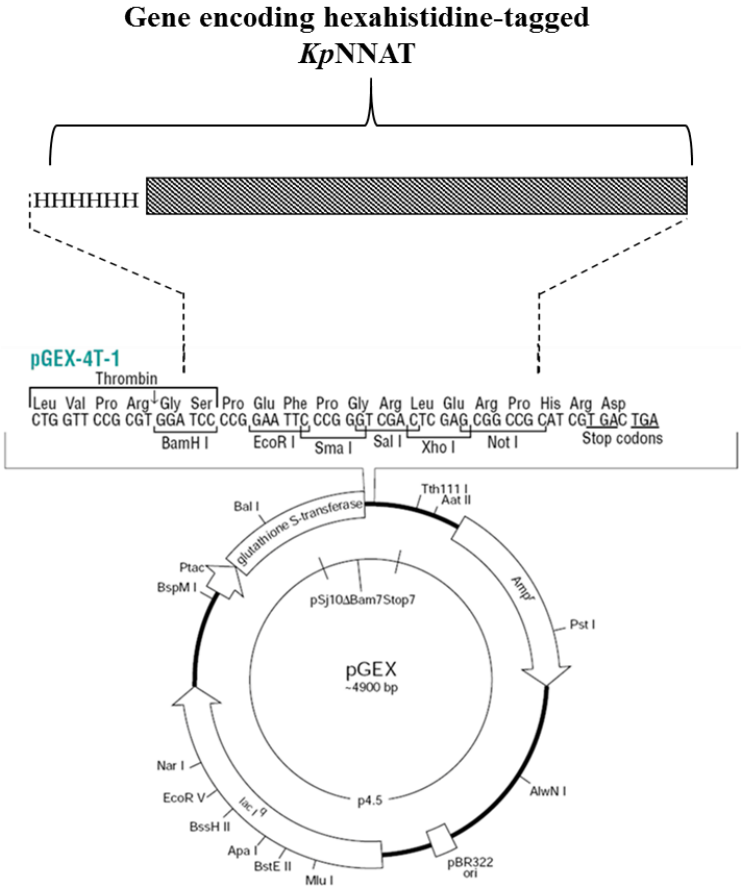

B

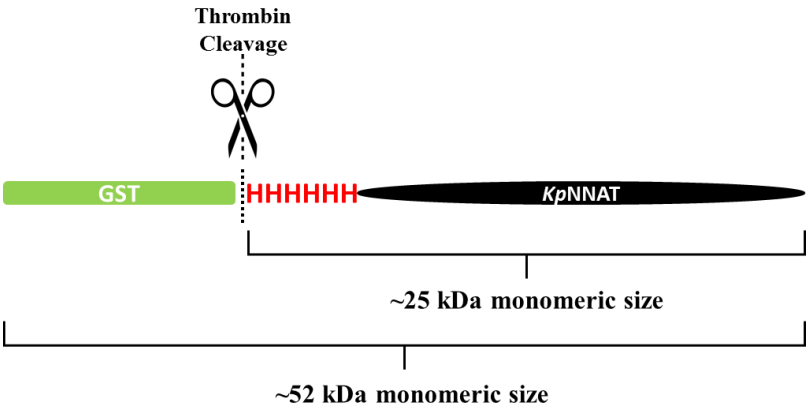

Figure 3.1: Vector map of pGEX plasmid

The vector map of a pGEX-4T-1 plasmid is illustrated in A with the additional tags. GSH-Glutathione, H-Histidine. Thrombin recognition sequence is indicated by the arrow between the arginine and glycine residue. Figure B shows an illustration demonstrating the expressed product consisting of a GST tag, hexahistidine tag and *Kp*NNAT with a total monomeric molecular weight of ~52 kDa. Thrombin cleavage results in a hexahistidine-tagged *Kp*NNAT with a monomeric molecular weight of ~25 kDa.

3.2.2 Recombinant protein expression

E. coli cells were chosen as a system of expression due to their rapid growth; high cell density achievement and the transfer of exogenous materials is time-efficient (Rosano and Ceccarelli, 2014). Due to these advantages, *E. coli* is a popular recombinant expression system. The selectivity of protein expression is achieved using specific antibiotics. Since the pGEX-4T-1 vector contains an ampicillin resistance gene, the presence of ampicillin during recombinant expression allows for the selectivity of bacterial cells that contain the appropriate plasmid (Bennett, 2008).

T7 *E. coli* cells were transformed with the vector encoding GST and hexahistidine-tagged *Kp*NNAT and was subjected to expression. The T7 *E. coli* cells and SOC media (super optimal broth) [2% (w/v) tryptone, 0.5% (w/v) yeast, 10 mM NaCl, 2.5 mM KCl, 10 mM $MgCl_2$ and 20 mM glucose] were defrosted on ice. Once defrosted, 1 µL of the pGEX-4T-1 plasmid (with the gene of interest) was added to the T7 *E. coli* cells and was incubated on ice for 30 min. For 45 seconds, the cells were heat shocked at 42 °C to enable permeability of the cell wall to allow the plasmid to enter. SOC media (950 µL) was then added to the transformed cells. The media was incubated at 230 rpm for 90 min at 37 °C to allow for bacterial growth. Thereafter, 200 µL of cells were spread onto a petri dish containing set lysogeny broth (LB) agar containing 50 µg/mL ampicillin for antibiotic selectivity. The dish was incubated overnight at 37 °C.

Single colonies were selected and cultured overnight in 2 × yeast tryptone (2 × YT) media (37 °C for 16 hrs, 220 rpm) augmented with 50 µg/mL of ampicillin. The overnight culture was diluted 1:50 with 2 × YT media augmented with 50 µg/mL of ampicillin (37 °C, 220 rpm) until an optical density at 600 nm (OD_{600}) was approximately 0.5. The cultures were then incubated at 4 °C for 30 min. Cultures was then subjected to the corresponding IPTG inductions (0 mM-1 mM) and was incubated (20 °C for 16 hrs, 220 rpm) for expression trials. IPTG acts as a non-hydrolysable analogue of lactose to induce the gene expression (Rosano and Ceccarelli, 2014). Cell harvesting was performed using centrifugation (5000 × *g*, 4 °C for 15 min). Cells were resuspended in phosphate buffer saline (PBS) (137 mM NaCl, 2.7 mM KCl, 10 mM Na_2HPO_4, 2 mM KH_2PO_4, pH 7.4) using a ratio of 1:125 [buffer to cell culture (prior to centrifugation)] and was incubated (-80 °C for 16 hrs) to facilitate cell lysis. Frozen cells were thawed at room temperature (20 °C) and thoroughly sonicated before centrifugation (25000 × *g*, 4 °C for 30 min). The resulting soluble and insoluble fractions were analysed using

electrophoresis. Thereafter, subsequent protein expression was performed using the optimal IPTG concentration of 0.5 mM.

3.2.3 Protein purification

To purify a GST-tagged protein, one of the most efficient purification techniques is the GSH-Agarose affinity chromatography. Affinity chromatography is a purification technique based on highly specific interactions between enzymes and substrates, antigens and antibodies or ligands and receptors (Acikara *et al*., 2013). Soluble GST-tagged proteins are purified using an immobilised glutathione column, based on the interaction between GST and reduced GSH. Studies show that the tyrosine residue of GST interacts with GSH via hydrogen bonding with the sulphur group of GSH (Angelucci *et al*., 2005). Due to this interaction, purification is achieved since GST-tagged proteins will be attached to the immobilised column until eluted. Elution can be performed by the addition of GSH to the column, which binds the GST tag and is released from the matrix. Alternatively, glycine at low pH levels (pH 2-3) or high pH levels (pH 9-11) disrupts the bonding between the immobilised matrix and GSTs, thus, can be used to elute GST from the matrix (Narhi *et al*., 1997). An advantage of conducting this type of purification is the specificity of the substrate and enzyme complex, permitting the specific binding GST-tagged proteins to the column, resulting in a high yield of tagged protein (Angelucci *et al*., 2005). The pGEX-4T-1 vector used for the recombinant expression of *Kp*NNAT contains a GST tag and thrombin site for enzymatic cleavage. These tags can be enzymatically removed using thrombin which is facilitated by the thrombin site on the vector. Thrombin, a serine protease, cleaves between arginine and glycine residues thus removing the GST tag, releasing the recombinant protein (Waugh, 2011). However, a concern surrounding thrombin cleavage is the non-specific cleavage that occurs in secondary sites (Rajalingam *et al*., 2008).

Since the expressed enzyme contained an additional hexahistidine tag, further purification of *Kp*NNAT could be achieved. Proteins that possess histidine tags enable further purification by IMAC. Due to specific interactions within the IMAC column, a greater yield of purified protein can be achieved. The principle of IMAC is the association between metal ions (cobalt, nickel, zinc or copper) on immobilised matrices and the side chains of amino acids (Bornhorst and Falke, 2000). Due to the possession of the imidazole ring, histidine strongly interacts with metal ions as electron donor groups on the ring and readily forms bonds with the metal ions. The hexahistidine-tagged proteins are thus bound to the matrix until elution occurs via a change in

pH or the addition of imidazole (Bornhorst and Falke, 2000). The functionality and structure of the protein remain unaltered since the size of the hexahistidine tag is almost negligible (Majorek *et al*., 2014).

The soluble fraction derived from centrifugation was exposed to a gravity flow GSH-Agarose affinity resin to permit the binding of the GST tag to the column. Before passing the soluble fraction to the column, PBS equilibration buffer (137 mM NaCl, 2.7 mM KCl, 10 mM Na_2HPO_4, 2 mM KH_2PO_4, pH 7.4 with 0.5 % Tween-20-PBS) was passed through the column. Thereafter, the soluble fraction was passed through the column and the flow-through was collected. The column was further equilibrated with the PBS buffer (with and without Tween-20-PBS). Once the column was drained, the PBS buffer (1 × column volume) was introduced into the column in addition to 22 µL of thrombin (per 1 litre of media) for the cleavage of the GST tag. The column was secured and rotated gently overnight (16 hrs) at room temperature (20 °C).

The GSH column was then connected to a gravity flow Ni^{2+}-IMAC column. The contents from the on-column cleavage within the GSH-Agarose column had flowed directly into the Ni^{2+}-IMAC column. The flow-through was immediately retrieved from the IMAC column. After the equilibration of both columns with PBS buffer (without Tween-20-PBS), the protein of interest was eluted with an elution buffer (PBS buffer with 500 mM imidazole) with a flow rate of 3 mL/min. Eluted fractions were assessed for protein presence by the addition of 450 µL Bradford dye [6% β-mercaptoethanol (v/v), 10% SDS (w/v), 30% glycerol (v/v), 0.05% Bromophenol Blue, 150 mM Tris-HCl, pH 7.0] to 50 µL of eluted volume per fraction. After elution, the two columns were disconnected, and a further elution of the GSH-Agarose column was performed (PBS buffer with 5 mM GSH) and eluted fractions were collected. The quality (enzyme purity) and indirect quantity (based on band thickness) of purified protein was analysed using gel electrophoresis.

To initially analyse the purification and cleavage of *Kp*NNAT using the GSH-Agarose column, the protein was eluted using 5 mM GSH in PBS buffer (137 mM NaCl, 2.7 mM KCl, 10 mM Na_2HPO_4, 2 mM KH_2PO_4, pH 7.4) prior to thrombin cleavage. The eluted fractions were collected and analysed using electrophoresis and was then subjected to off-column cleavage to investigate the optimal cleavage time interval. To conduct the thrombin cleavage trials, 480 µL of uncleaved *Kp*NNAT (1-2 mg/mL) was subjected to 2 µL of thrombin. After the respective

time intervals, 50 µL of the cleaved sample was added directly to 50 µL of reducing sample buffer (RSB) for Sodium dodecyl sulphate polyacrylamide gel electrophoresis (SDS-PAGE) analysis. The early elution of the GSH-Agarose column prior to cleavage followed by off-column cleavage was done solely for investigative analysis regarding the optimisation of these techniques. All subsequent purifications were performed using on-column cleavage and permitted the direct flow of contents between the dual affinity columns.

3.2.4 SDS-PAGE analysis of KpNNAT purity

SDS-PAGE is a simple way to confirm the quality and indirect quantity of proteins. The technique is based on the principle in which charged molecules move through a gel matrix under the influence of an electric field (Manns, 2011). SDS, an anionic detergent, is comprised of a hydrophobic chain and polar sulphate head and interacts with proteins via positively charged and hydrophobic residues (Jafari *et al*., 2018). Additionally, it confers an overall negative charge (in proportion to protein length) to the protein due to its anionic nature and unfolds protein molecules. However, the disulphide bonds of the protein remain intact. The addition of β-mercaptoethanol aids in the disruption of these disulphide bonds (Parakhia, 2009). In the presence of an electric current, all molecules can migrate to the positively charged electrode (anode) at different rates depending on their molecular weight. Molecules with higher molecular weights migrate slower due to restraint from the gel pore size (Moosavi-Movahedi, 2005). Thus, information regarding protein size and quality can be explored through electrophoresis. Glycine SDS-PAGE is commonly used in protein studies for analysis due to its rapid outcomes and the vivid visualisation of proteins (Laemmli, 1970).

Assessment of protein purity was accomplished by performing a glycine SDS-PAGE and further allowed for the estimation of protein molecular weight using a molecular weight ladder. The components of the gel were prepared as follows: monomer solution [30% (w/v) acrylamide, 2.7% (w/v) bis-acrylamide], separating buffer [1.5 M Tris-HCl, pH 8.8], stacking buffer [500 mM Tris-HCl, pH 6.8], 10% SDS (w/v) and 10% (w/v) ammonium persulfate (APS) initiator reagent. The table below indicates the amount of each ingredient required to produce the gel.

Table 3.1: Components of a glycine SDS-PAGE gel

Reagents	Separating Gel (12.5%)	Stacking gel (4%)
Monomer Solution	6.25 mL	940 µL
Separating Buffer	3.75 mL	-
Stacking Buffer	-	1.75 mL
SDS (10%)	150 µL	70 µL
Distilled Water	4.75 mL	4.3 mL
APS	75 µL	35 µL
TEMED*	15 µL	15 µL

*TEMED to be added last, before gel casting.

The SDS-PAGE samples were produced using a 1:1 ratio of 50 µL sample and 50 µL RSB [125 mM Tris-HCl, 4% (w/v) SDS, 20% (v/v) glycerol, 10% (v/v) β-mercaptoethanol, pH 6.8]. All samples were centrifuged at high speed for 1.5 min. To the wells of the gel, 15 µL of each sample was added alongside the MWM (Bio-Rad). The gel was placed in a cassette in tank (1x) buffer [25 mM Tris, 0.192 M glycine, 10% SDS (w/v), pH 8.3 (unadjusted)]. The gel was electrophoresed at 120 V for 1.5 hrs until the dye front was 0.5 cm from the gel edge. Coomassie stain [0.2% Coomassie Brilliant Blue R in 1:5:4 (v/v/v) acetic acid: methanol: distilled water] was used to soak the gel (30 min) after electrophoresis to enable band visualisation. A destain solution [1:5:4 (v/v/v) acetic acid: methanol: distilled water] was consequently used to soak the stained gel to aid in band visualisation. A standard curve using the retention factor (R_f) was created to determine the weights of specific bands on the SDS-PAGE gels. A linear relationship occurs between the logarithm of the molecular weight of the denatured protein and its R_f (Parakhia, 2009). The equation used to calculate the factor is shown below (2):

$$R_f = \frac{\text{Distance travelled by molecule}}{\text{Distance travelled by dye front}} \quad (2)$$

The enzyme was then subjected to absorbance at 260 nm (detection of nucleic acids) and 280 nm to attain a ratio of $A_{260/280}$. This was performed using 1 µL of random eluted fractions. The NanoDrop (Thermo Scientific NanoDrop 1000) was used to calculate this ratio. Additionally, a protein absorbance spectrum was created by subjecting the protein to absorbance at 280 nm for protein detection and 340 nm for protein aggregation.

3.2.5 Concentration determination of KpNNAT

Quantification of *Kp*NNAT was performed by using absorbance spectroscopy and the Beer-Lambert law. A dilution series of *Kp*NNAT in PBS buffer (137 mM NaCl, 2.7 mM KCl, 10 mM Na_2HPO_4, 2 mM KH_2PO_4, pH 7.4), was done to create the following dilutions: 0.05, 0.025, 0.0125, 0.00625, 0.00312, and 0.00156. Using a Jasco V-630 spectrophotometer, the absorbance of each sample at 280 nm and 340 nm was measured. Absorbance at 280 nm was used for the detection of protein while the absorbance at 340 nm detects aggregation. The data was corrected using blanks (sample of PBS buffer) and by subtraction of the A_{340} readings from the samples. A linear regression line was fitted to the data and by using the gradient/slope from the trendline, the value could be fitted into the Beer-Lambert law equation (3) as shown in equation (4) below to determine the concentration of *Kp*NNAT.

$$A = \varepsilon c l \tag{3}$$

where A is absorbance, ε represents molar extinction efficient (38055 M/cm) according to ProtParam (Gasteiger *et al*., 2005) (Uniprot ID: B5XZR5), c is the concentration (M) and l is path length (cm).

$$\text{Protein concentration} = \frac{\text{Molecular weight} \times \text{Slope}}{\varepsilon \times \text{Path length}} \tag{4}$$

where concentration is represented in mg/mL, molecular weight is represented in Daltons and the path length is 1 cm at 20 °C.

3.2.6 Dual enzyme activity assay of KpNNAT

Coupled enzymatic assays are characterised by the presence of two or more enzymes in biochemical reactions (Uhr, 2010). During these assays, the product/s of the first reaction acts as a substrate for the second reaction in order to produce an additional product which is easily detectable through various techniques such as fluorescence (Uhr, 2010). Unlike single reactions, coupled assays exhibit a lag phase (pre-steady-state) until the steady-state phase is attained (formation and conversion of the intermediate remain constant) (Bisswanger, 2014). The lag phase can be described as a hyperbolic function of the enzyme concentration during the enzyme assay (Ösz *et al*., 2005). Optimal conditions for coupled enzyme assays cannot be achieved for all present enzymes as the first enzyme for the primary reaction determines the

assay conditions since the primary product needs to be formed at an optimal rate (Bisswanger, 2014).

The use of steady-state enzyme kinetics can be used to interpret data attained from coupled enzyme assays from the rate laws that it provides. Steady-state kinetics is the assumption that the concentration of enzyme-substrate complex reaches a constant value, that is, the enzyme-substrate intermediate forms as quickly as it disappears once product formation occurs (Garrett and Grisham, 2008). The equations below indicate derivation of the enzyme kinetics by McClure (1969) for coupled enzyme reactions (Wagner, 1976):

Overall reaction sequence:

$$A \xrightarrow[k_1]{E_1} S \xrightarrow[k_2]{E_2} P$$

(5)

where A represents a substrate, S represents an intermediate substrate complex, P represents a product, E_1 and E_2 represents enzyme 1 and enzyme 2 respectively, k_1 and k_2 represent rate constants for the respective reaction. The steady-state kinetics for this coupled reaction can be expressed as follows:

$$\frac{d[S]}{dt} = k_1 - k_2[S]$$

(6)

Thus, the intermediate substrate complex (S) at steady-state can be re-expressed as:

$$[S]_{ss} = \frac{k_1}{k_2}$$

(7)

Equation (7) can be expressed as above since the following is true for this reaction:

$$v_1 = k_1$$
$$v_2 = k_2[S]_{ss}$$

(8)

where v_1 and v_2 represent the velocity of reaction 1 and 2 respectively.

A coupled enzyme assay is only valid if specific conditions are met. These are: irreversible zero-order primary reaction, implying there is no effect on the initial rate of reaction and an irreversible first-order secondary reaction, implying effects on the initial rate of reaction due to reactant concentrations (Wagner, 1976).

The rate at which an enzyme catalyses the conversion of its substrates is dependent on various factors such as pH, temperature, ionic strength, metal ion requirements and enzyme activity. In order to test the activity or functionality of enzymes, assays are conducted to measure the rate at which a product is produced by catalysation. Enzyme activity is paramount in structural biochemistry to analyse enzyme structure and thus, enzyme function. The following reaction is catalysed by *Kp*NNAT in this assay. The structures of the reaction can be seen in Figure 3.2.

$$\mathrm{NMN + ATP} \underset{\mathrm{Mg^{2+}}}{\overset{\mathbf{NNAT}}{\rightleftharpoons}} \mathrm{NAD^+ + H^+ + PP_i} \qquad (9)$$

Upon the investigation of *Kp*NNAT activity, the product of its reaction, NAD^+, poses a challenge in detection. NAD^+ displays an absorbance maximum only at 250 nm. Both NADH and nucleotides exhibit an absorbance maximum around the same wavelength (250 nm), causing difficulty in NAD^+ detection (Coremans and Bruining, 1992). Unlike its oxidised form, NADH exhibits an additional absorbance at ~340 nm due to its reduced nicotinamide ring (Coremans and Bruining, 1992). Due to this feature, the activity assay of *Kp*NNAT can be performed via NADH detection. Once catalysed by *Kp*NNAT, the product of the reaction, NAD^+, can be converted into NADH by an additional enzyme, ADH. This enzyme is responsible for the catalysis of alcohol, such as ethanol, to an aldehyde, producing NADH as a by-product which can then be detected at 340 nm as shown in equation (10) (Plapp, 2010). The presence of two enzymes in an assay produces a dual enzyme assay.

$$\mathrm{NAD^+} \xrightarrow[\text{ethanol}]{\text{ADH}} \text{NADH + acetaldehyde} \qquad (10)$$

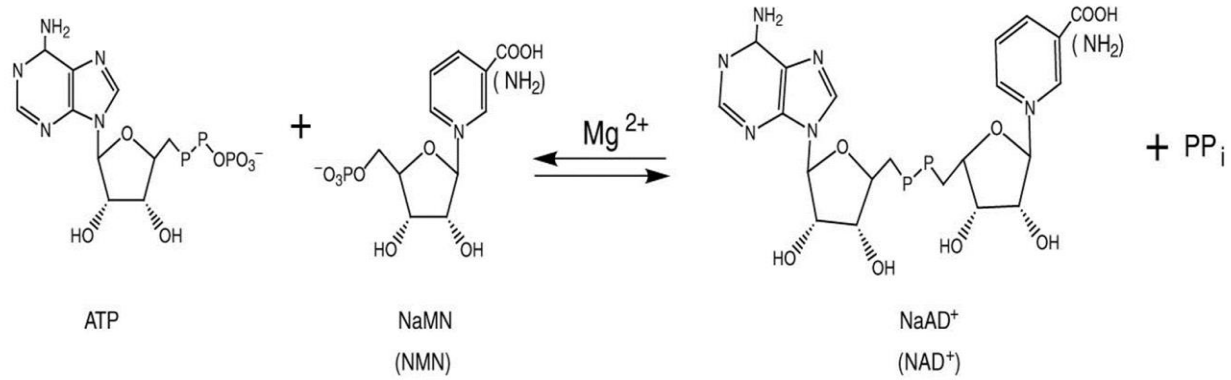

Figure 3.2: A structural depiction of NNAT catalysis

The reaction catalysed by NNAT is shown with all substrates and products in their respective structural forms. NNAT catalyses substrates NMN and ATP to produce NAD^+ and inorganic pyrophosphate. The reaction catalysed by NNAT proceeds via a nucleophilic attack by the 5' phosphate of the mononucleotide on the α-phosphate of ATP to produce NAD^+ (D'Angelo *et al*., 2000).

3.2.6.1 pH-dependent activity assay

An important factor that influences an enzyme's ability to optimally catalyse a reaction is the pH of a reaction. The activity of most enzymes follows a bell-shaped pattern with regard to pH levels, that is, low activity in strong acidic regions and strong alkaline regions (Bisswanger, 2014). Many enzymes exhibit optimal pH levels within the physiological range of pH 7.5. The effects of pH are due to the protonation of amino acid functional groups and the native structure of the enzyme (Bisswanger, 2014).

Coupled enzyme assay conditions such as pH, are difficult to optimise since more than one enzyme are present. Thus, a pH activity assay can be performed to investigate the optimal pH range for the assay comprising of dual enzymes. To investigate the effect of pH levels on this enzymatic assay, a series of assays with varied pH values were performed. A 3 mL sample was prepared as follows for each buffer: 10 units/mL ADH, analytical grade ethanol [1% (v/v)], 5 mM $MgCl_2$, 1 mM ATP and 0.8 μM *Kp*NNAT in the appropriate buffer. To start the reaction, 2.9 mL of the sample was added to a final concentration of 0.5 mM NMN. The following buffers were prepared and used for the assays: 0.1 M acetate buffer (pH 5.5), 0.1 M phosphate buffer (pH 6-8), 0.1 M Tris-HCl buffer (pH 8.5- 9) and 0.1 M Na-glycine buffer (pH 9.5-10.5). For each sample in the appropriate buffer, a blank was accounted for (10 units/mL ADH, analytical grade ethanol (1%), 5 mM $MgCl_2$, 1 mM ATP and 0.5 mM NMN in the appropriate buffer). The assay was performed in triplicates by using the Jasco V-630 spectrophotometer (Analytical Solutions) with a data pitch of 0.5 for 60 seconds. The produced NADH was spectrophotometrically monitored at 340 nm for 60 seconds at approximately 20 °C.

Once the optimal pH level range for the *Kp*NNAT activity assay was investigated, the activity assay was carried out at two different pH conditions to gain insight into the difference in activity at different pH units. A standard 3 mL sample contained *Kp*NNAT (varied concentrations), ATP (1 mM), NMN (0.5 mM), ADH (10 units/mL), $MgCl_2$ (5 mM) in the appropriate buffer containing 1% (v/v) analytical grade ethanol. Concentrations of *Kp*NNAT varied from 0 nM to 1.6 μM. The assay was repeated at two pH units, pH 7.5 (phosphate buffer) and pH 9.0 (Tris-HCl buffer). Appropriate blanks were used (sample contained 1 mM ATP, 0.5 mM NMN, ADH (10 units/mg), 5 mM $MgCl_2$ in the appropriate buffer with 1% analytical grade ethanol (99%). The dual reaction produced NADH as a by-product which is an indirect measurement of *Kp*NNAT activity. The produced NADH was spectrophotometrically monitored at 340 nm for 60 seconds at approximately 20 °C using the Jasco V-630

spectrophotometer (Analytical Solutions). The experiment was performed in triplicates and the data was averaged. A linear regression plot was created using the gradients from each *Kp*NNAT concentration. The gradient of the linear plot was accepted as the pseudo-specific activity of *Kp*NNAT.

3.2.7 Structural Studies

3.2.7.1 Secondary structural content analysis

The secondary structure of proteins is produced by stabilised regions of hydrogen bonding between atoms of the carbonyl oxygen and the amino hydrogen of a polypeptide backbone (Rehman and Botelho, 2018). The pattern in which the backbone folds gives rise to secondary structural features such as α-helices or β-sheets (Rehman and Botelho, 2018). A popular technique used for determination of protein secondary structure is far-UV CD. This technique measures absorption differences in left-handed (anti-clockwise rotation) and right-handed (clockwise rotation) polarised light due to structural asymmetry (Greenfield, 2006). In the far-UV region (190 nm-250 nm), the chromophores of the amide bonds of protein backbones are aligned, but change in transitions when excited (Greenfield, 2006). These changes produce unique spectra characterising the various secondary structures of proteins which can be seen in Figure 3.3. The simplicity and inexpensive nature of the technique favours its use for secondary structural analysis. CD is a technique that produces rapid results which can be easily analysed in a variety of conditions. However, data from CD does not quantify secondary structural features, thus algorithms such as Dichroweb can be used. The online tool enables quantification of experimental data for secondary structural analysis. The algorithms deconvolute the data in comparison to built-in reference protein sets and produce an analysis report quantifying the α-helices, β-sheets, random coils and unordered structures of a protein (Whitmore and Wallace, 2004).

To determine the overall predominant secondary structural features of *Kp*NNAT, far-UV CD was performed using the Jasco J-1500 CD spectrometer (Analytical Solutions) with a data pitch of 0.5, scanning speed of 100 nm/min and bandwidth of 2.5 nm. The analysis was performed on native (5 µM *Kp*NNAT) and denatured (5 µM *Kp*NNAT with 8 M urea) samples in filtered phosphate buffer (5 mM sodium phosphate monobasic, pH 7.4) at approximately 20 °C. Blank samples were used and subtracted where appropriate: native blank (filtered PBS buffer) and denatured blank (8 M urea in filtered PBS buffer). The plots were analysed for secondary

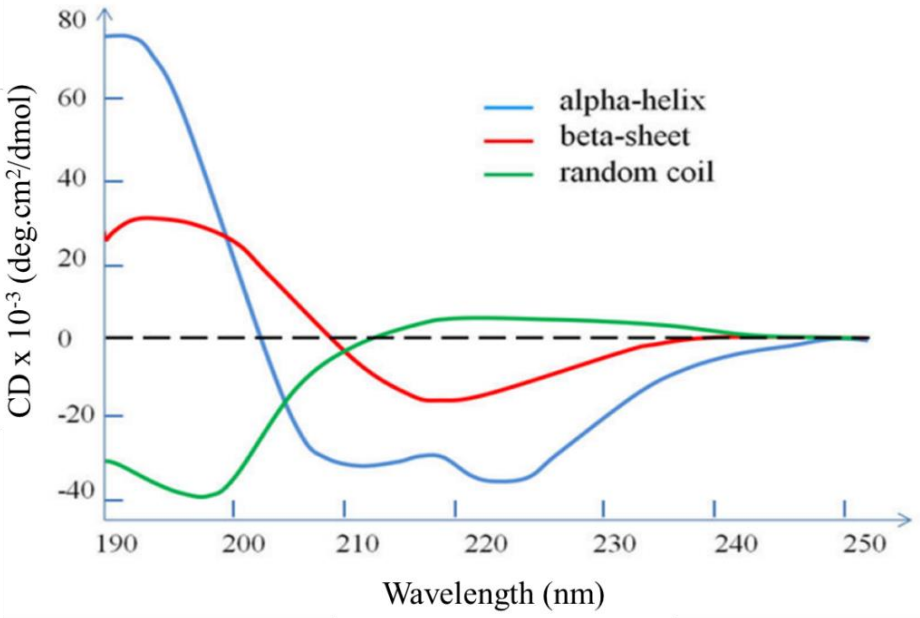

Figure 3.3: Spectral properties of the secondary structural content of proteins using circular dichroism

The blue spectrum represents the α-helical structure with a positive peak at 190 nm and negative peaks at 222 nm and 208 nm. The red spectrum represents the β-sheet secondary structure with a positive peak at 195 nm-200 nm and a negative peak between 210 nm-220 nm. The green spectrum represents a random coil structure with a negative peak ~200 nm (Wei *et al*., 2014).

structural features. The results of this experiment were expressed in molar ellipticity which was derived using the following equation:

$$[\theta] = \frac{100 \times \theta}{Cnl} \tag{11}$$

where θ represents ellipticity (millidegree), *C* represents protein concentration (mM), *n* represents the number of residues in protein and *l* represents path length (cm)

The data was further submitted onto the Dichroweb Online Circular Dichroism Tool which was used to further evaluate *Kp*NNAT secondary structure (Whitmore and Wallace, 2004). The Contin-LL (Provencher & Glockner Method) was used and the data had been fitted against an algorithm. The data retrieved from Dichroweb is presented as secondary structural percentages of *Kp*NNAT residues.

3.2.7.2 Intrinsic tryptophan fluorescence

Intrinsic tryptophan fluorescence spectroscopy involves fluorescence spectroscopy, a commonly used technique for protein characterisation. The underlying principle of fluorescence spectroscopy involves the excitation of a sample which causes an emission of light of lower energy corresponding to a longer wavelength to produce an emission spectrum (Shahzad *et al.*, 2009). Thus, based on this principle, changes due to protein folding, environment (hydrophilic or hydrophobic) or binding may lead to changes in fluorescence which are used as a structural analysis tool.

Tryptophan (Trp) is a dominant source for intrinsic fluorescence due to its indole ring. This amino acid has an emission wavelength at ~350 nm when excited at 295 nm. Compared to other aromatic amino acids such as phenylalanine or tyrosine, Trp fluorescence exhibits a higher quantum yield and less quenching due to the reactivity of its unique indole group (Ghisaidoobe and Chung, 2014). In addition, the indole ring of Trp is highly sensitive to its local microenvironment with regards to polarity, hydrogen bonding and non-covalent interactions thus influencing its emission spectrum (Ghisaidoobe and Chung, 2014). Thus, changes in the emission spectrum of tryptophan can reveal changes in the microenvironment of the protein tertiary structure.

Determination of the microenvironment of *Kp*NNAT was performed by using tryptophan fluorescence studies. The Jasco FP-6300 spectrofluorometer (Analytical Solutions) was used with a scanning speed of 100 nm/min, data pitch of 0.5 and bandwidth of 2.5 nm. An analysis was performed on native (5 µM *Kp*NNAT) and denatured (5 µM *Kp*NNAT with 8 M urea) samples in filtered phosphate buffer (5 mM sodium phosphate monobasic, pH 7.4) at approximately 20 °C. Blank samples were used and subtracted where appropriate: native blank (filtered phosphate buffer), denatured blank (8 M urea in filtered phosphate buffer). Excitation occurred at 295 nm and emission was observed between 300 nm-500 nm. Furthermore, to emphasise the conservation of Trp residues, Clustal Omega (online alignment tool) was used to align the amino acid sequences of *Kp*NNAT and *Ec*NNAT (see Figure 2.10). Trp residues are highly conserved within bacterial NNATs and thus exhibit crucial roles in NNAT activity.

3.2.7.3 Extrinsic ANS fluorescence spectroscopy

Another common method for tertiary structure analysis is the use of fluorescent dyes. ANS, a popular fluorescent dye, is used for the analysis of surface hydrophobicity, unfolding/folding, aggregation and conformational studies of proteins. The dye is excited at ~395 nm and exhibits an emission wavelength at ~500 nm-505 nm (Hawe *et al*., 2008). This anionic dye binds to positively charged amino acids and prefers non-polar environments. The emission wavelength and ANS quantum yield is dependent on the polarity, viscosity and temperature of the microenvironment. It binds non-covalently to proteins and exhibits a low fluorescence or quantum yield in polar environments (Hawe *et al*., 2008). Shifts in ANS maximum emission wavelengths may reveal changes in tertiary structure with regards to folding and unfolding events. In addition, the displacement of ANS upon the binding of substrates or ligands provides insight into ligand binding. The structure of ANS is shown in Figure 3.3.

Analysis of the hydrophobicity of *Kp*NNAT was accomplished by performing ANS fluorescence using the Jasco FP-6300 spectrofluorometer (Analytical Solutions). The analysis was performed on native (5 µM *Kp*NNAT, 35 µM ANS), denatured (5 µM *Kp*NNAT with 8 M urea, 35 µM ANS), native-NAD^+ (5 µM *Kp*NNAT, 35 µM ANS with 1 mM NAD^+) and native-ATP (5 µM *Kp*NNAT, 35 µM ANS with 1 mM ATP) samples in filtered phosphate buffer (5 mM sodium phosphate monobasic, pH 7.4) at approximately 20 °C. Blank samples were prepared in the same way as native, denatured, ATP and NAD^+ samples in the absence of *Kp*NNAT. Excitation occurred at 395 nm and emission was observed between 400 nm-600 nm

respectively. The experiment was performed using a scanning speed of 100 nm/min, data pitch of 0.1 and bandwidth of 5 nm.

3.2.7.4 Mant-ATP fluorescence

The binding of methylanthraniloyl-ATP (mant-ATP) to an enzyme may reveal information regarding enzyme binding sites. Mant-ATP contains a fluorescent probe that emits fluorescence at ~440 nm when excited at ~355 nm. Thus, changes in tertiary structure alter the fluorescence intensity of mant-ATP (Patel *et al*., 2014). The fluorescent probe is highly sensitive to environmental conditions such as polarity. In non-polar environments, the fluorescent quantum yield is significantly higher than in a polar environment. Since the enzyme of focus in this study requires ATP as a substrate, the use of mant-ATP can be used the mimic the binding of ATP to its binding site. Furthermore, the displacement of mant-ATP in the presence or absence of certain substrates may contribute to the analysis of substrate binding. Thus, changes in mant-ATP fluorescence may provide insight into enzyme tertiary structure, polarity and substrate binding (Leskovar and Reinstein, 2008). The structure of mant-ATP is shown in Figure 3.4.

Further analysis of ligand binding was accomplished by performing mant-ATP fluorescence. The experiment involved several samples. All samples (excluding blanks) contained 5 μM *Kp*NNAT and 10 μM mant-ATP. The following samples (with corresponding blanks) were prepared: native, denatured (8 M urea), native with 2 mM ATP, native with 2 mM NAD^+. All samples were prepared in filtered phosphate buffer (5 mM sodium phosphate monobasic, pH 7.4) with 5 mM $MgCl_2$ at approximately 20 °C. Blank samples were prepared in the same manner as the native, denatured, ATP and NAD^+ samples in the absence of *Kp*NNAT. Data was corrected using the blanks. Excitation occurred at 355 nm and emission was observed between 400 nm-600 nm respectively using the Jasco FP-6300 spectrofluorometer (Analytical Solutions). The scanning speed was 100 nm/min, data pitch of 0.5 and bandwidth of 5 nm.

3.2.8 Thermodynamic studies

3.2.8.1 Isothermal titration calorimetry

Binding events associated with ligands and substrates produce changes in thermodynamic parameters of various complexes. ITC is a well-known technique used to identify changes in thermodynamic parameters of protein-protein interactions. This technique is based on the

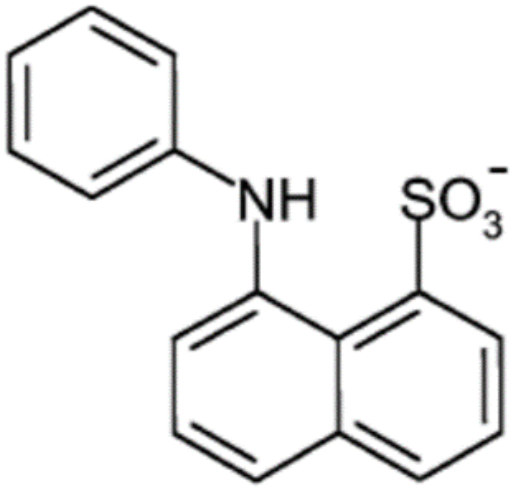

Figure 3.4: Structure of 1-anilinonapthalene-8-sulfonate (ANS)
The structure of ANS shows the naphthalene ring and the sulfonate group. The naphthalene ring is sensitive to the polarity of the environment (Singh *et al*., 2019).

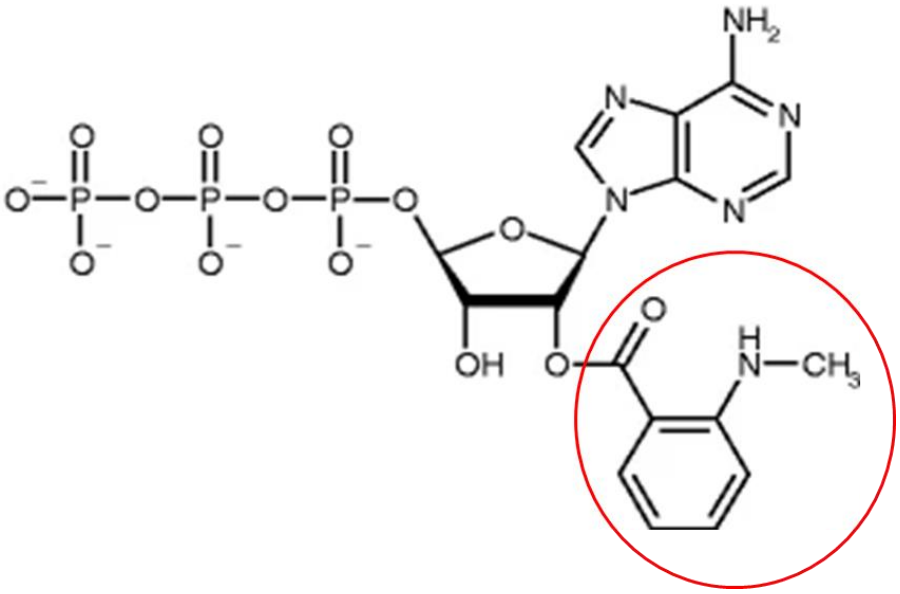

Figure 3.5: Structure of methylanthraniloyl-ATP (mant-ATP)
The structure of mant-ATP is shown in this figure. The red circled area indicates the mant fluorophore (Szulc *et al*., 2013).

principle of measuring the heat released or absorbed upon the binding of two molecules, thus revealing information about the binding equilibrium (Pierce *et al*., 1999). Thermodynamic parameters such as binding constants (K_a), stoichiometry (n) and binding enthalpy (ΔHb) can be derived from this experiment. Other parameters such as the change in Gibbs free energy (ΔG), change in entropy (ΔS) and change in heat capacity binding (ΔCp) can be calculated using the information derived from an ITC experiment (Pierce *et al*., 1999). ITC involves the injection of a sample to determine if heat is taken up or released depending on whether the reaction is exothermic or endothermic (Pierce *et al*., 1999). The ITC instrument is set up using two cells, a reference and sample cell. Constant power is supplied to the reference cell which allows heat maintenance within the cells (Pierce *et al*., 1999). Upon ligand-macromolecule interaction in the sample cell, heat is either absorbed or released and the power needed to maintain a constant temperature will either increase or decrease (Pierce *et al*., 1999). The heat supplied to the sample cell with every ligand injection is an observable signal associated with the binding event (Pierce *et al*., 1999). The ITC set up, raw data and direct measure of thermodynamic parameters are shown in Figure 3.5.

ITC experiments were performed using the Nano-ITC instrument (TA instruments). The instrument was cleaned and equilibrated before each run. All samples were prepared in a PBS (137 mM NaCl, 2.7 mM KCl, 10 mM Na_2HPO_4, 2 mM KH_2PO_4, pH 7.4) buffer with 5 mM $MgCl_2$ and 1 mM TCEP. ATP (5 mM) in a PBS buffer dialysate at pH 7.4 was prepared and used. Dialysis of *Kp*NNAT was done in a PBS buffer overnight at 4 °C before performing each experiment. For each titration (excluding blanks), ~40 μM *Kp*NNAT was used. Blank samples involved the injection of ligands (5 mM ATP) in PBS buffer, pH 7.4. The conditions for the experiments were as follows: 310 rpm stirring rate, 250 μL syringe volume, 1.5 mL sample cell volume, 5 μL injection volume and a data interval of 2 at 25 °C. The data was analysed using NanoAnalyze software. After each data set was treated accordingly with the blank data, the following parameters were derived from the software analysis: dissociation constant (K_d), change in standard enthalpy ($\Delta H°$) and stoichiometry (n). The following equations were then used to derive the outstanding thermodynamic parameters:

$$\Delta G° = RT \ln(1/K_d) \quad (12)$$

$$\Delta G° = \Delta H° - T\Delta S° \quad (13)$$

where R is 8.314 J/mol/K, T is the absolute temperature in Kelvin and K_d is the inverse of K_a.

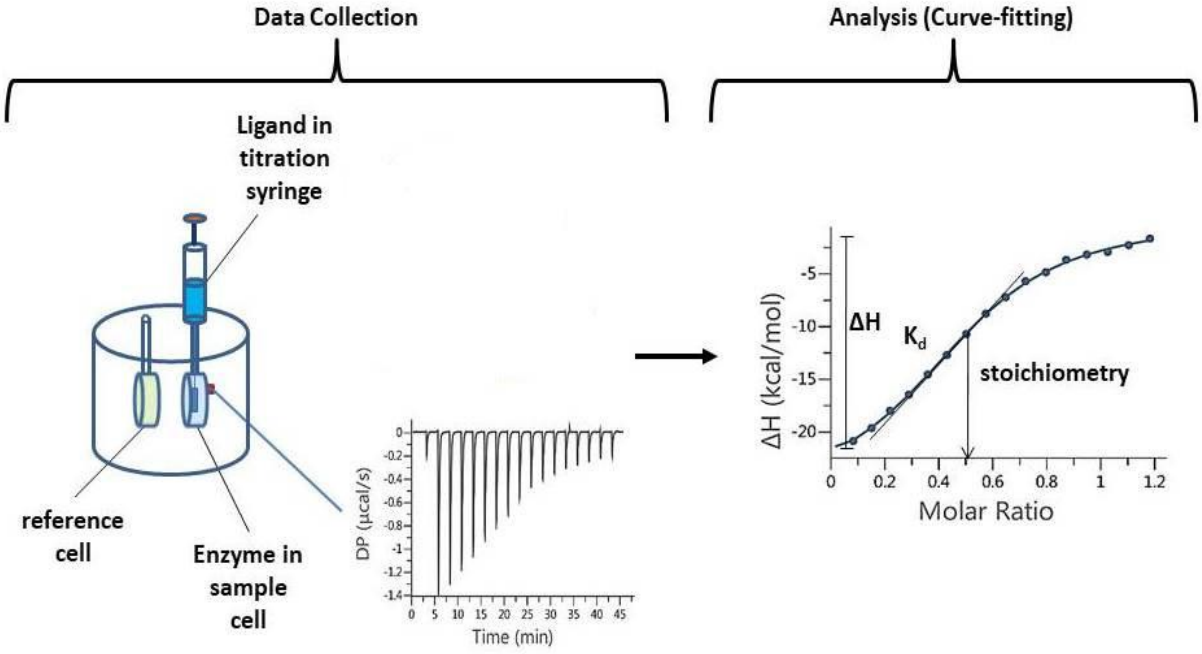

Figure 3.6: ITC data collection and curve fitting

ITC data collection demonstrates the ITC set up with the reference cell and the sample cell (macromolecule, enzyme). The ligand is in the syringe and will be injected into the sample cell upon injection. The raw data attained from the experiment is shown with negative peaks. The data is then analysed using curve fitting demonstrating the change in enthalpy against molar ratio. Thermodynamic parameters such as $\Delta H°$, K_d and stoichiometry (n) are derived directly from the curve as indicated (Gunnell, 2019).

CHAPTER 4:

RESULTS

4.1 Recombinant expression of *Kp*NNAT

*Kp*NNAT was recombinantly expressed at 20 °C overnight using a pGEX-4T-1 vector at which encoded for the expressed enzyme attached to a GST and hexahistidine tag with an overall molecular weight of ~52 kDa. Varying IPTG inductions were performed to investigate the effect on the expression of *Kp*NNAT. SDS-PAGE was used to analyse the efficiency of *Kp*NNAT expression and purification based on the migration of proteins on their respective molecular weights (Moosavi-Movahedi, 2005). From Figure 4.1, IPTG inductions between the range of 0.25 mM and 1 mM resulted in a similar expression of *Kp*NNAT in the soluble fraction. However, without the addition of IPTG, *Kp*NNAT was unable to be overexpressed as indicated by the small band at ~52 kDa (supernatant, 0 mM) in comparison to the induced cultures. A larger fraction of *Kp*NNAT was observed in the supernatant samples in comparison with the pellet samples. Thus, the GST-hexahistidine-tagged *Kp*NNAT was successfully overexpressed in the soluble fraction using a pGEX-4T-1 vector encoding for a GST tag on the N-terminus which was confirmed by the large bands at ~52 kDa.

4.2 Purification and cleavage of *Kp*NNAT

Due to the presence of both GST and hexahistidine tags, a double purification of *Kp*NNAT could be achieved. *Kp*NNAT was first subjected to a GSH-Agarose column to trap the protein via its GST tag. Figure 4.2A shows the various washes performed to investigate the binding efficiency of *Kp*NNAT to the column in the presence of a detergent such as Tween-20-PBS. The binding of *Kp*NNAT to the GSH-Agarose column was efficient since the protein was not present in any subsequent washes (no bands evident). The uncleaved *Kp*NNAT was eluted to confirm the purity of the samples prior to subjecting the protein to further cleavage and purification. The eluted fractions were controlled as indicated by the peak elutions (elutions 2, 3 and 4). The presence of impurities was evident in the concentrated samples (elution 2, 3 and 4). Thrombin cleavage was optimised by performing a time trial to investigate the effective thrombin cleavage time interval as shown in Figure 4.2B. Within 5 min, thrombin cleavage had occurred however, a slight band of uncleaved *Kp*NNAT was evident in all samples. Overnight (16 hrs) cleavage resulted in the smallest band of uncleaved *Kp*NNAT, thus, overnight cleavage was used for subsequent purifications. Simultaneous primary purification and cleavage

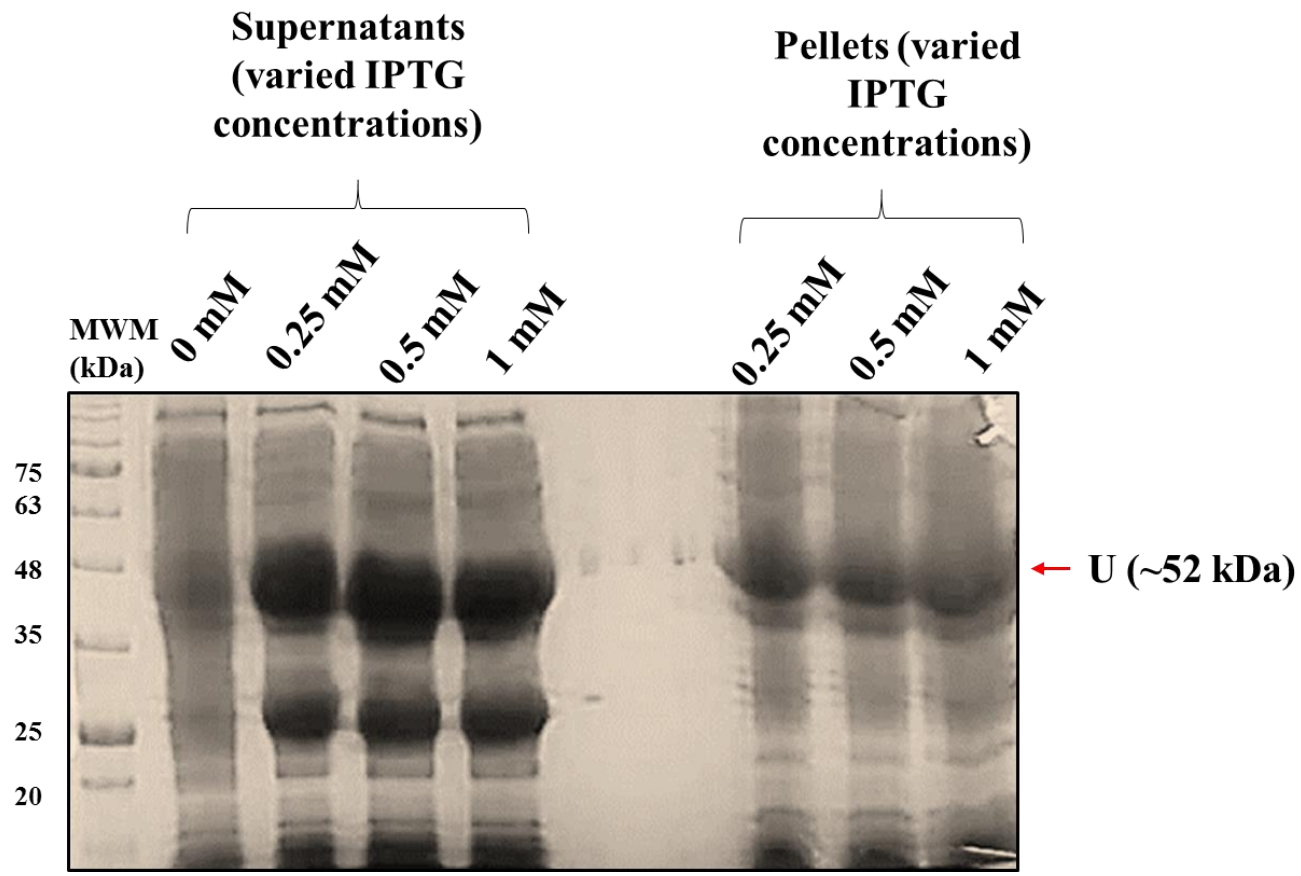

Figure 4.1: SDS-PAGE analysis of the expression trials of *Kp*NNAT

The resulting gel represents the expression trials of *Kp*NNAT at 20 °C overnight using a pGEX-4T-1 vector. The supernatants and pellets are shown with their corresponding IPTG inductions. The addition of IPTG in the range of 0.25 mM to 1 mM produced a vast increase in *Kp*NNAT production. U represents uncleaved *Kp*NNAT which was successfully expressed in the soluble form due to the thick bands with a molecular weight of ~52 kDa in the supernatants. The pellets samples also contained a fraction of *Kp*NNAT which was less prominent than in the supernatant. The standard curve for this gel can be found in the Supplementary information.

occurred via on-column cleavage within the GSH-Agarose column overnight. These contents were then passed through the Ni^{2+}-IMAC, the final step of *Kp*NNAT purification. *Kp*NNAT had bound to the Ni^{2+}-IMAC column via the hexahistidine tag and was eluted using imidazole. Elution of *Kp*NNAT was controlled as shown in Figure 4.2C (peak elution 3). Successful cleavage and purification of *Kp*NNAT was confirmed due to the presence of cleaved *Kp*NNAT (with hexahistidine tag) at ~25 kDa which was confirmed by the standard curve (see Supplementary figure 1). There was a slight presence of impurities which is only evident in the concentrated samples (elution 2 and 3). Figure 4.2D shows the elution of GSH-Agarose after thrombin cleavage and IMAC elution, thus, GST was eluted which is shown by the single band at ~26 kDa. The overall double purification and on-column cleavage resulted in a pure and mostly cleaved *Kp*NNAT. The purity and homogeneity were further analysed using absorbance spectroscopy (Figure 4.3) which showed a distinct peak at 280 nm indicative of protein and no peaks or interference at 340 nm indicating that the purified and cleaved protein showed no sign of aggregation. The concentration of the homogenous and cleaved *Kp*NNAT IMAC elution 3 sample was 13.85 mg/mL (Figure 4.4).

4.3 *Kp*NNAT concentration determination

Quantifying the enzyme *Kp*NNAT was achieved using absorbance spectroscopy at both 280 nm (protein detection) and 340 nm (protein aggregation). From the readings, a linear regression line was fitted to produce a linear equation with a gradient. Utilising the Beer-Lambert law (equation 1), the gradient derived from the line equation and the *Kp*NNAT (Uniprot ID: B5XZR5) extinction coefficient (38055 M/cm) derived from ProtParam (Gasteiger *et al*., 2005), the concentration of IMAC elution 3 was calculated to be 13.85 mg/mL or 0.55 mM of *Kp*NNAT (Figure 4.4).

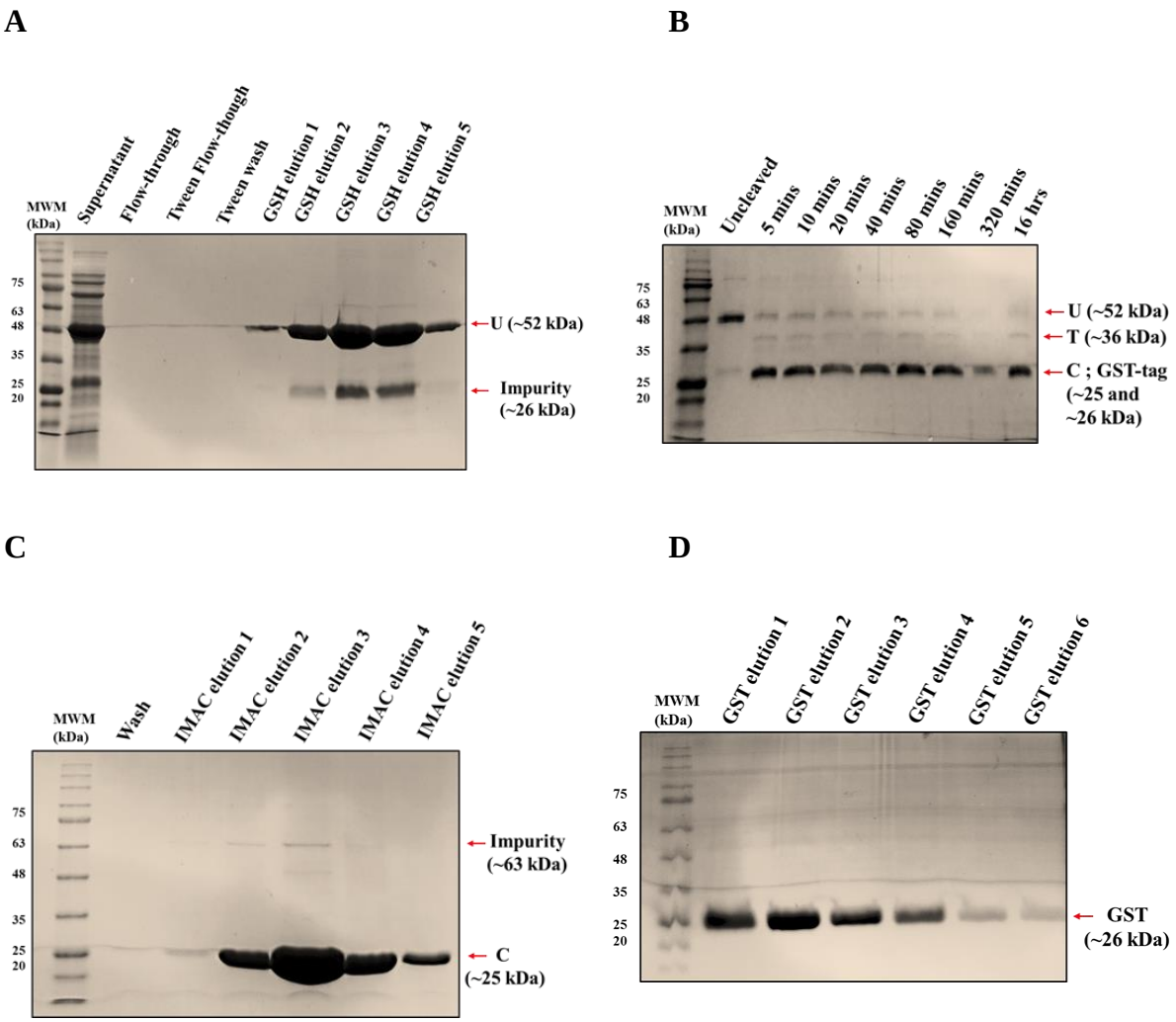

Figure 4.2: SDS-PAGE analysis of *Kp*NNAT purification and cleavage

All analysis was done using 12.5% glycine SDS-PAGE gels. U represents uncleaved *Kp*NNAT, C represents cleaved *Kp*NNAT and T represents thrombin. Figure A represents the first purification step using GSH-Agarose chromatography. The supernatant lane indicates the presence of *Kp*NNAT (~52 kDa) among other impurities. Several washes indicate the high binding efficiency of *Kp*NNAT to the column due to the absence of the *Kp*NNAT band. The elutions from the column using 5 mM reduced GSH (in PBS buffer, pH 7.4) demonstrate the controlled uncleaved *Kp*NNAT elution (~52 kDa) with some impurities. Figure B shows thrombin cleavage trials for effective thrombin cleavage. Cleavage occurs swiftly but results in a fraction of uncleaved protein. Overnight (16 hrs) cleavage demonstrated the slightest amount of uncleaved protein. Figure C shows the final step of purification performed using Ni^{2+}-IMAC. The elution (500 mM imidazole in PBS buffer, pH 7.4) of cleaved *Kp*NNAT was controlled as shown by the peak elution (elution 3). The cleaved *Kp*NNAT was successfully purified. A slight fraction of impurities is observed within concentrated samples. Figure D shows the elution (5 mM GSH in PBS buffer, pH 7.4) of GSH-Agarose column after thrombin cleavage and IMAC elution. GST was eluted as indicated by the bands at ~26 kDa. The standard curves for the gels can be found in the Supplementary information.

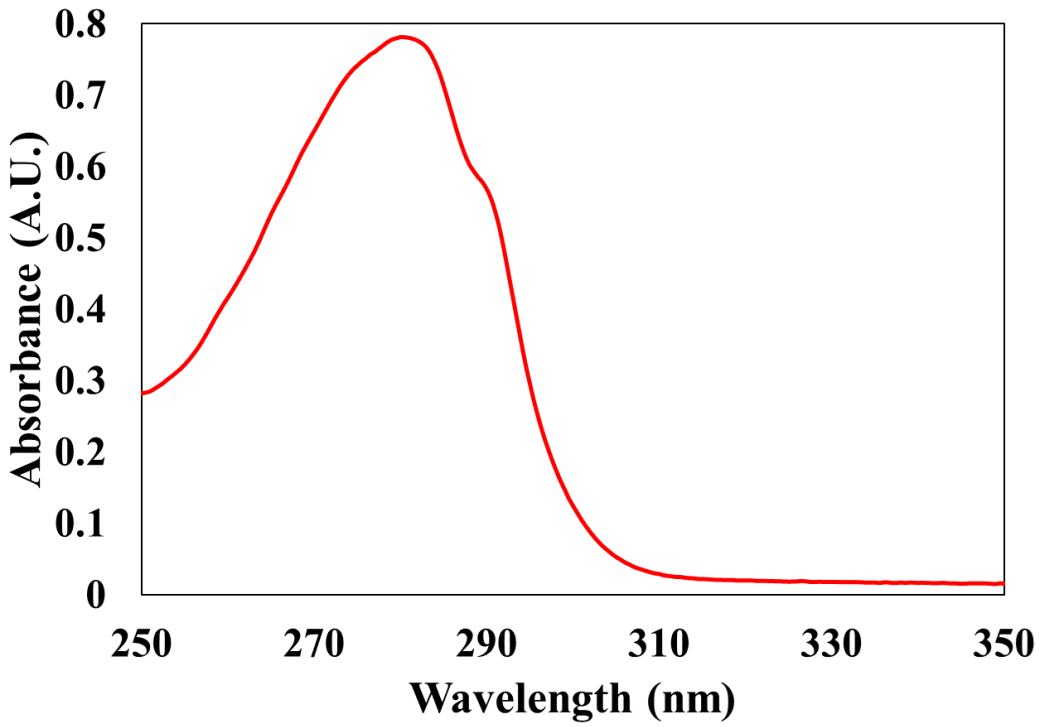

Figure 4.3: Absorbance spectrum of purified *Kp*NNAT

The absorbance spectrum of *Kp*NNAT shows a distinct peak at 280 nm indicating the presence of protein. The data shows no nucleic acid contamination at 260 nm and no aggregation of protein at 340 nm.

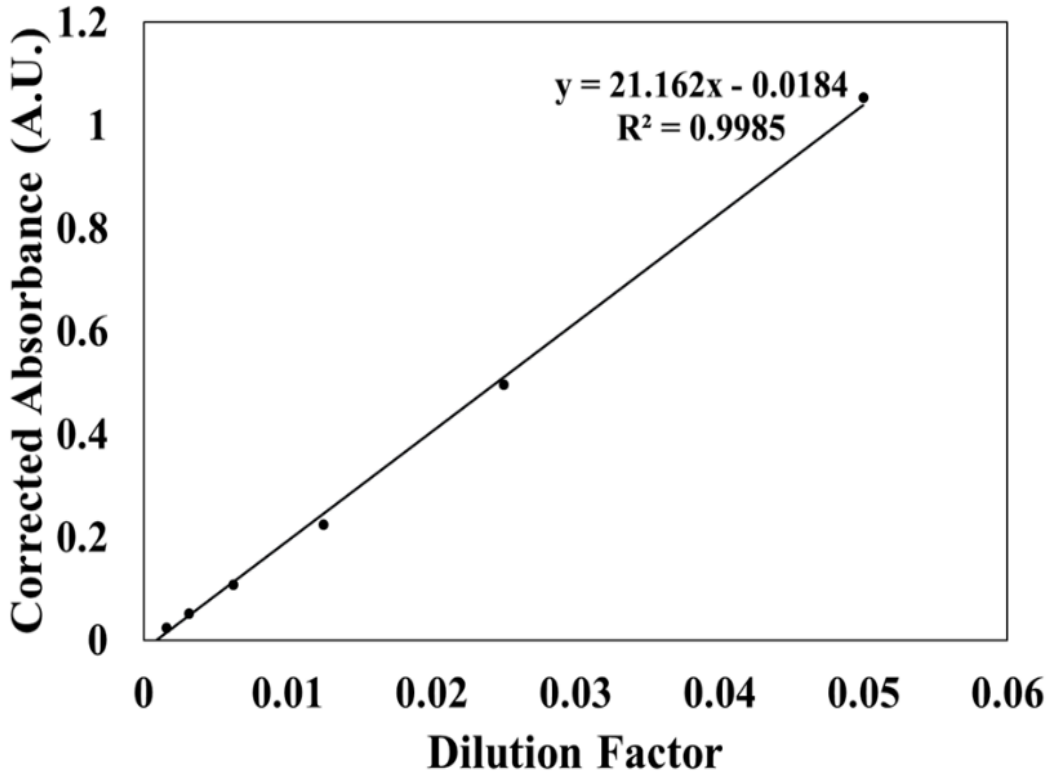

Figure 4.4: Quantification of purified *Kp*NNAT

The linear regression presents the line of best fit for the scatter plot of corrected absorbance against the dilution factor. The trendline equation displays a gradient of 21.162 and R^2 value of 0.99. The Beer-Lambert law and trendline gradient produced a concentration of 13.85 mg/mL of *Kp*NNAT in PBS buffer (137 mM NaCl, 2.7 mM KCl, 10 mM Na_2HPO_4, 2 mM KH_2PO_4, pH 7.4) which is represented by IMAC elution 3. The calculation associated with this figure is shown in the Supplementary information.

4.4 *Kp*NNAT activity assay

To investigate the optimal pH range for the *Kp*NNAT dual enzyme assay, a pH-dependent activity assay was performed. The assay was conducted through numerous buffers with varied pH ranges. From the experiment, the optimal pH range for the dual assay was deduced to be pH 9 (Figure 4.5). Since the activity assay is based on dual enzymes, the pH level effect on the assay cannot be contributed to a single enzyme. Noteworthy, the optimal pH range for the second enzyme of the reaction, ADH, is pH level 9 resulting in optimal NADH production which is detected at 340 nm. Thereafter, the assay was repeated at two different pH levels (pH 7.5 and pH 9) with varied *Kp*NNAT concentrations which produced pseudo-specific activities of these assays. Pseudo-specific activity is a specific activity that does not specifically represent the rate of catalysation of one enzyme during a dual enzyme reaction. The specific activity was obtained and verified that *Kp*NNAT was an active enzyme at different pH levels. Specific activity was derived using the gradient from the linear equation of the trendline. A higher specific activity of 0.2408 μmol/min/mg was achieved at pH level 9 (Figure 4.6B) rather than a specific activity of 0.0143 μmol/min/mg at pH 7.5 (Figure 4.6A).The pseudo-specific activity of the dual enzyme assay resulted in a 20-fold increase at pH level 9. Since ADH exhibits optimal functioning at pH level 9, the pseudo-specific activity could be influenced by ADH functionality during this assay.

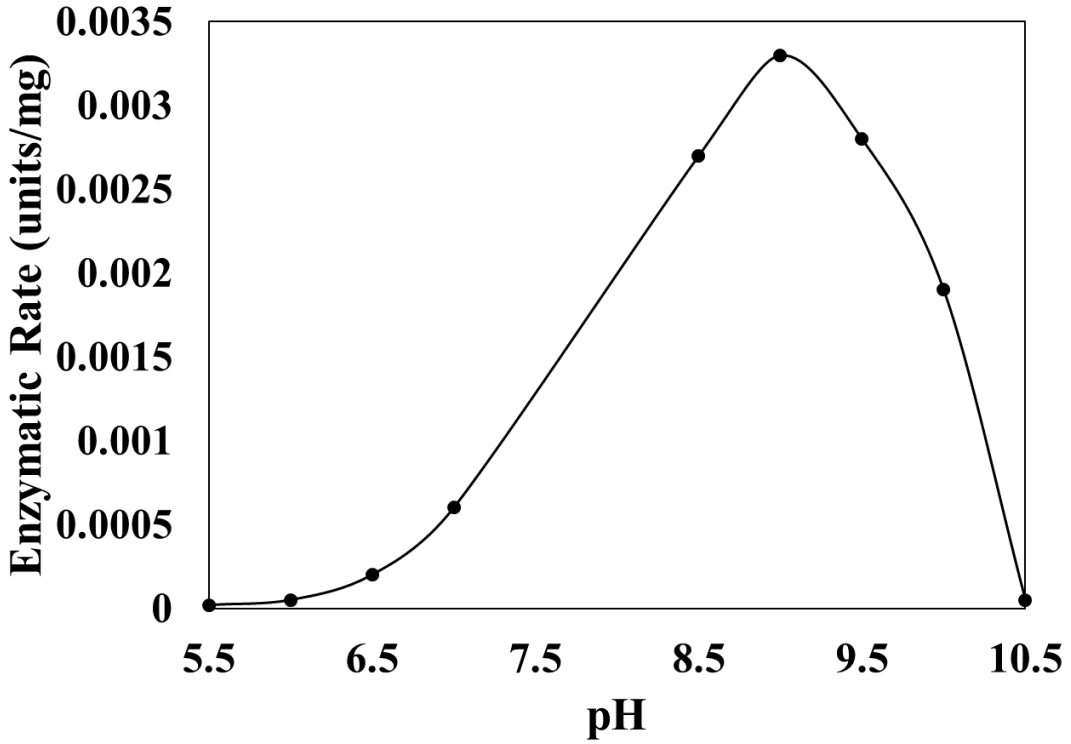

Figure 4.5: pH-dependent activity assay of *Kp*NNAT

Dual activity assay of *Kp*NNAT under varied pH conditions from pH level 5.5 to pH level 10.5. The optimal pH condition for the dual *Kp*NNAT activity assay is pH level 9.0 as shown by the above plot which exhibits a bell curve with its peak at pH level 9.0. *Kp*NNAT concentration of 800 nM was used with 10 units/mL ADH, analytical grade ethanol (1%), 5 mM $MgCl_2$, 1 mM ATP and 0.5 mM NMN in the appropriate buffer.

A

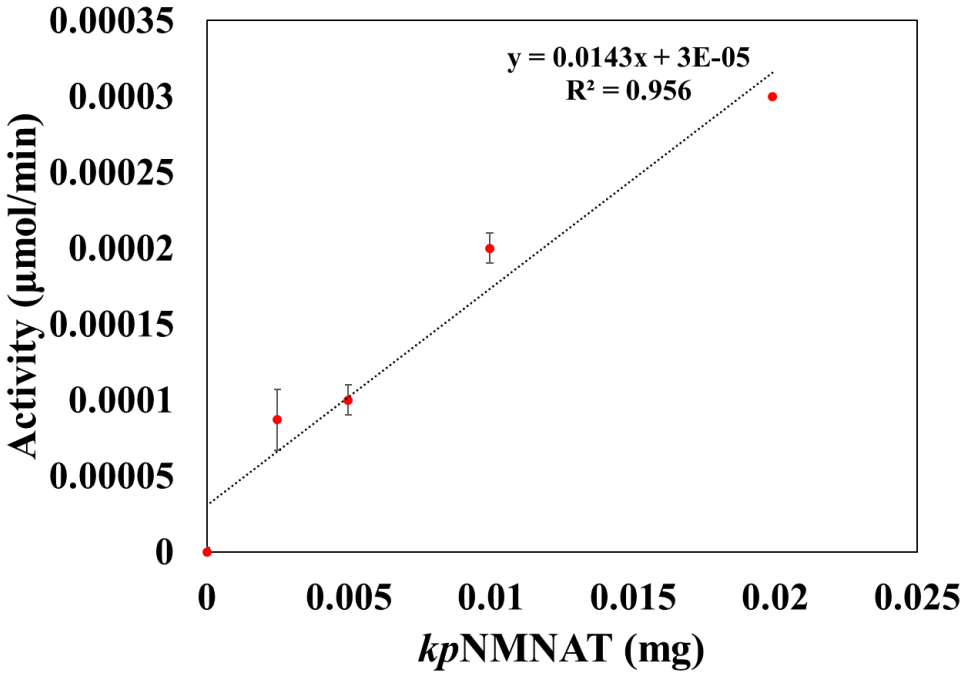

B

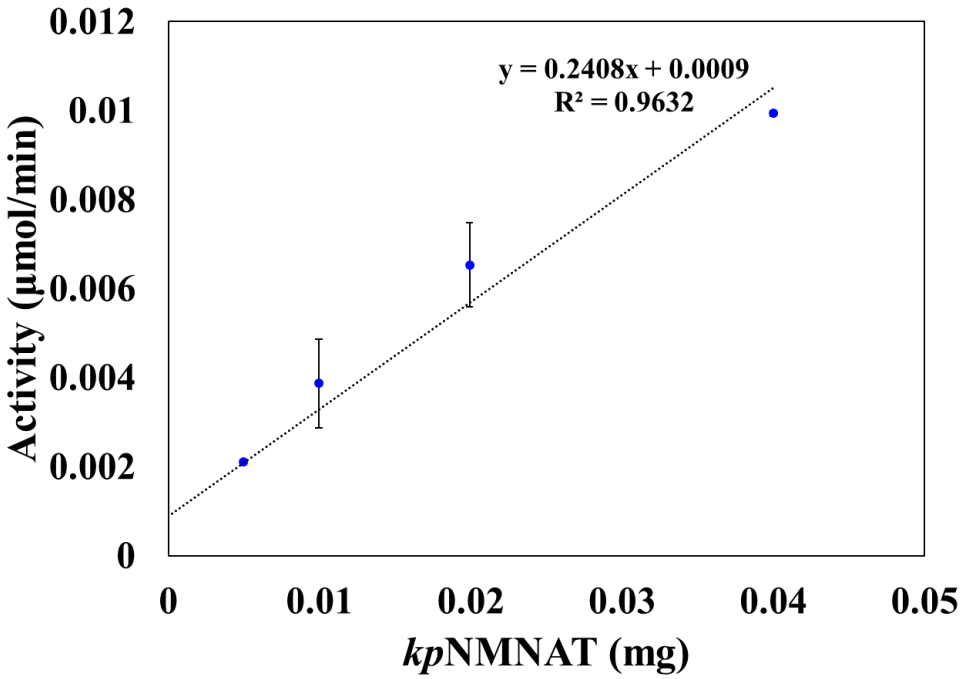

Figure 4.6: *Kp*NNAT dual activity assay

The effect of pH levels on a dual enzyme assay at 340 nm is depicted in the above figures. *Kp*NNAT dual assay at pH level 7.5 (PBS buffer) (•) produced a specific activity of 0.0143 µmol/min/mg. *Kp*NNAT dual assay at pH level 9.0 (Tris-HCl buffer) (•) produced a specific activity of 0.2408 µmol/min/mg. At pH level 9, higher specific activity was achieved under the same conditions. The assay was done in triplicates and standard error bars are shown.

4.5 Spectral Studies

4.5.1 Far-UV circular dichroism

Investigating secondary structural characteristics was performed using far-UV CD. Based on the ability to polarise light, the peptide bonds of *Kp*NNAT served as a chromophore in the far-UV region. The analysis revealed a dominant α-helical secondary structure indicated by the distinct peak at 190 nm (Figure 4.7). The data is confirmed through the predicted model. In its unfolded state, *Kp*NNAT exhibited a loss of secondary structural features due to unfolding. The Dichroweb analysis tool produced an NRMSD (normalized root mean square deviation) value of 0.1 which is slightly higher than normal (0.05) (Table 4.1). This value represents a "goodness-of-fit" for the submitted data (Whitmore and Wallace, 2004). If the value is higher than 0.1, the calculated secondary structure fitted against the actual structure is unlikely to be accurate (Whitmore and Wallace, 2004). Since the data convoluted by Dichroweb (Whitmore and Wallace, 2004) exhibited an NRMSD value within the range of 0.1, it can be used as a reference to the *Kp*NNAT secondary structure.

4.5.2 Intrinsic tryptophan fluorescence spectroscopy

To evaluate the microenvironment of *Kp*NNAT under specific conditions, intrinsic tryptophan fluorescence was performed. Due to its unique indole ring, tryptophan is excited at 295 nm and emits light at 350 nm, subject to change due to polarity. Native *Kp*NNAT emission showed a high tryptophan fluorescent intensity (~50 arbitrary units) at 350 nm (Figure 4.8). Denatured *Kp*NNAT exhibited a lower intensity (~30 arbitrary units) at the same wavelength. During unfolding, the polarity of the environment influenced tryptophan residues. From the data, it can be deduced that the tryptophan residues are mostly buried. The unfolding of *Kp*NNAT exposes these buried tryptophan residues to the polar environment.

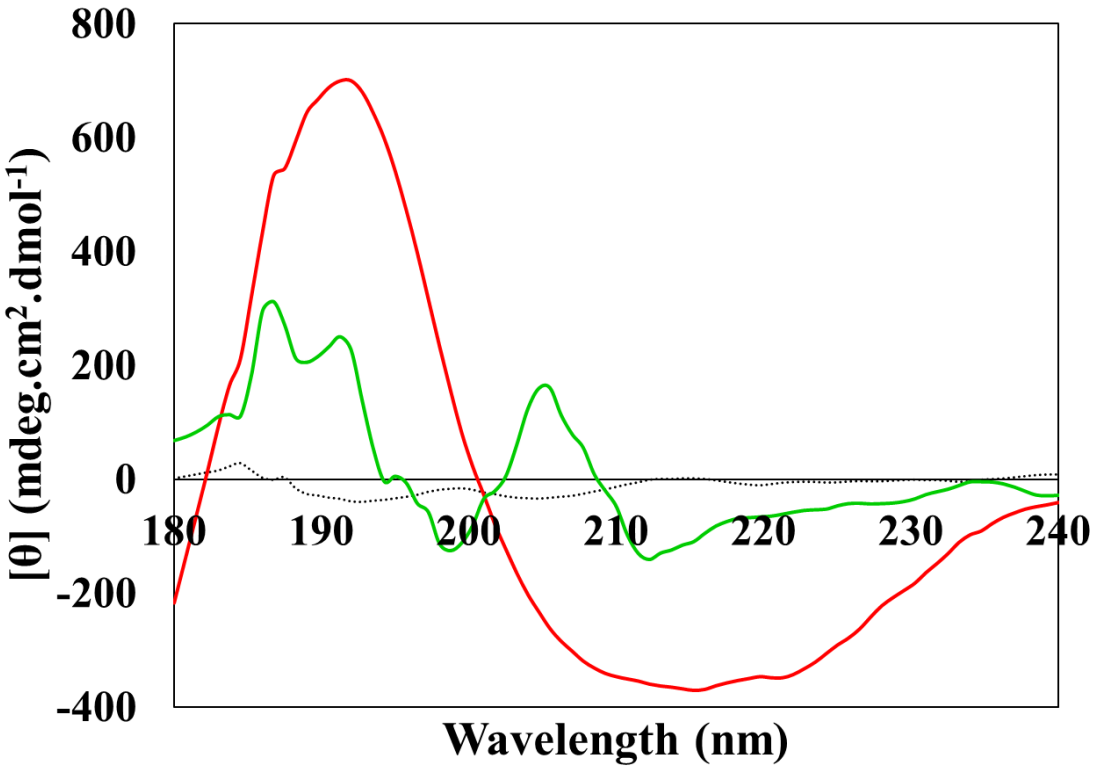

Figure 4.7: Far-UV circular dichroism spectra of *Kp*NNAT
Native *Kp*NNAT (5 µM) (—) in 5 mM phosphate buffer (pH 7.4) exhibits a dominant α-helical secondary structure with a distinct peak at 190 nm. Denatured *Kp*NNAT (5 µM) (—) in 5 mM phosphate buffer (pH 7.4) with 8 M urea, shows unfolding of the enzyme and loss of secondary structural features. The dotted line indicates the blank data set.

Table 4.1: Dichroweb Analysis of the native *Kp*NNAT secondary structure
NRMSD: 0.1

	Helix	Strand	Turns	Unordered	Total
***Kp*NNAT**	38	16	20	26	100

*All data is represented as percentages

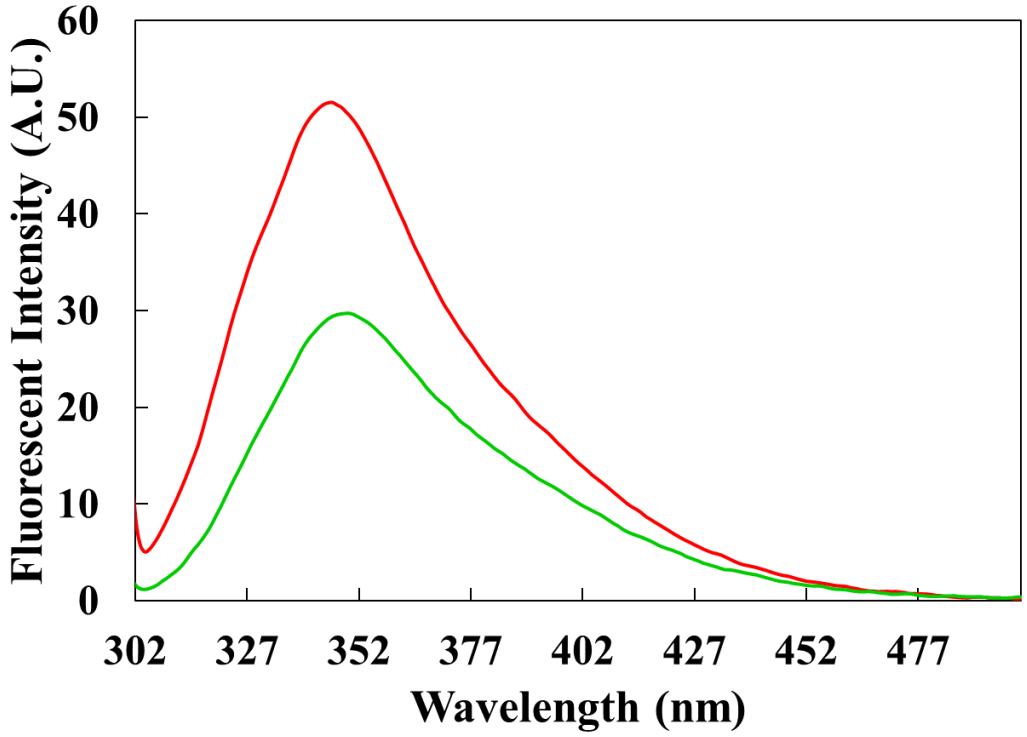

Figure 4.8: Intrinsic tryptophan fluorescence spectra of *Kp*NNAT
Native *Kp*NNAT (5 µM) (—) in phosphate buffer (5 mM sodium phosphate monobasic, pH 7.4) exhibited a high tryptophan fluorescent intensity upon emission at 350 nm. Denatured *Kp*NNAT (5 µM) (—) in phosphate buffer (5 mM sodium phosphate monobasic, pH 7.4) with 8 M urea exhibited a low tryptophan fluorescent intensity upon emission at 350 nm. Unfolding of *Kp*NNAT influences the polarity of the environment.

4.5.3 Extrinsic ANS fluorescence spectroscopy

To further investigate the hydrophobicity of *Kp*NNAT, ANS, an anionic dye was used. Due to its spectral features, ANS emission can be observed at 500 nm once excited at 395 nm. Shifts in the ANS maximum emission spectra revealed fluctuations in the protein tertiary structure. In the presence of NAD^+ and ATP, the ANS fluorescent intensity was significantly high compared to unbound *Kp*NNAT with bound ANS (Figure 4.9). Upon ATP binding in the presence of ANS, the fluorescent intensity increased by 2.3-fold. Upon NAD^+ binding in the presence of ANS, the fluorescent intensity increased by 2-fold. The binding of *Kp*NNAT substrates and products causes conformational changes in the tertiary structure of *Kp*NNAT. These ANS displacement studies provide insight into the possible binding events associated with *Kp*NNAT.

4.5.4 Mant-ATP fluorescence spectroscopy

Further insights into *Kp*NNAT binding events was achieved by performing mant-ATP fluorescence. Mant-ATP is an ATP molecule with an additional fluorescent probe which emits light at 445 nm when excited at 355 nm. Mant-ATP binds to ATP binding sites. Fluorescent signalling indicates the binding of mant-ATP. Free *Kp*NNAT (unbound) generated the highest mant-ATP fluorescent intensity whereas the presence of ATP or NAD^+ resulted in a low intensity and emission shift to a longer wavelength (Figure 4.10). The binding of NAD^+ exhibited the lowest mant-ATP fluorescent intensity (decreased intensity by 1.7-fold). Data from this experiment reveal information regarding the occupancy of *Kp*NNAT binding sites. The displacement of mant-ATP upon NAD^+ binding indicates a possible competitive nature between ATP and NAD^+ for the ATP binding site.

A

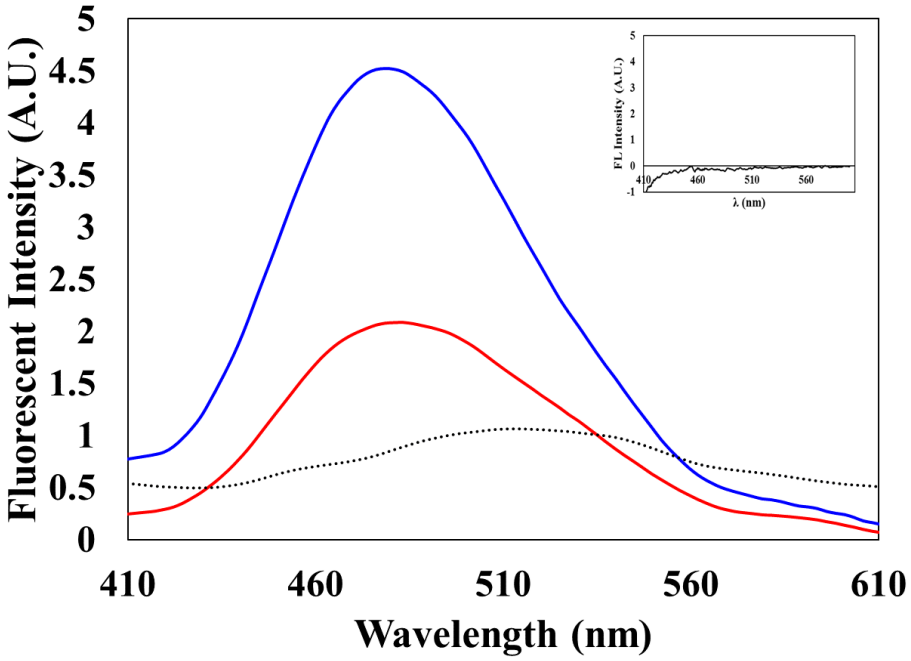

B

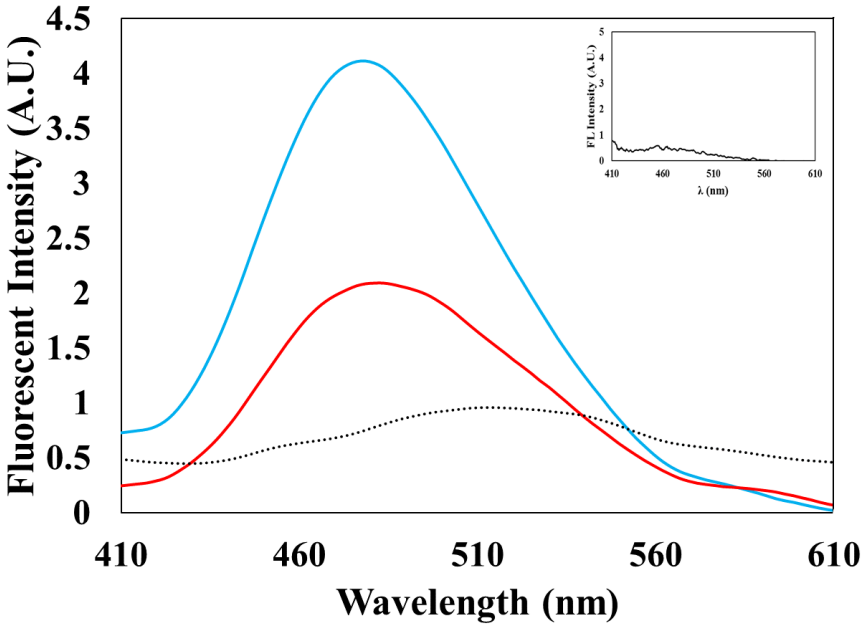

Figure 4.9: Extrinsic ANS fluorescence spectra of *Kp*NNAT in the presence of various substrates and ligands

The above spectra represent ANS:*Kp*NNAT (—), ANS:*Kp*NNAT in the presence of ATP (—), ANS:*Kp*NNAT in the presence of NAD^+ (—) and free ANS in buffer (·····). All samples were prepared in 5 mM sodium phosphate monobasic (pH 7.4), 35 µM ANS, 5 µM *Kp*NNAT, 1 mM ligands. The presence of substrate, ATP, and product, NAD^+, produces a high ANS fluorescent intensity upon binding to *Kp*NNAT. The binding of NAD^+ or ATP causes conformational changes of *Kp*NNAT that may alter the polarity of pockets. The dotted spectrum was used to correct the data. The inner filter effect for the respective ligands are shown as a subset on the respective plots.

A

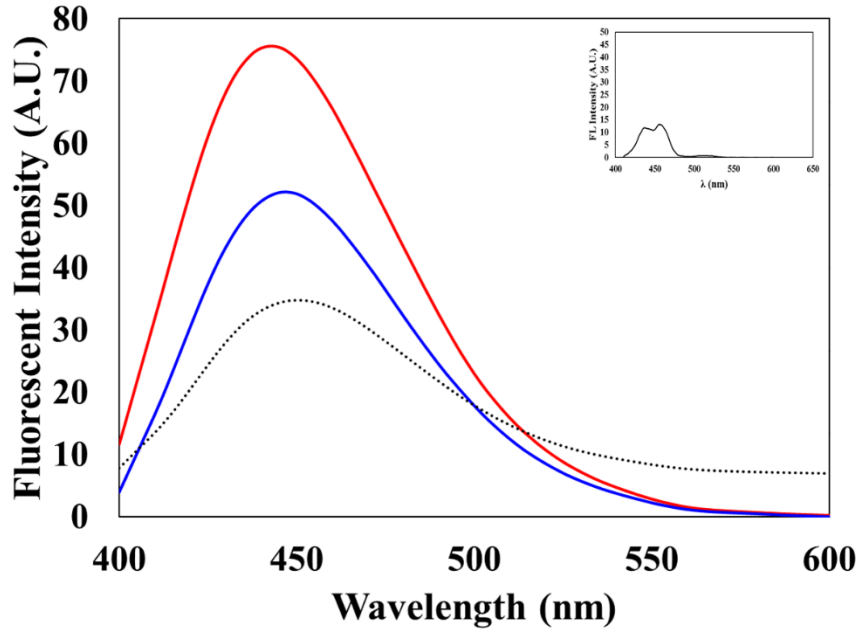

B

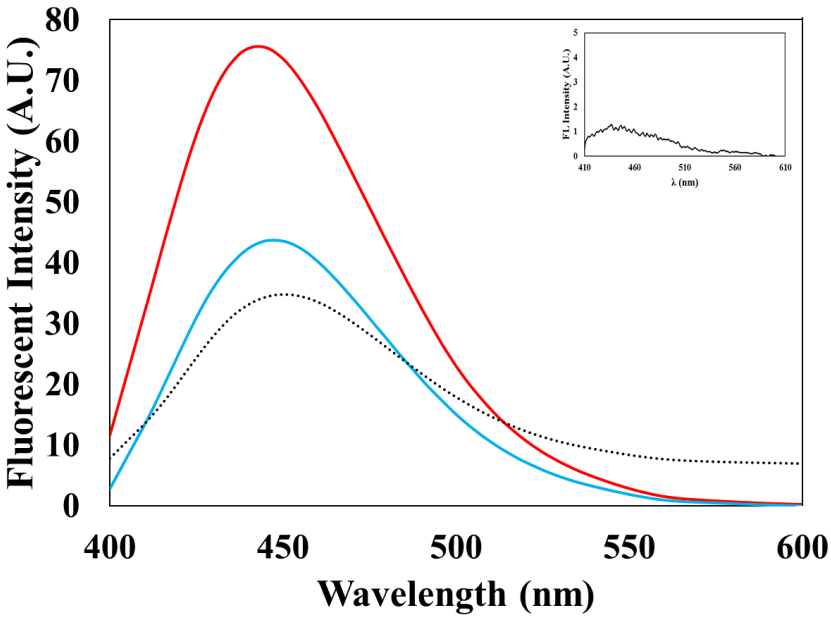

Figure 4.10: Mant-ATP fluorescence spectra of free and bound *Kp*NNAT
The above mant-ATP spectra represent mant-ATP:*Kp*NNAT (—), mant-ATP:*Kp*NNAT in the presence of ATP (—), mant-ATP:*Kp*NNAT in the presence of NAD^+ (—) and free mant-ATP in buffer (·····). All samples were prepared in 10 mM phosphate buffer with 5 mM magnesium chloride (pH 7.4), 10 µM mant-ATP, 5 µM *Kp*NNAT and 2 mM ligands. Bound *Kp*NNAT results in low mant-ATP fluorescent intensity with a longer wavelength emission to ~455 nm (blue shift). The binding of ATP and NAD^+ results in significantly low mant-ATP fluorescent intensity. The dotted spectrum used to correct the data. The inner filter effect for the respective ligands are shown as a subset on the respective plots. The inner filter effect for ATP is negligible when compared to free mant-ATP.

4.6 Thermodynamic Studies

4.6.1 Isothermal titration calorimetry

ITC experiments were performed to investigate the thermodynamic parameters during the binding of substrate ATP under consistent conditions. The binding thermograms and fitted data demonstrated an exothermic reaction ($\Delta H<0$) upon ATP binding to *Kp*NNAT. In addition, the reaction is entropically driven ($\Delta S>0$) and spontaneous ($\Delta G<0$) and exhibited a stoichiometry (n) of 3 (Figure 4.11) (Table 4.2). The thermodynamic parameters derived from the experiments are shown in the table below. The typical sigmoidal ITC curve was not achieved and thus produced thermodynamic parameters (change in enthalpy and stoichiometry) that cannot be fully trusted. However, the nature of these parameters can be used for analysis and correlates with previous studies (Sershon *et al*., 2009).

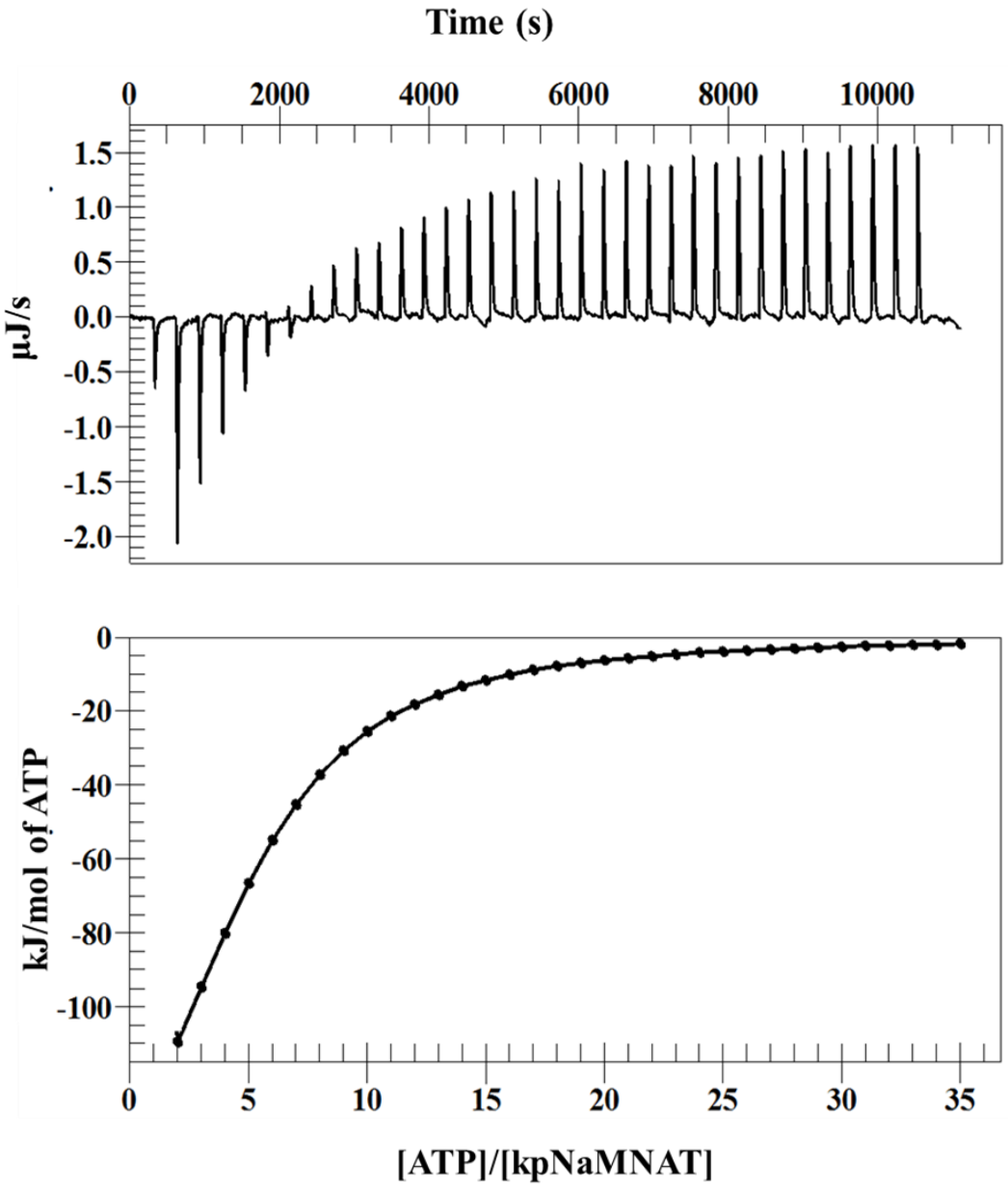

Figure 4.11: Isothermal titration calorimetric analysis of *Kp*NNAT with ATP

Figure depicts the titration of 37 µM *Kp*NNAT with 5 mM ATP in PBS (137 mM NaCl, 2.7 mM KCl, 10 mM Na_2HPO_4, 2 mM KH_2PO_4, pH 7.4) buffer at 298.15 K with a stirring rate of 310 rpm with a duration of 300 sec between each injection. The fitted data follows an independent model (single-site binding) derived from the NanoAnalyze software. The reaction is exothermic and spontaneous. The upper panel represents the raw data from the titration and the lower panel represents the fitted data.

Table 4.2: Thermodynamic parameters of ATP bound to *Kp*NNAT

Protein	Ligand	K_d (μM)	K_a	n	Δ*H*° (kJ/mol)	-TΔ*S*° (kJ/mol)	Δ*G*° (kJ/mol)
***Kp*NNAT**	ATP	69.1	14481.8	3	-8.1	-14.9	-23.8

All titrations were performed in filtered PBS buffer (pH 7.4) at 298.15 K
K_a, n and ΔH were retrieved from NanoAnalyze, independent model site binding.

CHAPTER 5:
OVERALL DISCUSSION, LIMITATIONS AND CONCLUSION

ESKAPE pathogens are responsible for causing nosocomial infections which threatens health-care systems across Africa (Elizabeth *et al*., 2016). These pathogens exhibit MDR to most current therapeutic options due to their effective virulence and drug resistance strategies such as drug inactivation, ligand modification, biofilm formation and efflux pumps (Obritsch *et al*., 2005). Current antibiotics like penicillin, cephalosporins and other β-lactam drugs need to be administered using combinational therapy to decrease the risk of bacterial resistance (Bush and Bradford, 2020). Thus, the urgency for new therapeutic options against ESKAPE pathogens is rising rapidly. A possible approach to drug therapy includes the targeting of essential bacterial enzymes. NNAT is one such enzyme which is responsible for the production of NAD^+, an essential cofactor for cell survival (Jayaram *et al*., 2011). Since the bacterial NNAT is significantly different (~20% sequence similarity) from its human counterpart, this allows the enzyme to be considered as a druggable target (Zhou *et al*., 2002) (Lau *et al*., 2009). Previous studies have been performed on NNAT from several species such as *H. sapiens* and several bacterial species like *E. coli*, but no studies have been considered for NNAT derived from *K. pneumoniae*. This is of concern since *K. pneumoniae* is responsible for more than 75% of infections in South Africa and is associated with high levels of drug resistance (Hirsch and Tam, 2010). Therefore, the analysis of NNAT derived from *K. pneumoniae* may provide insight into a possible drug therapy which would contribute positively towards combatting infections and prevent the spread of MDR pathogens. Thus, this study focused on the novel structural and functional analysis of *Kp*NNAT, a possible future drug target against nosocomial infections.

The optimised expression conditions resulted in the novel expression of tagged *Kp*NNAT (GST and hexahistidine tag) in the soluble fraction since a large band is visible at ~52 kDa in the supernatant lane (Figure 4.1). This is expected due to the presence of the GST tag which protects the expressed protein from degradation, allowing it to be stabilised in the soluble fraction (Young *et al*., 2012). Thus, the GST tag exhibits dual purposes in this study, that is, soluble protein expression and protein purification. The induction of cultures with IPTG also plays a significant role in the expression of *Kp*NNAT which demonstrates a vast difference in the expressed product without the addition of IPTG (Figure 4.1, supernatant with 0 mM IPTG).

The addition of IPTG allowed for overexpression of *Kp*NNAT which is fairly similar within the range of 0.25 mM to 1 mM.

Conventional methods for protein purification often require fusion tags such as GST tags, hexahistidine tags and others. These fusion tags often aid in purification due to their interactions with specific substrates which allow for the entrapment of proteins (Bell *et al*., 2013). Usually, these purifications involve a single tag which yields relatively pure protein samples (Bell *et al*., 2013). However, single protein purifications may lead to contaminants and dilution of the protein which will require additional steps to achieve purer protein samples (Zhao *et al*., 2013). Data from Figure 4.2A confirms contaminated protein samples achieved from a single GSH-Agarose purification, as indicated by the impurities present within the eluted fractions (elutions 2, 3 and 4). Thus, double purification with dual affinity tags permits the re-purification of proteins to prevent protein contamination while allowing one of the tags to be cleaved off simultaneously resulting in a high-throughput technique yielding (>95%) (see Supplementary table 1) purified protein (Zhao *et al*., 2013).

The specificity of this novel *Kp*NNAT purification (see Supplementary figure 2) process plays crucial roles in the manner in which *Kp*NNAT is purified. The location of the dual tags (GST and hexahistidine) is critical for the direction of protein purification and cleavage. Using the pGEX-4T-1 vector, the GST tag is encoded on the N-terminus of the expressed protein with a corresponding thrombin cleavage site shortly after the GST tag is encoded. The expressed protein had been designed to further encode for a hexahistidine tag on its N-terminus, thus placing the hexahistidine tag in between the GST tag and the expressed *Kp*NNAT. The reason behind this specific design was to allow the *Kp*NNAT to be subjected to initial GSH-Agarose purification and cleavage which allowed the uncleaved *Kp*NNAT and cleaved GST tag to remain on the GSH-Agarose column resulting in the eradication of unwanted protein species such as uncleaved protein or unwanted fusion tags. The advantage of the hexahistidine tag was then to trap the cleaved *Kp*NNAT and allow other contaminants such as thrombin to flow through resulting in a controlled and single elution of the Ni^{2+}-IMAC column to yield pure *Kp*NNAT. Furthermore, the decision to perform on-column or off-column cleavage will result in additional or fewer steps. Although both on-column and off-column cleavage would produce similar results, when performing off-column cleavage, additional steps such as GSH-Agarose elution (pre-cleavage, initial purification) and GSH-Agarose purification (post-cleavage, removal of GST tag species from protein) will need to be done. Thus, by performing on-column

cleavage ,purification and cleavage of *Kp*NNAT was simultaneously achieved without additional washes or dilutions while conserving the flow of protein between different affinity columns. A possible disadvantage regarding on-column cleavage is the aggregation of protein; however, Figure 4.3 exhibiting the protein spectrum, showed no sign of aggregation at 340 nm. The evaluation of the double purification, on-column cleavage technique can be observed in Figure 4.2.

The purification of *Kp*NNAT with both tags occurs primarily in the GSH-Agarose column. Since the GST tag is on the far end of the *Kp*NNAT N-terminus, the addition of thrombin allows the GST tag cleavage to occur simultaneously (on-column cleavage). Thus, once connected to the Ni^{2+}-IMAC column, only the cleaved hexahistidine-tagged *Kp*NNAT will be passed through the Ni^{2+}-IMAC column while the cleaved GST tag or uncleaved *Kp*NNAT remains attached to the GSH-Agarose column via the GST tag. Initial GSH-Agarose purification trials were performed to analyse this primary purification step prior to cleavage and secondary purification (Figure 4.2A). The purification was successful (thick band at ~52 kDa) but contained some impurities as shown by the additional bands (Figure 4.2A, elution 2, 3 and 4). Thus, there is a need for further purification. In addition, the use of detergent washes (Tween-20-PBS) did not disrupt the binding of the GST-tagged protein to the column since no bands were observed at ~52 kDa (Figure 4.2A, Tween wash) From Figure 4.2B, thrombin cleavage trials show that cleavage occurs within 5 min of incubation with *Kp*NNAT (~25 kDa), however, the presence of uncleaved *Kp*NNAT (~52 kDa) was observed. This is expected since thrombin cleavage is not always efficient (Guan and Dixon, 1991). Since overnight (16 hrs) cleavage resulted in the slightest band of uncleaved *Kp*NNAT (Figure 4.2B, 16 hr lane), subsequent purifications were associated with overnight thrombin incubation. On-column cleavage was confirmed from Figure 4.2D which shows the GSH-Agarose column elution of GST (~26 kDa). The protein bands at ~26 kDa represent the cleaved GST tag which was eluted from the GSH-affinity column. The cleaved hexahistidine-tagged *Kp*NNAT was then directly passed though the Ni^{2+}-IMAC column to trap the tagged enzyme and allow any impurities to flow through (including thrombin). At this stage, the GST tag, uncleaved *Kp*NNAT and thrombin were eradicated from the protein sample and controlled Ni^{2+}-IMAC elution occurred as indicated by the peak elution of cleaved hexahistidine-tagged *Kp*NNAT (Figure 4.2C, elution 3). The final Ni^{2+}-IMAC elution (Figure 4.2C) demonstrates the success of the double purification, on-column cleavage process as indicated by relatively clean and concentrated bands at ~25 kDa. However, there is a slight presence of an impurity at ~63 kDa which only

eluted with concentrated fractions of *Kp*NNAT. Nevertheless, the impurity is only present in specific samples and its size is relatively small in comparison to the protein band (>95% purity, see Supplementary table 1). Furthermore, the $A_{260/280}$ of 0.75 confirms the purity of the enzyme with regards to the absence of nucleic acids. An $A_{260/280}$ for relatively pure protein should not exceed 1.6 (Lucena-Aguilar *et al*., 2016). Thus, the value of 0.75 is an acceptable figure for protein purity.

The data from the purification profiles (Figure 4.2) demonstrates that the dual-purification, on-column cleavage technique produces high concentrations (Figure 4.4) of protein which are ~95% pure. This is of importance since protein yield, purity and activity are considered pre-requisites in any study surrounding structural biology.

NAD^+ detection through absorbance spectroscopy is difficult to achieve since other molecules such as NADH and nucleic acids exhibit an absorbance at a similar wavelength of 250 nm. Thus, an alternative technique to investigate the activity of *Kp*NNAT is the use of a coupled enzyme assay. This assay comprised of two different enzymes (*Kp*NNAT and ADH), thus forming a dual enzyme assay. The dual assay provides insight into the activity of *Kp*NNAT at varying pH levels. The addition of ADH in this assay has allowed for the formation of NADH which has been observed at 340 nm. The formation of this product acts as a measure of *Kp*NNAT activity. At a pH level 7.5 (PBS buffer), the specific activity read 0.0143 μmol/min/mg in comparison to a much higher specific activity (0.2408 μmol/min/mg) achieved at pH level 9 (Tris-HCl buffer) **(**Figure 4.6). The difference in specific activities is attributed to ADH which exhibits an optimal pH range of 8-9 (Figure 4.5) (Silverstein, 2016). Thus, higher specific activity is expected at pH level 9 as ADH functions optimally and converts NAD^+ more efficiently. This is further supported by the data retrieved from previous studies demonstrating the kinetic parameters of yeast ADH associated with pH level changes and indicates the optimal pH level 9 (Dickinson and Dickenson, 1975). Furthermore, it has been noted that the pH level becomes a determining factor of *Kp*NNAT activity since ADH controls the formation of the end product for the reaction. In addition, the specific activity for the assay is not a true representation of *Kp*NNAT activity (pseudo-specific activity), as it profoundly relies on ADH activity. Nevertheless, the production of NADH is only possible if NAD^+ is produced which relies on active *Kp*NNAT. Thus, the conditions for the secondary reaction in a coupled assay should be taken under consideration during experimental design. Furthermore, the conditions that validate a coupled enzyme assay have not been fully satisfied,

that is, the irreversible secondary reaction. Once the primary product is formed, it is simultaneously used as a substrate for the secondary reaction, therefore the reversibility of the primary reaction is diminished. However, the reversibility of the secondary reaction still exists, and the kinetics of the overall assay cannot be confirmed. Thus, the pseudo-specific activity attained from this coupled assay is only enough to indicate an active primary enzyme. Since the primary goal of this assay was to determine if the expressed *Kp*NNAT is active, the design of the dual assay enabled successful investigation of enzyme activity. Structural characterisation was thus carried out using active *Kp*NNAT.

Far UV CD has revealed a dominant α-helical secondary structure with a distinct peak at 190 nm (Figure 4.7). Previous literature supports this data which concluded that bacterial adenylyltransferases share a common secondary structure referred to as the Rossmann-fold, characterised by alternating α-helices and β-sheets (Zhai *et al*., 2009). This feature is imperative for substrate recognition and catalysis across NNATs. Bacterial NNATs, such as *Kp*NNAT, contain additional α-helices and β-sheets towards its C-terminus which plays a role in substrate preference (Zhang *et al*., 2002). The overall conservation of the secondary structure is imperative for catalysis since several helices are responsible for the substrate interactions (Zhang *et al*., 2002). The flexibility of these structural elements has also shown to be crucial in NNAT catalysis (Zhang *et al*., 2002). To further confirm the secondary structure of *Kp*NNAT, Dichroweb Tool (Whitmore and Wallace, 2004) was used. The NRMSD value of 0.1 lies within an acceptable range (0.1) and thus the data retrieved from Dichroweb can be used for secondary structural analysis (Whitmore and Wallace, 2004). The analysis resulted in a predominant α-helical secondary structure (38% in comparison to the other structural elements) (Table 4.1). This data correlates with the experimental data achieved which shows predominant α-helical secondary structural content (Figure 4.7). Furthermore, the presence of β-sheets (16%) reinforces the idea of the conserved Rossman-fold (α/β/α motif) in *Kp*NNAT. Interestingly, Dichroweb analysis also revealed a high content of unordered regions (26%). However, from the experimental data (Figure 4.7), the absence of a negative peak at ~200 nm demonstrates a lack of unordered structural elements (Figure 3.3) (Corrêa and Ramos, 2009). Nevertheless, the data from the experimental study and Dichroweb analysis correlate with each other regarding the predominant α-helical secondary structure which provides structural analysis that can otherwise not be attained without a high-resolution structure.

Changes in polarity have led to higher or lower tryptophan fluorescent intensities as well as shifts in emission wavelengths. Native *Kp*NNAT (folded) exhibited a high fluorescent intensity at 350 nm compared to the denatured state of *Kp*NNAT (Figure 4.8). Although there was no shift in emission wavelength, unfolded *Kp*NNAT revealed a low tryptophan fluorescent intensity which can be attributed to buried tryptophan residues exposed to a polar environment. This data reveals that the tryptophan residues should be located within clefts or hydrophobic patches which are slightly more buried than other portions of *Kp*NNAT. According to the predicted *Kp*NNAT structure and its gene sequence (Uniprot ID: B5XZR5), there are five tryptophan residues: Trp87, Trp95, Trp120, Trp152 and Trp179. These residues participate in vital interactions to support both the structure and function of *Kp*NNAT. Trp95 plays a dual role in secondary structure formation as well as aiding in ligand binding according to data shown by Zhang *et al*., 2002. Trp120 has an important role by occupying the pyridine binding site prior to substrate binding. Upon binding, Trp120 stacks favourably under the nicotinate ring creating stable stacking interactions (Zhai *et al*., 2009). Other tryptophan residues share similar roles in stabilising stacking interactions, closing active sites during product formation and interactions with specific substrates (Wang *et al*., 2017). These residues are highly conserved among all NNATs and due to their roles, they are located within the hydrophobic cores of the enzyme which correlate with the data (Figure 4.8) proposing buried tryptophan residues. In addition, these residues are highly conserved with *Ec*NNAT (Figure 2.11) further emphasising their importance in enzyme functionality.

Previous studies show that bacterial NNATs such as *Ec*NNAT, undergo drastic ligand-induced conformational changes at ATP and NaMN/NMN binding sites (Zhang *et al*., 2003). From the ANS displacement studies, a blue shift had occurred upon the binding of ANS to *Kp*NNAT in comparison to free ANS (Figure 4.9). This demonstrates the binding of ANS to *Kp*NNAT. ANS is an anionic probe that detects surface hydrophobicity. Interestingly, the data shows an increase in ANS quantum yield in the presence of ATP and NAD^+ respectively. Thus, the polarity of the *Kp*NNAT active site/s is influenced by the binding of substrates or products. Upon binding of the product, NAD^+, conformational changes of Asp109, Ser110 and Trp117 in *Ec*NNAT, allow interactions between these residues and the product (Zhang *et al*., 2002). Furthermore, the binding of NAD^+ produces a conformational change in Arg134 to facilitate interactions with the ATP molecule (Zhang *et al*., 2002). These ligand-induced conformations result in a more closed active site which covers almost 90% of the bound NAD^+ product permitting tight binding between the enzyme and the product (Zhang *et al*., 2002). These

induced conformations could be reason for the increase in ANS fluorescent intensity. Upon ATP binding to *Ec*NNAT, Arg134 and Arg185 are crucial to catalysis and undergo positional changes which may also contribute to a change in site polarity (Zhang *et al*., 2002). These residues that participate in ligand-induced conformations are conserved in *Kp*NNAT (Figure 2.11) and contribute to the ANS fluorescent intensity shown in Figure 4.9. The induced conformations upon ATP or NAD^+ binding independently may have resulted in a less exposed or a less polar pocket, which was bound by ANS, hence, the increase in ANS fluorescent intensity. Data from this experiment confirm the ligand-induced conformations experienced by bacterial NNATs upon a substrate or product binding.

Further analysis into ATP binding using mant-ATP confirmed the binding of ATP to *Kp*NNAT due to the blue shift (Figure 4.10) experienced in comparison to free mant-ATP. Upon the binding of ATP or NAD^+, in the presence of mant-ATP, the mant-ATP fluorescent intensity is lowered (Figure 4.10). As a result, mant-ATP fluorescence is quenched upon the binding of these molecules to *Kp*NNAT. Results from this experiment have shown that ATP alone binds a pocket with great hydrophobicity due to the increased mant-ATP intensity (Figure 4.10A). However, once bound with the product NAD^+, the polarity of the ATP binding site was influenced. According to previous crystal studies, the ATP binding site is described as a deep, yet solvent-accessible cleft (D'Angelo *et al*., 2000). This correlates well since ATP has both hydrophobic and hydrophilic structural features. In addition, NAD^+ is most likely located in a solvent-accessible cleft to allow for efficient product release (Saridakis *et al*., 2001). Since the binding of NAD^+ restricts or prevents the binding of ATP (Figure 4.10B), this could suggest that NAD^+ and ATP share the same or partial binding site. The reaction order, that is, the relationship between the concentrations of substrates or products and the reaction rate, for *Kp*NNAT is unknown, however, previous studies have shown that NNATs may follow an ordered sequential two-substrate mechanism of action (Lau *et al*., 2009). Thus, only the first substrate and the last product can bind to the enzyme, outcompeting one another for the site (Lau *et al*., 2009). This theory supports the data obtained in Figure 4.10 which indicates a possible competitive nature between NAD^+ and mant-ATP for the ATP binding site. Due to the nucleophilic attack by the 5' phosphate of the mononucleotide (NMN) on the α-phosphate of ATP during product formation (Figure 3.2), there is a possibility that the AMP portion of NAD^+ partially occupies the ATP site, thus preventing efficient ATP binding. In addition, previous literature confirms that *Ec*NNAT exhibits product inhibition which further reinforces the idea that the product of the *Kp*NNAT reaction may bind to a partial site that also binds a

specific substrate for the reaction (Mehl *et al*., 2000). Since the sequence similarity between *Ec*NNAT and *Kp*NNAT is high (~75%), studies performed on *Ec*NNAT can be used to interpret this *Kp*NNAT data. Furthermore, the decreased mant-ATP intensity observed upon ATP binding emphasises the specificity of ATP for the ATP binding site and demonstrates the conservative nature of the ATP binding site and motif across NNATs. In addition to the structural analysis of *Kp*NNAT, functional analysis was performed using ITC.

Derived from Nanoanalyze, the thermodynamic parameters of ITC revealed that an exothermic reaction (enthalpically favourable) upon ATP binding to *Kp*NNAT occurs (Figure 4.11). The results of this experiment correlate with previous studies performed by Sershon *et al*., 2009 with regards to the nature of the reaction between ATP and NNAT. In addition, this reaction is spontaneous in nature (ΔG = -23.8 kJ/mol) (Table 4.2) according to the data derived from ITC experiments. The model fitted to the raw data was an independent model (single site binding). Thus, ATP binds to only one site on *Kp*NNAT. This further emphasises the specificity of the ATP binding site.

From the thermodynamic parameters (Table 4.2), the binding of ATP requires interactions such as hydrogen bonding and hydrophobic interactions exhibited by the favourable enthalpy (Adams, 1980). The low entropy can be attributed to the flexibility of the water molecules due to the active site hydration and ATP interaction. During ATP binding, several water molecules participate in interactions with the phosphates of ATP and other active site residues such as Arg133 and Phe177 (Saridakis *et al.*, 2001) (Zhang *et al*., 2002) (D'Angelo *et al*., 2000). Thus, the low entropy suggests the flexibility of water molecules near the ATP binding site. Water molecules that are in proximity to the ligand binding site, often play crucial roles involved in the stabilisation of ligand binding and substrate specificity (Ladbury, 1996). In addition, these solvation effects surrounding the active sites due to ligand binding may exert effects on the overall enthalpy, entropy and free energy of the ligand binding reaction (Ladbry, 1996). A favourable enthalpy ($-\Delta H°$) and favourable entropy ($-T\Delta S°$) describes the flexibility of water molecules regarding ligand binding (Ladbury, 1996). The presence of hydrophobic interactions from active site residues such as tryptophan and phenylalanine may exert an opposing decrease in entropy that is not large enough to become unfavourable which contributes to the stabilising effect of ATP binding (Bronowska, 2011). In addition to the solvation effect by associated water molecules, ATP, the amphipathic ligand, may also contribute to the favourable entropy. The ATP binding motif across bacterial NNATs consists of histidine, glycine and tyrosine

which exhibits the amphipathic nature of binding (Huang *et al*., 2010). The polar histidine and tyrosine residues and non-polar glycine residue interact with the phosphates of ATP. Since the ligand is amphipathic, the ATP binding pocket cannot fully liberate water molecules due to the polar nature of ATP, thus this may contribute to the favourable entropy due to the flexibility of these water molecules to accommodate ATP binding. The energetics from this binding experiment only generalises the type of interactions that may exist when ATP binds to *Kp*NNAT at 25 °C (Connelly, 1994). Further analysis into enthalpic and entropic contributions can only be made using a crystal or molecular model of *Kp*NNAT to determine the accurate positions of various residues and water molecules.

The typical sigmoidal curve was not achieved during the ITC experiment which can be attributed to the large difference between ligand and protein concentration (Tshabalala *et al*., 2016). The curvature of an ITC plot is highly dependent on the Wiseman constant (*c*-value). This is a unitless value defined by the following equation:

$$c = \frac{n[\mathrm{P}]}{K_{\mathrm{d}}} \tag{14}$$

where *n* is the number of binding sites, P is the concentration of protein in the sample cell and K_{d} is the dissociation constant (Dutta *et al*., 2015).

The *c*-value parameter influences the shape of an ITC plot. To achieve an optimal sigmoidal curve, the *c*-value should range within 20-100 (Dutta *et al*., 2015). From the data used in the experiment and that which was derived from NanoAnalyze, the *c*-value for ATP binding to *Kp*NNAT was calculated to be 1.6. Thus, the sigmoidal curve was not achieved through the experiment. This could be due to the low enzyme concentration and high ligand concentration used in the experiment. The absence of an optimal sigmoidal curve influences the thermodynamic parameters that are derived from it. As seen in Figure 3.5, the stoichiometry and enthalpy are strongly influenced by the curvature of the data. Thus, the value of stoichiometry, enthalpy and Gibbs free energy are not reliable but the nature of the parameters (enthalpy and Gibbs free energy), that is, whether they are favourable or unfavourable, can be accepted since the *c*-value is greater than 1 (Broecker *et al*., 2011) (Turnbull 2005). The dissociation constant (69.1 μM) demonstrates weak binding between ATP and *Kp*NNAT. A possible cause for the weak binding achieved in the experiment could be due to the

concentrations of ATP and enzyme used. However, weak binding associated with ATP binding to *Kp*NNAT serves as beneficial data in drug design. A weak binding substrate may allow for drug targets to potentially bind to the same site, outcompeting the natural substrate. In order to achieve optimal binding affinities, the concentration of reactants should match the optimal binding range of the reactant (Winiewska *et al.*, 2017). Further analysis of ITC data can be performed by titrating other ligands and performing molecular docking of *Kp*NNAT with its ligands. In addition, higher concentrations of ligands need to be used to obtain a sigmoidal curve which produces accurate thermodynamic parameters.

Limitations and future work

Due to the novelty of this study, there are several limitations to consider. The coupled assay did not provide a direct measurement of the specific activity of *Kp*NNAT, resulting in a pseudo-specific activity. The coupled assay was necessary since the primary product, NAD^+ was undetectable through absorbance spectroscopy, thus, the reaction was coupled with ADH. An alternate technique that should be used to derive direct parameters from the *Kp*NNAT reaction, is the use of ITC. Under steady-state conditions, multiple injections of the ligand into enzyme can be performed. From the ITC data, the heat produced (Q) can be used to measure reaction rates as indicated in the equations below (Frasca, 2016):

$$Q = n\Delta H_{app} = [P]_{total} V\, \Delta H_{app} \tag{15}$$

where Q represents power, n represents stoichiometry, ΔH_{app} represents the change in apparent enthalpy, V represents the volume of the cell and P represents product.

$$\text{Rate} = \frac{1}{V\, \Delta H_{app}} \times \frac{dQ}{dt} \tag{16}$$

The Michealis-Menten plot which derives various kinetic parameters such as maximal velocity (V_{max}) and the Michealis constant (K_M) can also be created using ITC data. For instance, the molar enthalpy is derived through ITC experiments involving the integration of peak measurements to produce the total heat which can then be divided by the substrate concentration. In addition to this parameter, the equilibrium association constant for the enzyme-substrate complex can be investigated by performing an ITC experiment that limits

product formation (Frasca, 2016). Further derivation of parameters such as the catalytic constant (k_{cat}) can be attained by changing the substrate and enzyme concentrations (Frasca, 2016). Previous studies indicate the successes associated with ITC experiments for the analysis of enzyme reactions (Noske *et al*, 2010) (Aguirre *et al*, 2015).

To further understand the function of various water molecules in proximity to the *Kp*NNAT active site, additional ITC experiments can be performed. These experiments should substitute ligands or parts of ligands for water molecules to analyse the effect on the free energy, binding affinities and entropy associated with the reaction (Ladbury, 1996). However, the requirements for such an experiment are solved crystal structures, known water molecule sites and locations (Ladbury, 1996). Data from these experiments can potentially aid in drug design to increase the affinities of drugs to the enzyme binding site due to adaptations of the binding site by water molecules (Ladbury, 1996).

Insights into the binding displacements for *Kp*NNAT can be further explored using additional ANS and mant-ATP experiments. These experiments can also be performed with various substrates and drugs that may provide data on *Kp*NNAT inhibition for drug design. Additionally, inhibition studies using ITC can provide details on the inhibition of *Kp*NNAT activity. A future wholistic approach requires the crystallisation of *Kp*NNAT (with and without substrates) in addition to molecular docking with the various substrates. Thus, the associated binding events can be thoroughly analysed and create a platform for drug design to inactivate or inhibit *Kp*NNAT activity.

Conclusion

Data from this investigation aided in bacterial NNAT research which positively contributes to the ESKAPE pathogen crisis in Africa to this date. Targeting a crucial factor in bacterial metabolism may reveal new insights into drug therapy. This study was conducted to gain insight into a potential target in bacterial cells. Previous studies have provided a platform of research surrounding NNATs from bacterial organisms such as *E. coli*, *P. falciparum*, *B. anthracis* and several others. However, to date, there is no research investigating the structure and function of *Kp*NNAT, an important member of the ESKAPE pathogens.

*Kp*NNAT was successfully overexpressed and purified for the first time using novel approaches. The double purification, on-column cleavage approach proved to be a successful

and efficient technique in yielding pure active protein. Using a dual enzyme assay the enzyme indirectly demonstrated activity which varied in different pH conditions thereby limiting the analysis of *Kp*NNAT activity. Future work can include a direct approach to investigate the activity of *Kp*NNAT. Structural analysis of *Kp*NNAT revealed the conservation of secondary and tertiary structures between bacterial NNATs. Upon the binding of ATP and NAD^+ to *Kp*NNAT, ligand-induced conformations are exhibited which may alter the polarity of the active sites. An exothermic and spontaneous reaction occurs upon the binding of ATP to *Kp*NNAT. The ATP binding site can be characterised as an amphipathic site accommodating both polar and non-polar residues. This binding may be interrupted upon the formation of NAD^+ due to the possibility that the two ligands occupy the same portions of the binding cavity. The nature of this possible competitive binding is unknown, thus, further studies involving competitive inhibition studies are necessary. This study revealed novel structural and functional characteristics regarding *Kp*NNAT utilising unique and interesting techniques such as dual-tag double purification, on-column cleavage and dual enzyme assays. The successful novel expression and purification of active *Kp*NNAT is sufficient evidence to further pursue this enzyme as a possible druggable target as it is a determining factor in structural biochemistry. Further examination into ligand binding and binding affinities should be explored for drug design. Infections caused by MDR *K. pneumoniae* is rising rapidly in South Africa, thus, the dire need for new potential drug candidates against this bacterium is paramount. Data from this research has thus provided a unique structural and functional advancement that can be associated with drug design and research surrounding the ESKAPE pathogen crisis in Africa.

REFERENCES

ACIKARA, Ö.B., ÇITOĞLU, G.S., ÖZBILGIN, S., ERGENE, B., (2013). Affinity Chromatography and Importance in Drug Discovery. Column Chromatography.

ADAMS, P.A., (1980). The interpretation of entropy/enthalpy compensation phenomena in the deacylation of acyl-alpha-chymotrypsins. *Biochem J* 191, 653–655.

AGUIRRE, C., CONDADO-MORALES, I., OLGUIN, L.F., COSTAS, M., (2015). Isothermal titration calorimetry determination of individual rate constants of trypsin catalytic activity. *Anal. Biochem*. 479, 18–27.

AITKEN, A., LEARMONTH, M.P., (2002). Protein Determination by UV Absorption, in: Walker, J.M. (Ed.), *The Protein Protocols Handbook*. Humana Press, Totowa, NJ, pp. 3–6

AMARO, R.E. (2017). Toward Understanding "the Ways" of Allosteric Drugs. *ACS Cent Sci* 3, 925–926.

AZEVEDO, P.A.A., FURLAN, J.P.R., OLIVEIRA-SILVA, M., NAKAMURA-SILVA, R., GOMES, C.N., COSTA, K.R.C., STEHLING, E.G., PITONDO-SILVA, A., (2018). Detection of virulence and β-lactamase encoding genes in Enterobacter aerogenes and Enterobacter cloacae clinical isolates from Brazil. *Brazilian Journal of Microbiology* 49, 224–228.

BAGHERI NEJAD, S., ALLEGRANZI, B., SYED, S. B., ELLIS, B. & PITTET, D. (2011). Health-care-associated inf*Ec*tion in Africa: a systematic review. *Bulletin of the World Health Organization,* 89**,** 757-765.

BARBAS, A., POPESCU, A., FRAZAO, C., ARRAIANO, C. M. & FIALHO, A. M. (2013). Rossmann-fold motifs can confer multiple functions to metabolic enzymes: RNA binding and ribonuclease activity of a UDP-glucose dehydrogenase. *Biochem Biophys Res Commun,* 430**,** 218-24.

BASSETTI, M., VENA, A., CROXATTO, A., RIGHI, E., GUERY, B., (2018). How to manage Pseudomonas aeruginosa infections. *Drugs Context* 7.

BELL, M.R., ENGLEKA, M.J., MALIK, A., STRICKLER, J.E., (2013). To fuse or not to fuse: What is your purpose? *Protein Sci* 22, 1466–1477.

BEN SHIMON, M., LENZ, M., IKENBERG, B., BECKER, D., SHAVIT STEIN, E., CHAPMAN, J., TANNE, D., PICK, C. G., BLATT, I., NEUFELD, M., VLACHOS, A., & MAGGIO, N. (2015). Thrombin regulation of synaptic transmission and plasticity: implications for health and disease. *Frontiers in cellular neuroscience,* 9, 151.

BENNETT, P.M., (2008). Plasmid encoded antibiotic resistance: acquisition and transfer of antibiotic resistance genes in bacteria. Br J *Pharmacol* 153, S347–S357.

BERGOGNE-BEREZIN, E. (1999). Current guidelines for the treatment and prevention of nosocomial infections. *Drugs,* 58**,** 51-67.

BIAN, X. & LOCKLESS, S. W. (2016). Preparation To Minimize Buffer Mismatch in Isothermal Titration Calorimetry Experiments. *Anal Chem,* 88**,** 5549-53.

BIEN, J., SOKOLOVA, O., BOZKO, P., (2011). Characterization of Virulence Factors of Staphylococcus aureus: Novel Function of Known Virulence Factors That Are Implicated in Activation of Airway Epithelial Proinflammatory Response. *J Pathog*.

BISSWANGER, H., (2014). Enzyme assays. Perspectives in Science, Reporting Enzymology Data – STRENDA Recommendations and Beyond 1, 41–55.

BODEY, G.P., BOLIVAR, R., FAINSTEIN, V., JADEJA, L., (1983). Infections caused by Pseudomonas aeruginosa. *Rev. Infect. Dis*. 5, 279–313.

BOOTH, W.T., SCHLACHTER, C.R., POTE, S., USSIN, N., MANK, N.J., KLAPPER, V., OFFERMANN, L.R., TANG, C., HURLBURT, B.K., CHRUSZCZ, M., (2018). Impact of an N-terminal Polyhistidine Tag on Protein Thermal Stability. *ACS Omega 3*, 760–768.

BORNHORST, J. A. & FALKE, J. J. (2000). Purification of proteins using polyhistidine affinity tags. *Methods Enzymol*, 326**,** 245-54.

BROECKER, J., VARGAS, C., KELLER, S., (2011). Revisiting the optimal cvalue for isothermal titration calorimetry. *Analytical Biochemistry* 418, 307–309.

BRONOWSKA, A.K., (2011). Thermodynamics of Ligand-Protein Interactions: Implications for Molecular Design. Thermodynamics - Interaction Studies - Solids, Liquids and Gases.

BRUNETTI, L., DI STEFANO, M., RUGGIERI, S., CIMADAMORE, F., MAGNI, G., (2010). Homology modeling and deletion mutants of human nicotinamide mononucleotide adenylyltransferase isozyme 2: New insights on structure and function relationship. *Protein Sci* 19, 2440–2450.

BURMEISTER, A. R. (2015). Horizontal Gene Transfer. *Evolution, Medicine, and Public Health*, 2015**,** 193-194.

BUSH, K., BRADFORD, P.A., (2016). β-Lactams and β-Lactamase Inhibitors: An Overview. Cold Spring Harb Perspect Med 6, a025247.

CALFEE, D. P. (2017). Recent advances in the understanding and management of Klebsiella pneumoniae. *F1000Res*, 6**,** 1760.

CONNELLY, P.R., (1994). Acquisition and use of calorimetric data for prediction of the thermodynamics of ligand-binding and folding reactions of proteins. *Current Opinion in Biotechnology* 5, 381–388.

COPE, G., COPE, A. (2013). Antibiotic resistance and how to act on it. *Dental Nursing* 9, 706–709.

CORRÊA, D., RAMOS, C., (2009). The use of circular dichroism spectroscopy to study protein folding, form and function. *African Journal of Biochemistry Research* 3, 164–173.

CREW, B., (2014). New Report Says Antimicrobial Resistance Will Kill 300 Million by 2050. ScienceAlert.

CRICHTON, R.R., (2008). 12 - Zinc: Lewis Acid and Gene Regulator, in: Crichton, R.R. (Ed.), *Biological Inorganic Chemistry*. Elsevier, Amsterdam, pp. 197–210.

D'ANGELO, I., RAFFAELLI, N., DABUSTI, V., LORENZI, T., MAGNI, G., RIZZI, M., (2000). Structure of nicotinamide mononucleotide adenylyltransferase: a key enzyme in NAD+ biosynthesis. *Structure* 8, 993–1004.

DAVIN-REGLI, A., PAGÈS, J.-M., (2015). Enterobacter aerogenes and Enterobacter cloacae; versatile bacterial pathogens confronting antibiotic treatment. *Front. Microbiol*. 6.

DE CASTRO, E., SIGRIST, C.J.A., GATTIKER, A., BULLIARD, V., LANGENDIJK-GENEVAUX, P.S., GASTEIGER, E., BAIROCH, A., HULO, N., (2006). ScanProsite: detection of PROSITE signature matches and ProRule-associated functional and structural residues in proteins. *Nucleic Acids Research* 34, W362–W365.

DICKENSON, C.J., DICKINSON, F.M., (1975). A study of the pH- and temperature-dependence of the reactions of yeast alcohol dehydrogenase with ethanol, acetaldehyde and butyraldehyde as substrates. *Biochem* J 147, 303–311

DILALLO, H., (2018). NDM-1: Metallobetalactamases (MBLs) and Antibiotic Resistance. *Chemistry LibreTexts*.

DONLAN, R.M. (2001). Biofilm Formation: A Clinically Relevant Microbiological Process. *Clin Infect Dis* 33, 1387–1392.

DOORDUIJN, D.J., ROOIJAKKERS, S.H.M., VAN SCHAIK, W., BARDOEL, B.W., (2016). Complement resistance mechanisms of Klebsiella pneumoniae. Immunobiology, SI: XXVI ICW Kanazawa 2016 221, 1102–1109.

DUTTA, A.K., RÖSGEN, J., RAJARATHNAM, K., (2015). Using Isothermal Titration Calorimetry to Determine Thermodynamic Parameters of Protein–Glycosaminoglycan Interactions. *Methods Mol Biol* 1229, 315–324.

DŽIDIĆ, S., ŠUŠKOVIĆ, J., KOS, B. (2008). Antibiotic resistance mechanisms in bacteria: Biochemical and genetic aspects. *Food Technology and Biotechnology* 46, 11–21.

EDENBERG, H. J. (2007). The genetics of alcohol metabolism: role of alcohol dehydrogenase and aldehyde dehydrogenase variants. *Alcohol Res Health*, 30**,** 5-13.

ELIZABETH, M., MBOTO, C. & AGBO, B. (2016). A Review of Nosocomial Infections in Sub-Saharan Africa.

ESSEL, V., TSHABALALA, K., NTSHOE, G., MPHAPHULI, E., FELLER, G., SHONHIWA NEE RAKGANTSO, A., MCCARTHY, K., ISMAIL, H., STRASHEIM, W., LOWE, M., PEROVIC, O., HLONIPHO, M., GOVENDER, N. (2020). A multisectoral investigation of a neonatal unit outbreak of Klebsiella pneumoniae bacteraemia at a regional hospital in Gauteng Province, South Africa. *South African Medical Journal* 110, 783.

FRANCHETTI, P., CAPPELLACCI, L., PASQUALINI, M., GRIFANTINI, M., LORENZI, T., RAFFAELLI, N., MAGNI, G. (2003). Dinucleoside Polyphosphate NAD Analogs as Potential NMN Adenylyltransferase Inhibitors. Synthesis and Biological Evaluation. *Nucleosides, nucleotides & nucleic acids* 22, 865–8.

FRASCA, V., (2016). Using Isothermal Titration Calorimetry Techniques to Quantify Enzyme Kinetics. *Industrial Biotechnology* 12, 207–211.

FUKUOKA, T., OHYA, S., NARITA, T., KATSUTA, M., IIJIMA, M., MASUDA, N., YASUDA, H., TRIAS, J., NIKAIDO, H. (1993). Activity of the carbapenem panipenem and role of the OprD (D2) protein in its diffusion through the Pseudomonas aeruginosa outer membrane. *Antimicrobial agents and chemotherapy* 37, 322–7.

GARAVAGLIA, S., D'ANGELO, I., EMANUELLI, M., CARNEVALI, F., PIERELLA, F., MAGNI, G., RIZZI, M., (2002). Structure of Human NMN Adenylyltransferase A key nuclear enzyme for nad homeostasis. *J. Biol. Chem*. 277, 8524–8530.

GARRETT, R. AND GRISHAM, C., (2008). Biochemistry. 4th ed. pp.390-395

GASTEIGER, E., HOOGLAND, C., GATTIKER, A., DUVAUD, S., WILKINS, M.R., APPEL, R.D., BAIROCH, A., (2005). Protein Identification and Analysis Tools on the ExPASy Server, in: Walker, J.M. (Ed.), The Proteomics Protocols Handbook. Humana Press, Totowa, NJ, pp. 571–607.

GHEORGHE, I., POPA, M., MĂRUȚESCU, L.G., (2018). Molecular Features of Virulence and Resistance Mechanisms in Nosocomial and Community-Acquired Staphylococcus aureus. Staphylococcus Aureus.

GHISAIDOOBE, A. B. T. & CHUNG, S. J. (2014). Intrinsic tryptophan fluorescence in the detection and analysis of proteins: a focus on Förster resonance energy transfer techniques. *International journal of molecular sciences,* 15**,** 22518-22538.

GIEDRAITIENĖ, A., VITKAUSKIENĖ, A., NAGINIENĖ, R., PAVILONIS, A. (2011). Antibiotic resistance mechanisms of clinically important bacteria. *Medicina* (Kaunas) 47, 137–146.

GREENFIELD, N. J. (2006). Using circular dichroism spectra to estimate protein secondary structure. *Nature protocols,* 1**,** 2876-2890.

GUAN, K., DIXON, J.E., (1991). Eukaryotic proteins expressed in Escherichia coli: An improved thrombin cleavage and purification procedure of fusion proteins with glutathione S-transferase. *Analytical Biochemistry* 192, 262–267.

GUNNELL, E., (2019). How Strong is Your Binding? A Quick Introduction to Isothermal Titration Calorimetry. Bitesize Bio.

GUPTA, A., AMPOFO, K., RUBENSTEIN, D. & SAIMAN, L. (2003). Extended spectrum beta lactamase-producing Klebsiella pneumoniae infections: a review of the literature. *J Perinatol,* 23**,** 439-43.

HARDING, C.M., HENNON, S.W., FELDMAN, M.F., (2018). Uncovering the mechanisms of Acinetobacter baumannii virulence. *Nat Rev Microbiol* 16, 91–102.

HARPER, S. & SPEICHER, D. W. (2011). Purification of proteins fused to glutathione S-transferase. *Methods Mol Biol,* 681**,** 259-80.

HAUSER, A.R., (2011). Pseudomonas aeruginosa: So Many Virulence Factors, So Little Time. *Crit Care Med* 39, 2193–2194.

HAWE, A., SUTTER, M. & JISKOOT, W. (2008). Extrinsic fluorescent dyes as tools for protein characterization. *Pharmaceutical research,* 25**,** 1487-1499.

HIRSCH, E. B. & TAM, V. H. (2010). Detection and treatment options for Klebsiella pneumoniae carbapenemases (*KP*Cs): an emerging cause of multidrug-resistant infection. *J Antimicrob Chemother,* 65**,** 1119-25.

HOWARD, A., O'DONOGHUE, M., FEENEY, A., SLEATOR, R.D., (2012). Acinetobacter baumannii. *Virulence* 3, 243–250.

HUANG, N., KOLHATKAR, R., EYOBO, Y., SORCI, L., RODIONOVA, I., OSTERMAN, A.L., MACKERELL, A.D., ZHANG, H., (2010). Complexes of bacterial nicotinate mononucleotide adenylyltransferase with inhibitors: implication for structure-based drug design and improvement. *J Med Chem* 53, 5229–5239.

INCE C., COREMANS J.M.C.C., BRUINING H.A. (1992) In Vivo NADH Fluorescence. In: Erdmann W., Bruley D.F. (eds) Oxygen Transport to Tissue XIV. *Advances in Experimental Medicine and Biology*, vol 317. Springer, Boston, MA

ISMAIL, H., LOWMAN, W., GOVIND, C.N., SWE-HAN, K.S., MALOBA, M.R.B., BAMFORD, C., PEROVIC, O., (2019). Surveillance and comparison of antimicrobial susceptibility patterns of ESKAPE organisms isolated from patients with bacteraemia in South Africa, 2016 - 2017. *South African Medical Journal* 109, 934-940–940.

IWERIEBOR, B.C., OBI, L.C., OKOH, A.I., (2015). Virulence and antimicrobial resistance factors of Enterococcusspp. isolated from fecal samples from piggery farms in Eastern Cape, South Africa. *BMC Microbiol* 15.

JAFARI, M., MEHRNEJAD, F., RAHIMI, F., ASGHARI, S.M., (2018). The Molecular Basis of the Sodium Dodecyl Sulfate Effect on Human Ubiquitin Structure: A Molecular Dynamics Simulation Study. *Scientific*

JAYARAM, H. N., KUSUMANCHI, P. & YALOWITZ, J. A. (2011). NNAT expression and its relation to NAD metabolism. *Curr Med Chem,* 18**,** 1962-72.

KANG, C. I., KIM, S. H., PARK, W. B., LEE, K. D., KIM, H. B., KIM, E. C., OH, M. D. & CHOE, K. W. (2004). Bloodstream infections due to extended-spectrum beta-lactamase-producing Escherichia coli and Klebsiella pneumoniae: risk factors for mortality and treatment outcome, with special emphasis on antimicrobial therapy. *Antimicrob Agents Chemother,* 48**,** 4574-81.

KARAH, N., (2011). Identification, molecular epidemiology, and antibiotic resistance characterization of Acinetobacter spp. clinical isolates.

KHAN, H.A., BAIG, F.K., MEHBOOB, R., (2017). Nosocomial infections: Epidemiology, prevention, control and surveillance. *Asian Pacific Journal of Tropical Biomedicine* 7, 478–482.

KUMAR, P., (2015). Initial Velocity Measurement of a Chemical Reaction (With Diagram). Biology Discussion

LADBURY, J.E., (1996). Just add water! The effect of water on the specificity of protein-ligand binding sites and its potential application to drug design. *Chemistry & Biology* 3, 973–980.

LAEMMLI, U.K., (1970). Cleavage of Structural Proteins during the Assembly of the Head of Bacteriophage T4. *Nature* 227, 680–685.

LAU, C., NIERE, M. & ZIEGLER, M. (2009). The NMN/NaMN adenylyltransferase (NNAT) protein family. *Front Biosci (Landmark Ed),* 14**,** 410-31.

LAURINO, P., TOTH-PETROCZY, A., MEANA-PAÑEDA, R., LIN, W., TRUHLAR, D., TAWFIK, D., (2016). An Ancient Fingerprint Indicates the Common Ancestry of Rossmann-Fold Enzymes Utilizing Different Ribose-Based Cofactors. *PLOS Biology* 14, e1002396

LESKOVAR, A. & REINSTEIN, J. (2008). Photophysical properties of popular fluorescent adenosine nucleotide analogs used in enzyme mechanism probing. *Arch Biochem Biophys,* 473**,** 16-24.

LIN, H., KWAN, A. L. & DUTCHER, S. K. (2010). Synthesizing and salvaging NAD: lessons learned from Chlamydomonas reinhardtii. *PLoS Genet*, 6**,** e1001105.

LOW, Y.-M., YAP, P. S.-X., ABDUL JABAR, K., PONNAMPALAVANAR, S., KARUNAKARAN, R., VELAYUTHAN, R., CHONG, C.-W., ABU BAKAR, S., MD YUSOF, M. Y. & TEH, C. S.-J. (2017). The emergence of carbapenem resistant Klebsiella pneumoniae in Malaysia: correlation between microbiological trends with host characteristics and clinical factors. *Antimicrobial resistance and infection control*, 6**,** 5-5.

LUCENA-AGUILAR, G., SÁNCHEZ-LÓPEZ, A.M., BARBERÁN-ACEITUNO, C., CARRILLO-ÁVILA, J.A., LÓPEZ-GUERRERO, J.A., AGUILAR-QUESADA, R., (2016). DNA Source Selection for Downstream Applications Based on DNA Quality Indicators Analysis. *Biopreserv Biobank* 14, 264–270.

MAGNI, G., DI STEFANO, M., ORSOMANDO, G., RAFFAELLI, N., RUGGIERI, S. (2009). NAD(P) biosynthesis enzymes as potential targets for selective drug design. *Curr. Med. Chem*. 16, 1372–1390.

MAJOREK, K.A., KUHN, M.L., CHRUSZCZ, M., ANDERSON, W.F., MINOR, W., (2014). Double trouble—Buffer selection and His-tag presence may be responsible for nonreproducibility of biomedical experiments. *Protein Sci* 23, 1359–1368.

MANNS, J. M. (2011). SDS-Polyacrylamide Gel Electrophoresis (SDS-PAGE) of Proteins. *Current Protocols in Microbiology*, 22**,** A.3M.1-A.3M.13.

MARKWART, R., WILLRICH, N., HALLER, S., NOLL, I., KOPPE, U., WERNER, G., *EC*KMANNS, T., REUSS, A., (2019). The rise in vancomycin-resistant Enterococcus faecc*i*um in Germany: data from the German Antimicrobial Resistance Surveillance (ARS). *Antimicrob Resist Infect Control* 8, 147.

MAURICE, F., BROUTIN, I., PODGLAJEN, I., BENAS, P., COLLATZ, E., DARDEL, F. (2008). Enzyme structural plasticity and the emergence of broad-spectrum antibiotic resistance. *EMBO Rep*. 9, 344–349.

MAVEYRAUD, L., MOUREY, L. (2020). Protein X-ray Crystallography and Drug Discovery. *Molecules* 25.

MD, OBRITSCH., DN, FISH., R, MACLAREN., R, JUNG., (2005). Nosocomial Infections Due to Multidrug-Resistant Pseudomonas Aeruginosa: Epidemiology and Treatment Options Pharmacotherapy.

MEHL, R.A., KINSLAND, C., BEGLEY, T.P., (2000). Identification of the Escherichia coliNicotinic Acid Mononucleotide Adenylyltransferase Gene. *J. Bacteriol*. 182, 4372–4374.

MOOSAVI-MOVAHEDI, A.A., (2005). Thermodynamics of protein denaturation by sodium dodecyl sulfate. *JICS* 2, 189–196.

MULANI, M.S., KAMBLE, E.E., KUMKAR, S.N., TAWRE, M.S., PARDESI, K.R. (2019). Emerging Strategies to Combat ESKAPE Pathogens in the Era of Antimicrobial Resistance: A Review. *Front Microbiol* 10.

NAIR, A., STEINBERG, W. J., HABIB, T., SAEED, H. & RAUBENHEIMER, J. E. (2018). Prevalence of healthcare-associated inf*Ec*tion at a tertiary hospital in the Northern Cape Province, South Africa. *South African Family Practice*, 60**,** 162-167.

NARHI, L.O., CAUGHEY, D.J., HORAN, T., KITA, Y., CHANG, D., ARAKAWA, T. (1997). Effect of Three Elution Buffers on the Recovery and Structure of Monoclonal Antibodies. *Analytical Biochemistry* 253, 236–245.

NIKAIDO, H., PAGÈS, J.-M. (2012). Broad-specificity efflux pumps and their role in multidrug resistance of Gram-negative bacteria. *FEMS Microbiology Reviews* 36, 340–363.

NOBLE, J. E. (2014). Quantification of protein concentration using UV absorbance and Coomassie dyes. *Methods Enzymol,* 536**,** 17-26.

NORMAN, A., HANSEN, L. H. & SORENSEN, S. J. (2009). Conjugative plasmids: vessels of the communal gene pool. *Philos Trans R Soc Lond B Biol Sci,* 364**,** 2275-89.

NOSKE, R., CORNELIUS, F., CLARKE, R., (2010). Investigation of the enzymatic activity of the Na+,K+-ATPase via isothermal titration microcalorimetry. *Biochimica et biophysica acta* 1797, 1540–5.

ŐSZ, J., BODÓ, G., BRANCA, R.M.M., BAGYINKA, C., (2005). Theoretical Calculations on Hydrogenase Kinetics: Explanation of the Lag Phase and the Enzyme Concentration Dependence of the Activity of Hydrogenase Uptake. *Biophys J* 89, 1957–1964.

PANDEY, N., CASCELLA, M., (2020). Beta Lactam Antibiotics, in: StatPearls. StatPearls Publishing, Treasure Island (FL).

PANG, Z., RAUDONIS, R., GLICK, B., LIN, T.-J., CHENG, Z., (2018). Antibiotic resistance in Pseudomonas aeruginosa: mechanisms and alternative therapeutic strategies. *Biotechnology Advances.*

PAPP-WALLACE, K. M., ENDIMIANI, A., TARACILA, M. A. & BONOMO, R. A. (2011). Carbapenems: past, present, and future. *Antimicrob Agents Chemother,* 55**,** 4943-60.

PARAKHIA, M.V., (2009). Molecular Biology and Biotechnology: Microbial Methods. New India Publishing.

PATEL, J. T., BELSHAM, H. R., RATHBONE, A. J. & FRIEL, C. T. (2014). Use of stopped-flow fluorescence and labeled nucleotides to analyze the ATP turnover cycle of kinesins. *J Vis Exp***,** e52142.

PEARSE, J., (1997). Infection control in Africa. Nosocomial infection. *Afr Health* 19, 10–11.

PEROVIC, O., ISMAIL, H., QUAN, V., BAMFORD, C., NANA, T., CHIBABHAI, V., BHOLA, P., RAMJATHAN, P., SWE SWE-HAN, K., WADULA, J., WHITELAW, A., SMITH, M., MBELLE, N., SINGH-MOODLEY, **A.** (2020). Carbapenem-resistant Enterobacteriaceae in patients with bacteraemia at tertiary hospitals in South Africa, 2015 to 2018. *Eur J Clin Microbiol Infect Dis* 39, 1287–1294.

PEROVIC, O., ISMAIL, H., VAN SCHALKWYK, E., LOWMAN, W., PRENTICE, E., SENEKAL, M., GOVIND, C.N. (2018). Antimicrobial resistance surveillance in the South African private sector report for 2016. *Southern African Journal of Infectious Diseases* 33, 114–117.

PIERCE, M. M., RAMAN, C. S. & NALL, B. T. (1999). Isothermal titration calorimetry of protein-protein interactions. *Methods,* 19**,** 213-21.

PLAPP, B.V., (2010). Conformational Changes and Catalysis by Alcohol Dehydrogenase. Arch *Biochem Biophys* 493, 3–12.

PODSCHUN, R. & ULLMANN, U. (1998). Klebsiella spp. as nosocomial pathogens: epidemiology, taxonomy, typing methods, and pathogenicity factors. *Clin Microbiol Rev,* 11**,** 589-603.

RAMSAMY, Y., ESSACK, S.Y., SARTORIUS, B., PATEL, M., MLISANA, K.P. (2018). Antibiotic resistance trends of ESKAPE pathogens in Kwazulu-Natal, South Africa: A five-year retrospective analysis. *Afr J Lab Med* 7.

REHMAN, I., BOTELHO, S., (2018). *Biochemistry, Secondary Protein Structure*, in: StatPearls. StatPearls Publishing, Treasure Island (FL).

ROSANO, G. L. & CECCARELLI, E. A. (2014). Recombinant protein expression in Escherichia coli: advances and challenges. *Front Microbiol,* 5**,** 172.

SANTAJIT, S. & INDRAWATTANA, N. (2016). M*ec*hanisms of Antimicrobial Resistance in ESKAPE Pathogens. *Biomed Res Int,* 2016**,** 2475067.

SARIDAKIS, V., CHRISTENDAT, D., KIMBER, M.S., DHARAMSI, A., EDWARDS, A.M., PAI, E.F., (2001). Insights into ligand binding and catalysis of a central step in NAD+ synthesis: structures of Methanobacterium thermoautotrophicum NMN adenylyltransferase complexes. *J. Biol. Chem*. 276, 7225–7232.

SCHAUMBURG, F., ALABI, A.S., PETERS, G., BECKER, K., (2014). New epidemiology of Staphylococcus aureus infection in Africa. *Clinical Microbiology and Infection* 20, 589–596.

SCHERBAUM, M., KÖSTERS, K., MÜRBETH, R. E., NGOA, U. A., KREMSNER, P. G., LELL, B. & ALABI, A. (2014). Incidence, pathogens and resistance patterns of nosocomial infections at a rural hospital in Gabon. *BMC infectious diseases,* 14**,** 124-124.

SERSHON, V.C., SANTARSIERO, B.D., MES*EC*AR, A.D., (2009). Kinetic and X-Ray Structural Evidence for Negative Cooperativity in Substrate Binding to Nicotinate Mononucleotide Adenylyltransferase (NMAT) from Bacillus anthracis. *Journal of Molecular Biology* 385, 867–888.

SILVERSTEIN, T.P., (2016). The Alcohol Dehydrogenase Kinetics Laboratory: Enhanced Data Analysis and Student-Designed Mini-Projects. *Journal of Chemical Education* 93, 963–970.

SINGH, K., HUSSAIN, I., MISHRA, V., AKHTAR, MD.S., (2019). New insight on 8-anilino-1-naphthalene sulfonic acid interaction with TgFNR for hydrophobic exposure analysis. *International Journal of Biological Macromolecules* 122, 636–643.

SORCI, L., PAN, Y., EYOBO, Y., RODIONOVA, I., HUANG, N., KURNASOV, O., ZHONG, S., MACKERELL, A. D., JR, ZHANG, H., & OSTERMAN, A. L. (2009). Targeting NAD biosynthesis in bacterial pathogens: Structure-based development of inhibitors of nicotinate mononucleotide adenylyltransferase NadD. *Chemistry & biology*, 16(8), 849–861.

SPAANS, S. K., WEUSTHUIS, R. A., VAN DER OOST, J. & KENGEN, S. W. M. (2015). NADPH-generating systems in bacteria and archaea. *Frontiers in microbiology,* 6**,** 742-742.

STANCEK, M., SCHNELL, R., RYDÉN-AULIN, M., (2005). Analysis of Escherichia coli nicotinate mononucleotide adenylyltransferase mutants in vivo and in vitro. *BMC Biochemistry* 6, 16.

SUN, J., DENG, Z., YAN, A. (2014). Bacterial multidrug efflux pumps: Mechanisms, physiology and pharmacological exploitations. *Biochemical and Biophysical Research Communications, Integrative Glycobiology and Future Perspectives* 453, 254–267.

SZULC, A., APPELHANS, D., VOIT, B., BRYSZEWSKA, M., KLAJNERT, B., (2013). Studying Complexes Between PPI Dendrimers and Mant-ATP. *J Fluoresc* 23, 349–356.

TACCONELLI, E., CARRARA, E., SAVOLDI, A., HARBARTH, S., MENDELSON, M., MONNET, D.L., PULCINI, C., KAHLMETER, G., KLUYTMANS, J., CARMELI, Y., OUELLETTE, M., OUTTERSON, K., PATEL, J., CAVALERI, M., COX, E.M., HOUCHENS, C.R., GRAYSON, M.L., HANSEN, P., SINGH, N., THEURETZBACHER, U., MAGRINI, N., WHO Pathogens Priority List Working Group, (2018). Discovery, research, and development of new antibiotics: the WHO priority list of antibiotic-resistant bacteria and tuberculosis. *Lancet Infect Dis* 18, 318–327.

TAYLOR, T.A., UNAKAL, C.G., (2020). Staphylococcus Aureus, in: StatPearls. StatPearls Publishing, Treasure Island (FL).

TSHABALALA, T.N., TOMESCU, M.-S., PRIOR, A., BALAKRISHNAN, V., SAYED, Y., DIRR, H.W., ACHILONU, I., (2016). Energetics of Glutathione Binding to Human Eukaryotic Elongation Factor 1 Gamma: Isothermal Titration Calorimetry and Molecular Dynamics Studies. *Protein J*. 35, 448–458.

TURNBULL, (2005). Divided We Fall ? Studying low affinity fragments of ligands by ITC Ultrasensitive Calorimetry.

TZOUVELEKIS, L. S., MARKOGIANNAKIS, A., PSICHOGIOU, M., TASSIOS, P. T. & DAIKOS, G. L. (2012). Carbapenemases in Klebsiella pneumoniae and other Enterobacteriaceae: an evolving crisis of global dimensions. *Clin Microbiol Rev,* 25**,** 682-707.

UHR, M., (2010). Coupled enzyme systems: Exploring coupled assays with students. *Biochemical Education* 18, 48–50.

VON WINTERSDORFF, C. J. H., PENDERS, J., VAN NIEKERK, J. M., MILLS, N. D., MAJUMDER, S., VAN ALPHEN, L. B., SAVELKOUL, P. H. M. & WOLFFS, P. F. G. (2016). Dissemination of Antimicrobial Resistance in Microbial *Ec*osystems through Horizontal Gene Transfer. *Frontiers in microbiology,* 7**,** 173-173.

WAGNER, MICHAEL., (1976). Enzyme kinetics, behavior and analysis of rapid equilibrium and steady-state enzyme systems (Segel, Irwin H.). *J. Chem. Educ*. 53, A472.

WANG, X., ZHOU, Y. J., WANG, L., LIU, W., LIU, Y., PENG, C. & ZHAO, Z. K. 2017. Engineering Escherichia coli Nicotinic Acid Mononucleotide Adenylyltransferase for Fully Active Amidated NAD Biosynthesis. *Appl Environ Microbiol,* 83.

WANG, Y., TERAOKA, I., HANSEN, F. Y., PETERS, G. H. & HASSAGER, O. (2010). A Theoretical Study of the Separation Principle in Size Exclusion Chromatography. *Macromolecules,* 43**,** 1651-1659.

WATERHOUSE, A., BERTONI, M., BIENERT, S., STUDER, G., TAURIELLO, G., GUMIENNY, R., HEER, F.T., DE BEER, T.A.P., REMPFER, C., BORDOLI, L., LEPORE, R., SCHWEDE, T. (2018) SWISS-MODEL: homology modelling of protein structures and complexes. *Nucleic Acids Res*. 46(W1), W296-W303

WAUGH, D. S. (2011). An overview of enzymatic reagents for the removal of affinity tags. *Protein Expr Purif,* 80**,** 283-93.

WEI, Y., THYPARAMBIL, A., LATOUR, R., (2014). Protein Helical Structure Determination Using CD Spectroscopy for Solutions with Strong Background Absorbance from 190-230 nm. *Biochimica et biophysica acta* 1844.

WHITMORE, L., WALLACE, B.A., (2004). DICHROWEB, an online server for protein secondary structure analyses from circular dichroism spectroscopic data. *Nucleic Acids Res* 32, W668–W673.

WINIEWSKA, M., BUGAJSKA, E., POZNAŃSKI, J., (2017). ITC-derived binding affinity may be biased due to titrant (nano)-aggregation. Binding of halogenated benzotriazoles to the catalytic domain of human protein kinase CK2. *PLoS ONE* 12, e0173260.

WITTINGHOFER, A., (2016). GTP and ATP hydrolysis in biology. *Biopolymers* 105, 419–421.

WYRES, K. L. & HOLT, K. E. (2018). Klebsiella pneumoniae as a key trafficker of drug resistance genes from environmental to clinically important bacteria. *Curr Opin Microbiol,* 45**,** 131-139.

XIAO, W., WANG, R. S., HANDY, D. E. & LOSCALZO, J. (2018). NAD(H) and NADP(H) Redox Couples and Cellular Energy Metabolism. *Antioxid Redox Signal,* 28**,** 251-272.

YOON, H.-J., KIM, H.L., MIKAMI, B., SUH, S.W., (2005). Crystal Structure of Nicotinic Acid Mononucleotide Adenylyltransferase from Pseudomonas aeruginosa in its Apo and Substrate-complexed Forms Reveals a Fully Open Conformation. *Journal of Molecular Biology* 351, 258–265.

YOUNG C. L., BRITTON Z. T., ROBINSON A. S. (2012). Recombinant protein expression and purification: a comprehensive review of affinity tags and microbial applications. *Biotechnol. J*. 7 620–634

ZHAI, R.G., RIZZI, M., GARAVAGLIA, S., (2009). Nicotinamide/nicotinic acid mononucleotide adenylyltransferase, new insights into an ancient enzyme. *Cell. Mol. Life Sci.* 66, 2805–2818.

ZHANG, H., ZHOU, T., KURNASOV, O., CHEEK, S., GRISHIN, N. V., OSTERMAN, A. (2002). Crystal structures of E. coli nicotinate mononucleotide adenylyltransferase and its complex with deamido-NAD. *Structure,* 10**,** 69-79.

ZHANG, X., KURNASOV, O.V., KARTHIKEYAN, S., GRISHIN, N.V., OSTERMAN, A.L., ZHANG, H., (2003). Structural Characterization of a Human Cytosolic NMN/NaMN Adenylyltransferase and Implication in Human NAD Biosynthesis. *J. Biol. Chem*. 278, 13503–13511.

ZHAO, X., LI, G., LIANG, S., (2013). Several Affinity Tags Commonly Used in Chromatographic Purification. *Journal of Analytical Methods in Chemistry*.

ZHOU, T., KURNASOV, O., TOMCHICK, D.R., BINNS, D.D., GRISHIN, N.V., MARQUEZ, V.E., OSTERMAN, A.L., ZHANG, H., (2002). Structure of Human Nicotinamide/Nicotinic Acid Mononucleotide Adenylyltransferase BASIS FOR THE DUAL SUBSTRATE SPECIFICITY AND ACTIVATION OF THE ONCOLYTIC AGENT TIAZOFURIN. *J. Biol. Chem*. 277, 13148–13154.

SUPPLEMENTARY INFORMATION

Calculation for wet biomass concentration:

Volume of pooled protein: ~20 mL

Concentration of pooled protein: ~6 mg/mL

Total pellet weight per 4 L of expression: 21.6 g

$$\text{Concentration} = 120 \text{ mg}$$

$$\text{Wet biomass concentration} = 120\,\text{mg}/21.6\,\text{g}$$

$$= \mathbf{5.5\ mg/g\ of}\ \boldsymbol{E.coli}\ \mathbf{cells}$$

A

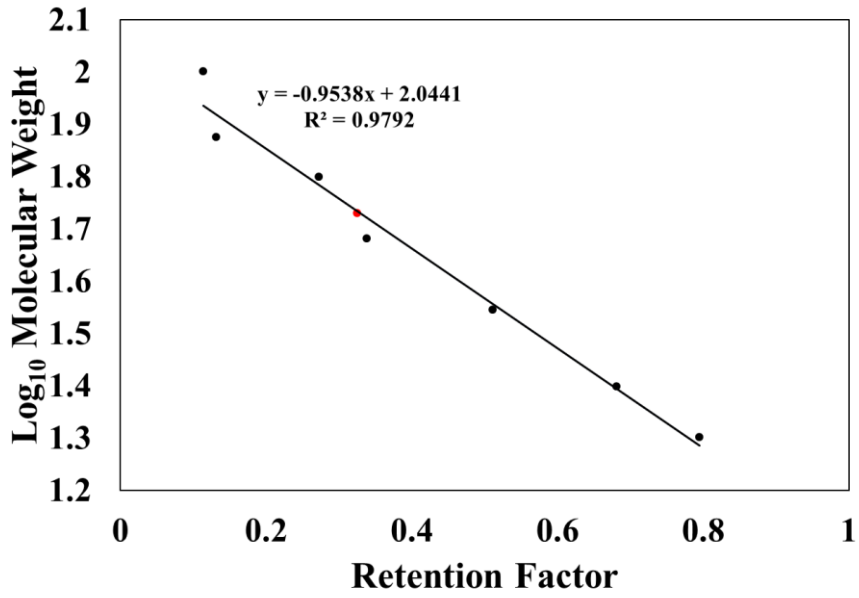
y = -0.9538x + 2.0441
R² = 0.9792
Log10 Molecular Weight
Retention Factor
2.1
2
1.9
1.8
1.7
1.6
1.5
1.4
1.3
1.2
0
0.2
0.4
0.6
0.8
1

B

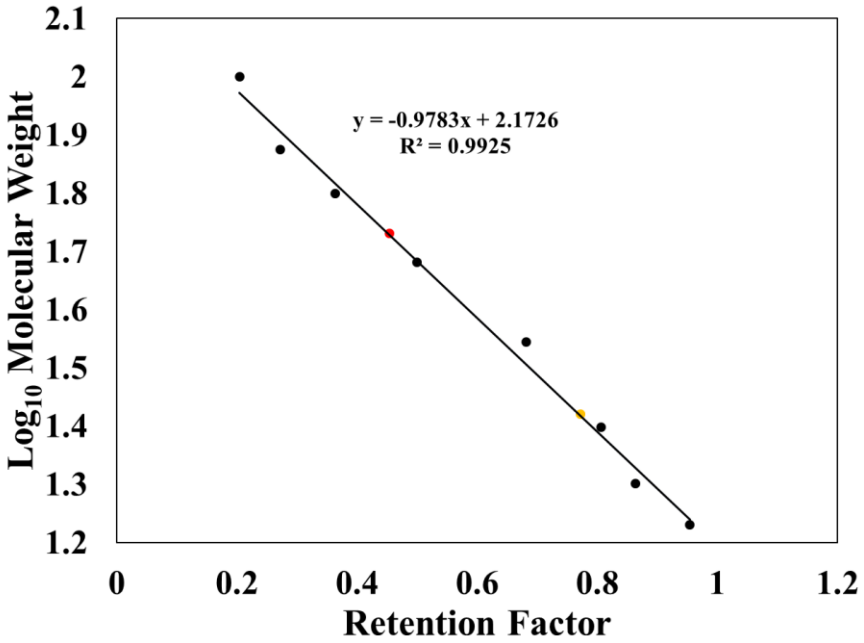
y = -0.9783x + 2.1726
R² = 0.9925
Log10 Molecular Weight
Retention Factor
2.1
2
1.9
1.8
1.7
1.6
1.5
1.4
1.3
1.2
0
0.2
0.4
0.6
0.8
1
1.2

C

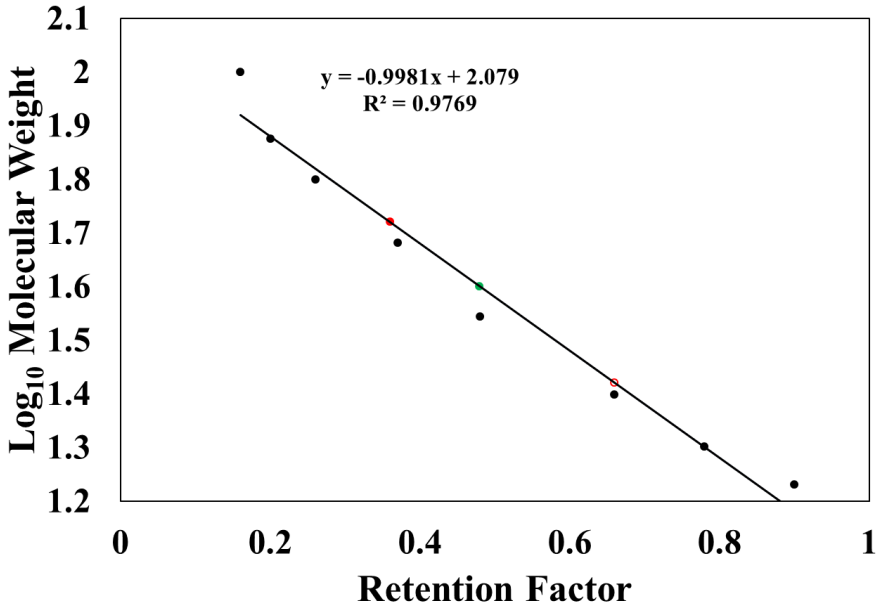
y = -0.9981x + 2.079
R² = 0.9769
Log10 Molecular Weight
Retention Factor
2.1
2
1.9
1.8
1.7
1.6
1.5
1.4
1.3
1.2
0
0.2
0.4
0.6
0.8
1

D

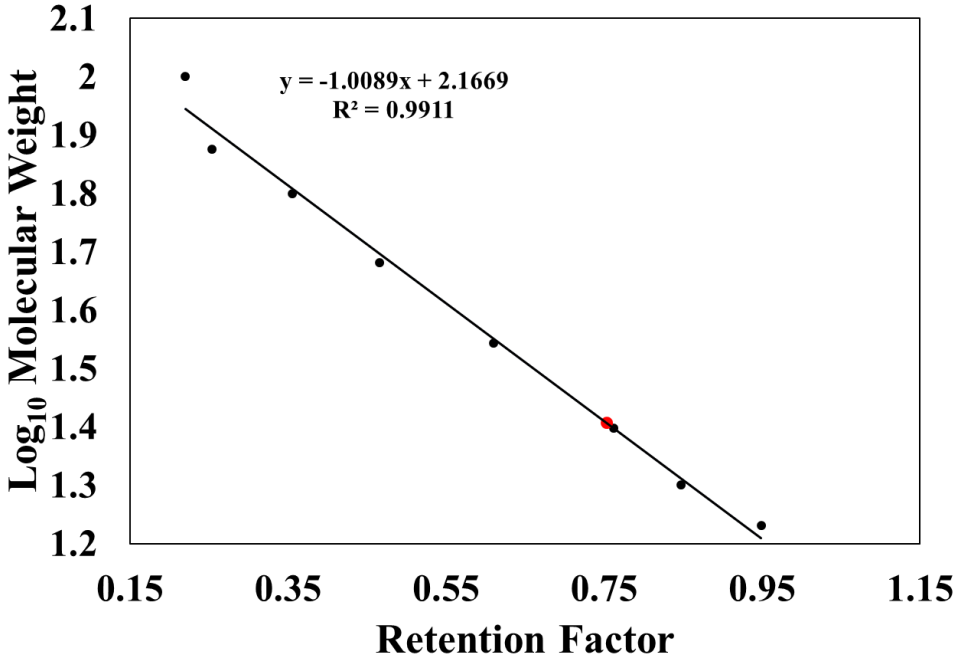
y = -1.0089x + 2.1669
R² = 0.9911
Log10 Molecular Weight
Retention Factor
2.1
2
1.9
1.8
1.7
1.6
1.5
1.4
1.3
1.2
0.15
0.35
0.55
0.75
0.95
1.15

E

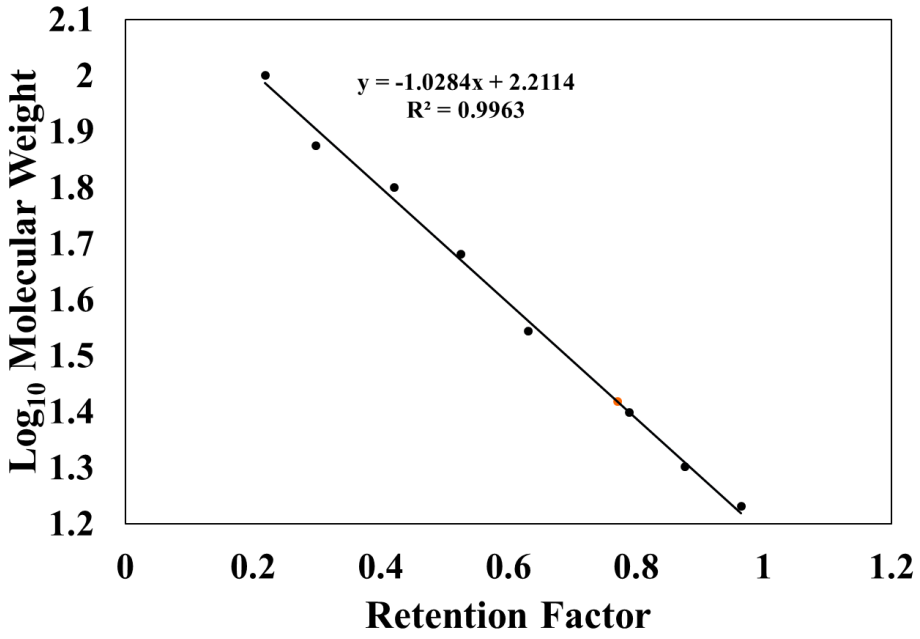

Supplementary figure 1: Standard curve for molecular weight determination of SDS-PAGE gels

Figure A represents the expression trials gel (Figure 4.1), where the red dot indicates uncleaved *Kp*NNAT with a log molecular weight of 1.73. Figure B represents GSH-Agarose elution (Figure 4.2A) which shows uncleaved *Kp*NNAT (red dot) and an impurity (yellow dot) with log molecular weights of 1.73 and 1.42 respectively. Figure C represents thrombin cleavage trials (Figure 4.2B) showing the uncleaved *Kp*NNAT (red dot), thrombin (green dot) and cleaved *Kp*NNAT and cleaved GST tag (open red circle) with log molecular weights of 1.71, 1.59 and 1.42 respectively. Figure D shows the determination of the band size (log_{10} molecular weight of 1.40) in Figure 4.2C which corresponds to ~25 kDa (red dot). Figure E represents GSH-Agarose elution after on-column cleavage (Figure 4.2E) showing cleaved GST tag (orange dot) with a log molecular weight of 1.41.

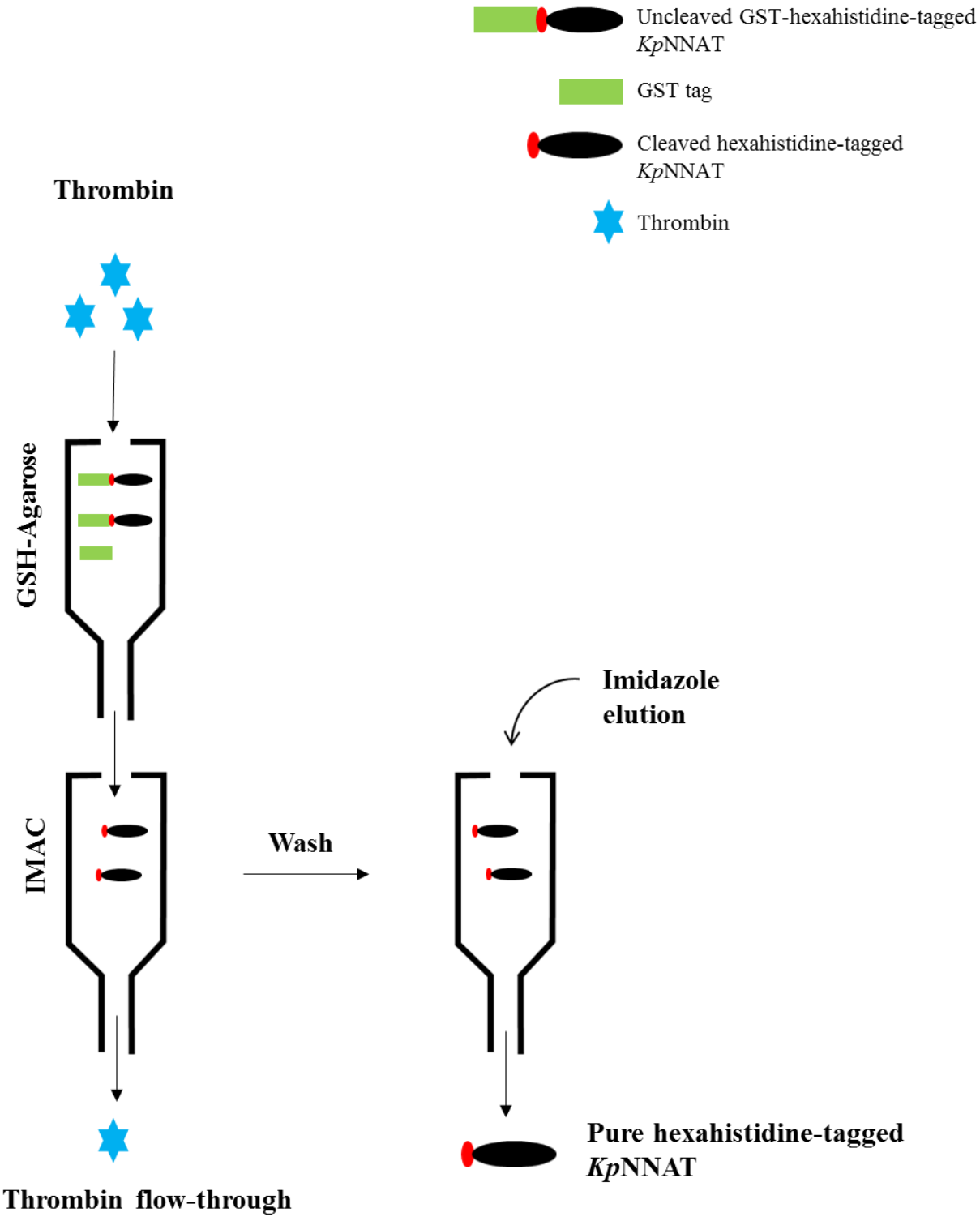

Supplementary figure 2: Double-purification, on-column cleavage strategy for *Kp*NNAT purification.
The purification strategy performed on *Kp*NNAT to derive pure, cleaved hexahistidine-tagged *Kp*NNAT. Initially, the GST-hexahistidine tagged *Kp*NNAT is exposed to a GSH-Agarose column in the presence of thrombin (on-column cleavage). The cleaved hexahistidine-tagged *Kp*NNAT is then continuously passed through an IMAC column, re-purifying *Kp*NNAT by removing thrombin. Lastly, pure hexahistidine-tagged *Kp*NNAT is eluted from the IMAC column using an imidazole wash.

Percentage protein purity derived using ImageJ Software:

From Figure 4.2 C, the percentage purity of IMAC Elution 3 was determined using ImageJ software based on the areas of relative peaks. The table below shows the areas of the peaks from IMAC Elution 3.

Supplementary table 1: Areas of relative peaks from IMAC elution 3 derived from ImageJ

PEAK	AREA
1	860.55
2	188.39
3 (peak of interest)	22057.84

Calculation for percentage purity:

$$\text{Sum of all peaks} = 23106.78$$

$$\text{Percentage purity of peak 3} = (22057.84/23106.78) \times 100$$

$$= \mathbf{95.5}\%$$

Calculation for *Kp*NNAT concentration (Figure 4.4)

$$\text{Protein concentration} = \frac{\text{Slope} \times \text{Molecular weight (daltons)}}{\varepsilon \times \text{Path length}}$$

$$= \frac{21.162 \times 24900}{38055}$$

$$= \mathbf{13.85\ mg\ /\ mL}$$

A

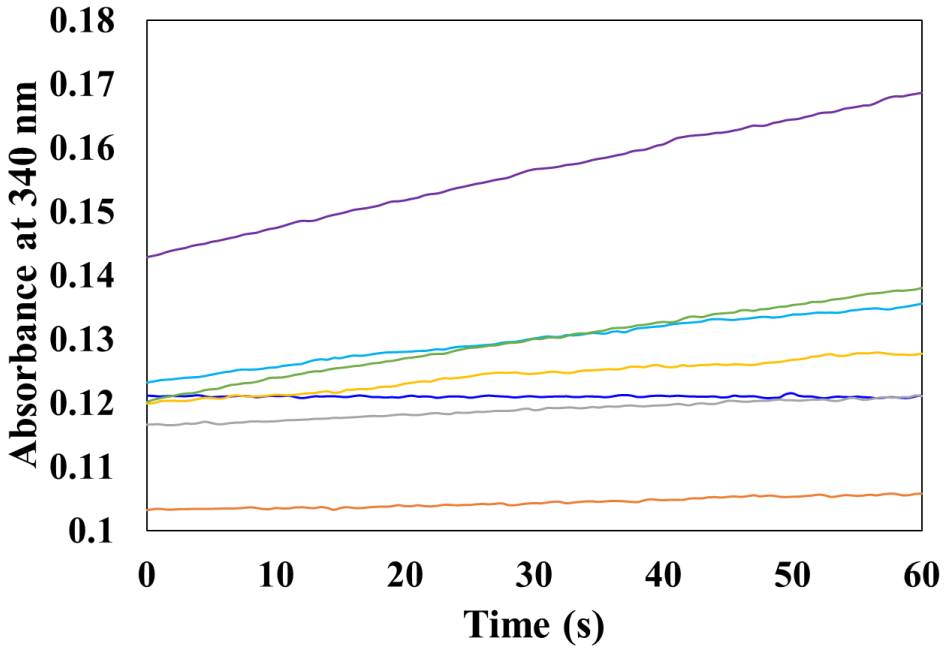

B

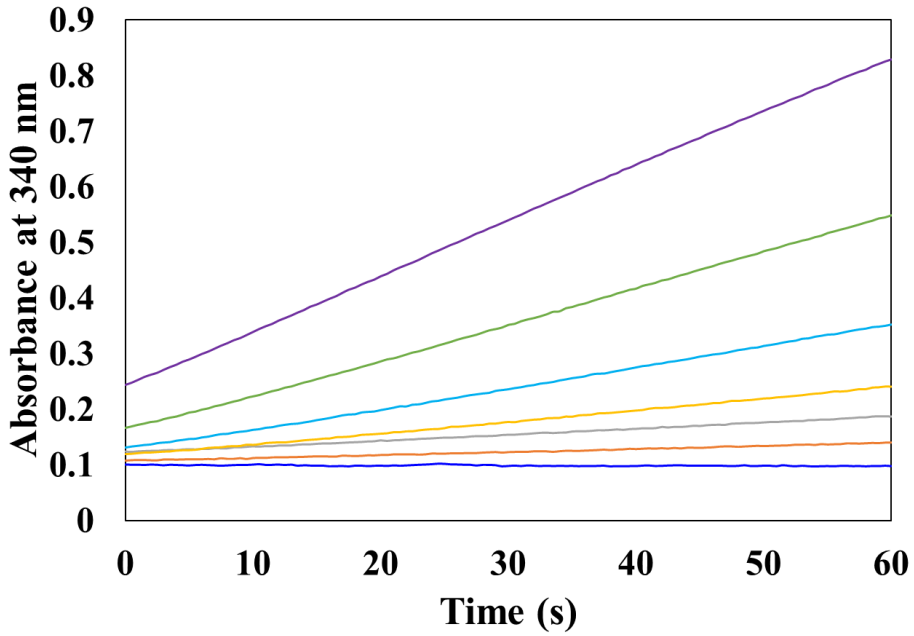

Supplementary figure 3: Progress curves for the varied *Kp*NNAT concentrations for assay

Figure A represents the assay in PBS buffer (pH 7.5) and Figure B represents the assay in Tris-HCl buffer (pH 9.0). The concentrations of *Kp*NNAT used were 0 nM (dark blue), 50 nM (orange), 100 nM (grey), 200 nM (yellow), 400 nM (light blue), 800 nM (green) and 1600 nM (purple).

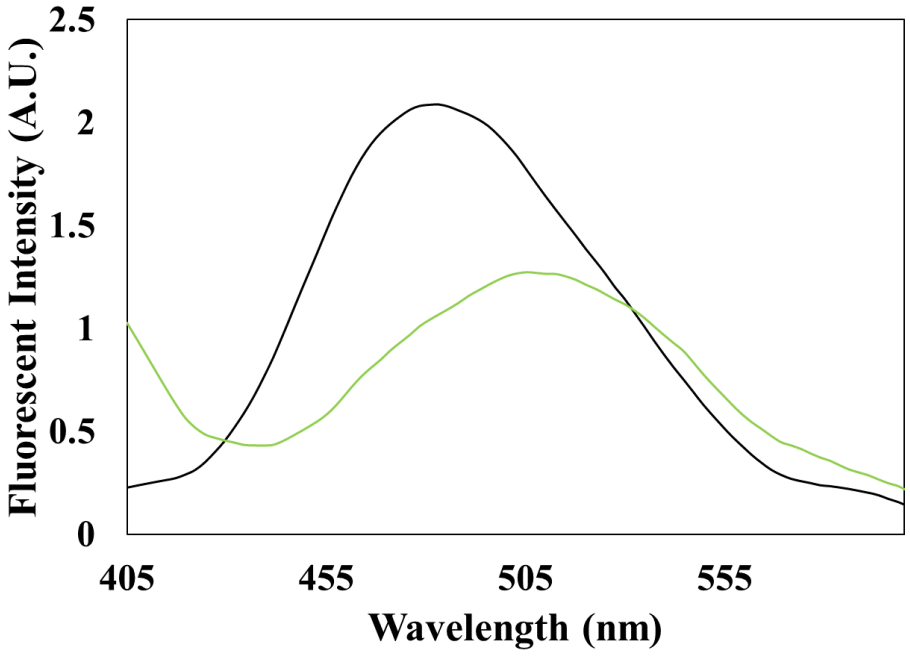

Supplementary figure 4: **ANS fluorescence of denatured *Kp*NNAT in the absence of ligands**

The green spectrum indicates the denatured (8 M urea) *Kp*NNAT in the presence of ANS. The black spectrum indicates native *Kp*NNAT in the presence of ANS. Due to the unfolding of *Kp*NNAT, the denatured sample shows low ANS fluorescent intensity. A blue shift is observed deduced by the decrease in fluorescent intensity and shift to longer wavelength (505 nm from 500 nm).

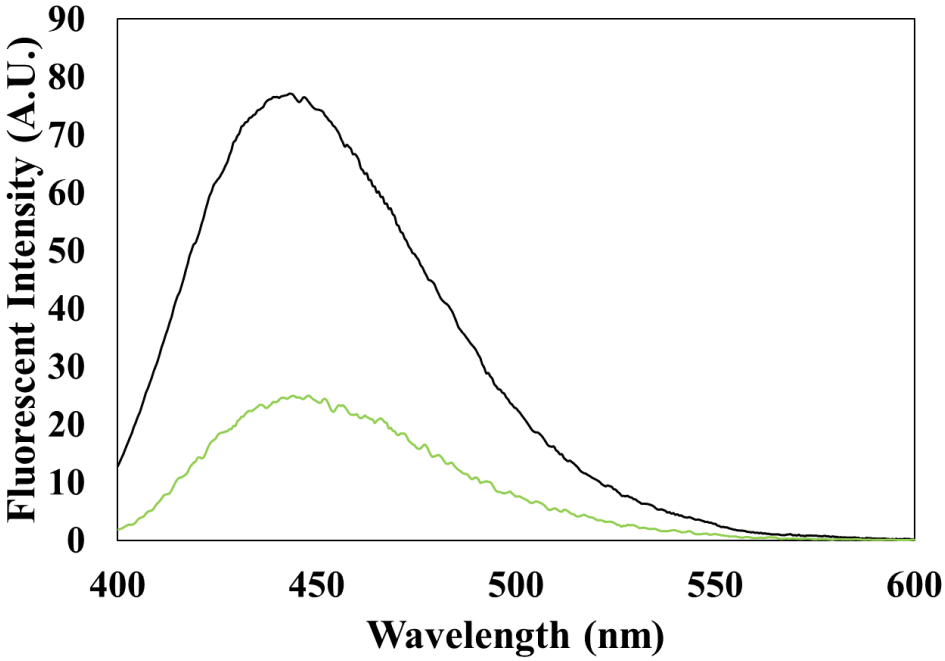

Supplementary figure 5: Mant-ATP fluorescence of denatured *Kp*NNAT in the absence of ligands

The green spectrum indicates the denatured (8 M urea) *Kp*NNAT in the presence of mant-ATP. The black spectrum indicates native *Kp*NNAT in the presence of mant-ATP. Due to the unfolding of *Kp*NNAT, the denatured sample shows low mant-ATP fluorescent intensity.

GGATCCATGGGCCACCACCACCACCACCACGTTGACATGACCCAACTGCAAGCGATTTACGGCGGCACCTTTGACCCGGTTCACTACGGCCACCT
GAAGCCGGTGGAGATCCTGGCGAACCAGATTGGTCTGAGCAAAGTGATCATTATGCCGAACAACGTTCCGCCGCACCGTCCGCAGCCGGAAGCGACCAGC
GCGCAACGTGTTCACATGCTGAAGCTGGCGATCGCGGACAAACCGCTGTTCACCCTGGATGAGCGTGAACTGCGTCGTGATACCCCGAGCTGGACCGCGC
AGACCCTGCAAGAGTGGCGTCAGGAACAAGGTCCGCGTAAGCCGCTGGCGTTCATCATTGGCCAGGATAGCCTGCTGACCTTTCCGACCTGGCACAACTA
CGAAACCATCCTGGACAACGTGCACCTGATTGTTTGCCGTCGTCCGGGCTATCCGCTGACCATGGCGCAGGAAGCGGACCAACGTTGGCTGGATCGTCAC
CTGACCCACGATGTGGAGAGCCTGCACAACAGCCCGAGCGGTGTTATCTACCTGGCGGAAACCCCGTGGTTTGACATTAGCGCGACCATCATTCGTCAAC
GTCTGGAGCGTGGCGAAAGCTGCGCGGAGATGCTGCCGGCGGCGGTGCTGGACTACATTCGTGAACAAGGTCTGTATTGCTAAGCGGCCGC

Supplementary figure 6: Target sequence for *Kp*NNAT

The sequence of *Kp*NNAT expression is shown in the figure. The sequence does not contain the GST tag or the hexahistidine tag. The sequence is used to express the 24.9 kDa enzyme.